

DIELECTRIC FREQUENCY RESPONSE ANALYSIS
APPLIED TO STATOR WINDING INSULATION
SYSTEMS

by

Mathieu LACHANCE-SAVARD

THESIS PRESENTED TO ÉCOLE DE TECHNOLOGIE SUPÉRIEURE
IN PARTIAL FULFILLMENT FOR A MASTER'S DEGREE
WITH THESIS IN ELECTRICAL ENGINEERING
M.A.Sc.

MONTREAL, APRIL 4, 2024

ÉCOLE DE TECHNOLOGIE SUPÉRIEURE
UNIVERSITÉ DU QUÉBEC

© Copyright 2024 reserved by Mathieu Lachance-Savard

© Copyright reserved

It is forbidden to reproduce, save or share the content of this document either in whole or in parts. The reader who wishes to print or save this document on any media must first get the permission of the author.

BOARD OF EXAMINERS

THIS THESIS HAS BEEN EVALUATED

BY THE FOLLOWING BOARD OF EXAMINERS

Mr. Éric David, Thesis Supervisor
Department of Mechanical Engineering, École de technologie supérieure

Mr. Handy Fortin-Blanchette, Chair, Board of Examiners
Department of Electrical Engineering, École de technologie supérieure

Mrs. Mélanie Lévesque, Researcher
Research Institute of Hydro-Quebec (IREQ)

THIS THESIS WAS PRESENTED AND DEFENDED

IN THE PRESENCE OF A BOARD OF EXAMINERS AND THE PUBLIC

ON MARCH 25, 2024

AT ÉCOLE DE TECHNOLOGIE SUPÉRIEURE

Analyse de la réponse diélectrique appliquée pour les systèmes d'isolations des enroulements statoriques

Mathieu LACHANCE-SAVARD

RÉSUMÉ

Cette étude présente les résultats d'investigations effectués dans le but de vérifier si l'application de mesures de spectroscopie diélectrique à basse tension peut détecter la dégradation de l'isolation électrique des enroulements statoriques.

Pour la recherche principale, trois bobines nouvellement fabriquées et ayant une tension d'opération de 13.8 kV ont été soumises à une procédure de vieillissement thermique et de vieillissement sous-tension. Les procédures du vieillissement thermique ont été effectuées selon IEEE 1310 alors qu'une version modifiée de IEEE 1553 a été utilisée pour le vieillissement sous-tension. Les trois bobines ont été vieilles jusqu'à la défaillance de leur diélectrique. Plusieurs essais diélectriques ont été effectués à différents moments au cours du vieillissement. Les résultats de mesure de la spectroscopie diélectrique ont été comparés aux résultats de mesures de décharges partielles et de facteur de dissipation traditionnel pour évaluer la sensibilité de la spectroscopie diélectrique à détecter le vieillissement de l'isolation.

L'étude discute également d'importants facteurs affectant les résultats des essais tels que l'effet des parties non-linéaire anti-effluves. Les résultats d'expérimentations et d'essais additionnels sont utilisés afin de démontrer comment les matériaux des parties anti-effluves se comportent, en fonction du niveau et de la fréquence de la tension appliquée. Les conclusions de l'analyse des résultats effectués pour des bobines sont également appliquées à la théorie des essais sur des enroulements statoriques complets.

Mots-clés: spectroscopie fréquentielle, machines tournantes, isolation statorique

Dielectric frequency response analysis applied to stator winding insulation systems

Mathieu LACHANCE-SAVARD

ABSTRACT

This study presents the results of investigations that were performed to verify if the use of low-voltage dielectric frequency response analysis can be successfully applied to detect the deterioration of stator winding insulation systems.

For the main investigation, three newly manufactured stator coils with a rated voltage of 13.8 kV were aged using the thermal cycle testing procedures described in IEEE 1310 and an extended and modified version of voltage endurance testing described in IEEE 1553, until dielectric failure. Throughout the accelerated ageing process, several dielectric measurements were performed, and the results trended over time. The results of the dielectric frequency response measurements were then compared with conventional dissipation factor measurements and partial discharge measurements to assess the sensitivity of dielectric frequency response analysis applied to stator insulation.

This study also discusses the effects of the nonlinear end-potential grading material on the measured dielectric losses. Additional experiments are summarized to illustrate how this nonlinear material behaves depending on the applied voltage level and frequency. The conclusions of the investigation are also extended, and the principles applied to measurements on complete stator windings, installed in the field.

Keywords: frequency domain spectroscopy, rotating machines, stator windings

TABLE OF CONTENTS

	Page
INTRODUCTION	1
CHAPTER 1 Review of electrical insulation systems of stator windings in high-voltage electrical rotating machines.....	3
1.1 Introduction to rotating machines	3
1.2 Construction of stator windings	6
1.2.1 Strand insulation	10
1.2.2 Turn insulation	11
1.2.3 Main or groundwall insulation.....	11
1.2.4 Outer corona protection (OCP).....	12
1.2.5 End potential grading (EPG).....	13
1.2.6 Other components	15
CHAPTER 2 Degradation mechanisms and current electrical diagnostic methods for stator windings	17
2.1 Degradation mechanisms in stator windings	17
2.1.1 Thermal stress	18
2.1.2 Electrical stress	19
2.1.3 Ambient stress.....	19
2.1.4 Mechanical stress	20
2.2 Current electrical diagnostic methods for stator windings	20
2.2.1 Insulation resistance.....	21
2.2.2 Polarization index	21
2.2.3 Polarization and depolarization current analysis	21
2.2.4 Direct-voltage ramp test.....	22
2.2.5 Dissipation factor measurement.....	22
2.2.6 Partial discharge measurements.....	23
CHAPTER 3 Electric properties of dielectric materials	25
3.1 Conduction in dielectric materials	25
3.2 Electric polarization in static electric field	26
3.2.1 Introduction to electric polarization.....	26
3.2.2 Electric permittivity	28
3.2.3 Electric polarization mechanisms	31
3.3 Electric polarization in time domain.....	33
3.4 Electric polarization in variable field.....	37
3.5 Application for stator winding insulation systems.....	40
CHAPTER 4 Artificial ageing of test objects	43
4.1 Stator coil specimens	43
4.2 Thermal cycling test.....	44

4.3	Voltage endurance test at elevated temperature.....	46
4.4	Voltage endurance test at room temperature	48
CHAPTER 5 Description of the test procedures.....		51
5.1	Dielectric frequency response (DFR) measurements	52
5.2	Partial discharge (PD) measurements	54
5.3	Conventional dissipation factor (DF) measurements.....	58
CHAPTER 6 Influence of end potential grading on dielectric loss measurements		61
6.1	Frequency dependency.....	62
6.2	Voltage dependency.....	66
6.3	Modeling of EPG	71
CHAPTER 7 Results of measurements.....		79
7.1	Coil 07.....	79
7.1.1	Results of DFR measurements.....	79
7.1.2	Results of PD measurements	87
7.1.3	Results of DF measurements	90
7.1.4	Analysis of the fault.....	92
7.2	Coil 19.....	92
7.2.1	Results of DFR measurements.....	93
7.2.2	Results of PD measurements	97
7.2.3	Analysis of the fault.....	100
7.3	Coil 20.....	102
7.3.1	Results of DFR measurements.....	102
7.3.2	Results of PD measurements	106
7.3.3	Analysis of the fault.....	109
CHAPTER 8 Application for complete stator windings.....		115
8.1	The value of the initial measurement.....	115
8.2	Influence of stator winding capacitance	116
8.3	Assessment of the loss peak.....	119
CONCLUSION		121
BIBLIOGRAPHY.....		123

LIST OF TABLES

		Page
Table 3.1	Relative permittivity of different materials.....	31
Table 3.2	Schematics of different polarization mechanism Adapted from David (2010, p.6).....	32
Table 5.1	Summary of the performed dielectric measurements	52
Table 7.1	Summary of the measured DF values for coil 07 from figure 7.1 and figure 7.2.....	81
Table 7.2	Measured PRPD patterns at different stages of the ageing process of coil 07.....	88
Table 7.2	Measured PRPD patterns at different stages of the ageing process of coil 07 (cont'd).....	89
Table 7.3	Summary of the measured DF values for coil 19 from figure 7.10 and figure 7.11	94
Table 7.6	Measured PRPD patterns at different stages of the ageing process of coil 20.....	108
Table 8.1	Results of typical DF measurements performed with guards at the factory with measurements performed at lower voltage, without guards	116

LIST OF FIGURES

	Page
Figure 1.1	Image showing the three different main components of an electrical machine Adapted from OMICRON (2023, p. 5)4
Figure 1.2	Image of a magnetic core Taken from OMICRON (2021, p. 2).....4
Figure 1.3	Picture of a magnetic core being assembled Taken from OMICRON (2021, p. 2).....5
Figure 1.4	Picture of a stator winding of a 230 MW turbo generator Taken from Lachance & Oetl (2020, p. 435)6
Figure 1.5	Picture of stator coils Taken from OMICRON (2023, p. 30).....7
Figure 1.6	Picture of stator bars Taken from OMICRON (2023, p. 30).....7
Figure 1.7	Simplified sketch of a three-phase electrical machine with two circuits per phase8
Figure 1.8	Picture of a stator winding diagram of a hydro-generator8
Figure 1.9	Picture of a stator winding making the distinction between the slot portion and the endwinding area.....9
Figure 1.10	Cross-sectional cuts of a stator bar and a stator coil Adapted from OMICRON (2023, p. 34)10
Figure 1.11	Picture of a taping Taken from OMICRON (2023, p. 37).....12
Figure 1.12	Image showing the use of OCP material Taken from OMICRON (2023, p. 43).....13
Figure 1.13	Picture of a stator coil showing the OCP and the EPG area Taken from OMICRON (2023, p. 42)14
Figure 1.14	Energized insulated conductor passing through a grounded metallic screen. (left) Typical configuration. (right) Equipotential lines and stress distribution Taken from Can-Otiz et al. (2021, p. 2)14
Figure 1.15	Picture of an experiment showing the discharges occurring when no EPG is used Taken from OMICRON (2023, p. 45).....15
Figure 2.1	Attributed causes of failure from 69 hydro generators Taken from OMICRON (2023, p. 4)18

Figure 3.1 Electric dipole Adapted from Fournie & Coelho (2000, p. 3)26

Figure 3.2 Electric polarization from a dielectric material28

Figure 3.3 Charge accumulation on the surface of the electrodes (left: surface charge accumulation in vacuum and right: charge density created in a dielectric material)29

Figure 3.4 Polarization under direct voltage Adapted from Ravindra & Wolfgang (2022, p. 353).....34

Figure 3.5 Example of a measured polarization (solid) and depolarization (dash) current on a hydro generator37

Figure 3.6 Phasor diagram representing the applied voltage U and the measured current with corresponding loss angles38

Figure 3.7 Sketch showing the frequency dependence of different polarization mechanism Taken from OMICRON (2019, p. 7)40

Figure 4.1 Schematic showing the cross-sectional dimensions of a stator coil44

Figure 4.2 Picture of the three stator coils used as test specimens.....44

Figure 4.3 Connection diagram of the coils for the thermal cycling test46

Figure 4.4 Picture of the test bench for the thermal cycling test.....46

Figure 4.5 Connection diagram of the coils for the voltage endurance test.....47

Figure 4.6 Picture of the test bench for the voltage endurance test.....48

Figure 4.7 Picture of the coil three hours after the beginning of the stage 3 ageing process49

Figure 4.8 Picture of the test bench for the voltage endurance test at room temperature49

Figure 5.1 Comparison of the obtained DFR curves for the measurements using PDC and FDS, for two different test objects53

Figure 5.2 Image of the test setup used for DFR measurement54

Figure 5.3 Schematic of the test setup used for PD measurements.....55

Figure 5.4 Picture of the test setup during PD measurements.....56

Figure 5.5 Applied voltage test sequence used for the PD measurements.....56

Figure 5.6	Simplified schematic describing how the PRPD diagram is built Taken from OMICRON (2020, p. 17)	57
Figure 5.7	Examples of PRPD diagrams associated with typical defects on stator windings Taken from OMICRON (2023, p. 355).....	58
Figure 5.8	Schematic of the test setup used for the conventional DF measurements.....	59
Figure 6.1	Typical V-I curves of EPG Taken from Conley & Frost (2005, p. 92).....	62
Figure 6.2	Picture of one of the guard electrodes installed on coil 02	64
Figure 6.3	Guarded and unguarded measured real capacitance of the slot sections and the EPG sections using linear Y-scaling	65
Figure 6.4	Guarded measured imaginary capacitance of the slot sections and the EPG sections using linear Y-scaling.....	65
Figure 6.5	Complex capacitance measured from the PTFE tube Taken from Taylor (2010, p. 186)	67
Figure 6.6	Picture of one of the guard electrodes installed on coil 07	68
Figure 6.7	Guarded measured losses of the slot sections and the EPG sections.....	69
Figure 6.8	Comparison of DF measurements when performed with and without temporarily installed guard electrodes	69
Figure 6.9	Measured apparent charge on coil 07 after 589 hours of VET showing the significant increase in PD activities from 6 kV _{RMS} to 8 kV _{RMS}	70
Figure 6.10	R-C circuit equivalent to Debye equations	71
Figure 6.11	Simulated imaginary capacitance of a simple R-C with empirical parameters and, experimental results from a guarded measurement for coil 02.....	74
Figure 6.12	Simulated real capacitance of a simple R-C with empirical parameters and, experimental results from a guarded measurement for coil 02	75
Figure 6.13	Simulated imaginary capacitance using the HN model compared with the measured imaginary capacitance of coil 07, after 208 hours of VET.....	77

Figure 7.1 Power factor curves measured on coil 07 using a linear scaling for the y-axis.....80

Figure 7.2 Power factor curves measured on coil 07 using a logarithmic scaling for the y-axis80

Figure 7.3 Summarized curves of the imaginary capacitance for coil 0783

Figure 7.4 Summarized curves of the real capacitance for coil 0784

Figure 7.5 Schematic of the test setup for the measurements of the resistivity of the EPG coating85

Figure 7.6 Measured resistance per unit of length of the EPG.....85

Figure 7.7 Trend of the measured apparent charge for coil 0788

Figure 7.8 Measured DF measurements at 60 Hz at different stages of the ageing process.....90

Figure 7.9 Results of guarded DF measurements after 589 hours and 1613 hours of ageing.....91

Figure 7.10 Power factor curves measured on coil 19 using a linear scaling for the y-axis.....93

Figure 7.11 Power factor curves measured on coil 19 using a logarithmic scaling for the y-axis94

Figure 7.12 Measured imaginary capacitance curves on coil 19 displayed using a linear scaling for the y-axis.....95

Figure 7.13 Measured imaginary capacitance curves on coil 19 displayed using a logarithmic scaling for the y-axis96

Figure 7.14 Measured real capacitance curves measured on coil 1996

Figure 7.15 Trend of the measured apparent charge for coil 1998

Figure 7.16 Picture of the suspect fault area of coil 19.....100

Figure 7.17 Picture of the cross-sectional cut in the suspected fault area using a stereoscope.....101

Figure 7.18 Cross-sectional cut of an unaged coil102

Figure 7.19 Power factor curves measured on coil 20 using a logarithmic scaling for the y-axis103

Figure 7.20	Power factor curves measured on coil 20 using a linear scaling for the y-axis.....	103
Figure 7.21	Measured real capacitance curves on coil 20.....	105
Figure 7.22	Measured imaginary capacitance curves on coil 20	105
Figure 7.23	Trend of the measured apparent charge for coil 20	107
Figure 7.24	Sketches summarizing the process for localization of the fault.....	110
Figure 7.25	Picture of the suspected fault area	111
Figure 7.26	Picture of the cross-sectional cut in the suspected fault area using a microscope	111
Figure 7.27	Picture of the upper right corner of figure 7.26	112
Figure 8.1	Projected DFR curves of coil 19 with different capacitance values	117
Figure 8.2	DFR curves from measurements performed on a 172 MVA hydro generator	118
Figure 8.3	DFR curves from measurements performed on a 16 kV turbo generator	119

LIST OF ABBREVIATIONS

AC	Alternative current
CIGRE	International Council on Large Electric Systems
DC	Direct current
DF	Dissipation factor
DFR	Dielectric frequency response
EPG	End potential grading
FDS	Frequency domain spectroscopy
IEC	International Electrotechnical Commission
IEEE	Institute of Electrical and Electronics Engineers
IPG	Inner potential grading
IR	Insulation resistance
OCP	Outer corona protection
PD	Partial discharge
PI	Polarization index
PRPD	Phase resolved partial discharge
PTFE	Polytetrafluoroethylene
PVC	Polyvinyl chloride
RMS	Root mean square
SiC	Silicon carbide
TC	Thermal cycle
VET	Voltage endurance test
VPI	Vacuum pressure impregnated

LIST OF SYMBOLS AND UNITS OF MEASUREMENT

ε	Absolute permittivity
ω	Angular frequency
C	Capacitance
q	Charge
σ_p	Charge density
σ_0	Charge density in vacuum
C^*	Complex capacitance
σ_{dc}	DC conductivity
ρ_{dc}	DC resistivity
χ	Electric susceptibility
C''	Imaginary capacitance
ε_r''	Imaginary relative permittivity
ε_0	Permittivity of vacuum
$\cos \phi$	Power factor
C'	Real capacitance
ε_r'	Real relative permittivity
ε_r	Relative permittivity
$\tan \delta$	Tangent delta
Ω	Volume

XXII

A	Ampere [A]
C	Coulomb [A.s]
F	Farad [$A^2 \cdot s^4 / m^2 / kg$]
h	Hour [h]
Hz	Hertz [1/s]
m	Meter [m]
s	Second [s]
V	Volt [$kg \cdot m^2 / A \cdot s^3$]
VA	Volt ampere [$kg \cdot m^2 / s^3$]
VAR	Volt ampere reactive [$kg \cdot m^2 / s^3$]
W	Watts [$kg \cdot m^2 / s^3$]
Ω	Ohms [$m^2 \cdot kg / s^3 / A^2$]

INTRODUCTION

This project was performed in order to evaluate if the use of dielectric frequency response (DFR) analysis can be used successfully for condition assessment of the electrical insulation of stator windings of high-voltage electrical machines. DFR measurements have been used for more than two decades to quantify the moisture content in the paper of power transformers and have recently been used for the insulation assessment of unshielded low-voltage cables installed in nuclear power plants (Gafvert et al., 2000), (Gorji et al., 2020). It has also been recently investigated for the use on stator windings (C. Hao & B. Gao, 2016), (E. Calo & al., 2020). There are several potential advantages of using DFR measurements instead or, in addition to other conventional dielectric loss measurements. For example, when the measurement is performed on liquid filled transformers, the DFR measurements offer the possibility to quantify different polarization mechanisms independently from each other. For rotating machines, this independent quantification could potentially lead to a narrower and more accurate diagnostic as per, which degradation mechanism is occurring, instead of simply providing the measured losses at power frequency, for example.

The first two chapters of this document provide information about the construction of stator winding insulation system (chapter 1), and about the common deterioration processes and electrical measurement techniques applied to stator windings (chapter 2). Chapter 3 introduces the electric properties of dielectric materials, which is useful at this point onward. These chapters are only meant to provide enough background information to readers who might not be familiar on those topics and will help them to understand the subsequent chapters. Readers that are only interested in the experimental portion of this work and the corresponding results are encouraged to skip those chapters. Chapters 4 and 5 explain the experimental work which was done as part of this research project including the accelerated ageing protocol and the procedures of the dielectric measurements. Because of the strong influence of the end potential grading material on dielectric measurements, chapter 6 offers a review of the literature as well as a summary of some additional experiments that were done to get a better understanding on this topic. The results of the main experiment are summarized in chapter 7 while in chapter 8,

the understanding gained from the experiments on individual components are applied to complete assembly of stator windings.

CHAPTER 1

REVIEW OF ELECTRICAL INSULATION SYSTEMS OF STATOR WINDINGS IN HIGH-VOLTAGE ELECTRICAL ROTATING MACHINES

This section introduces electrical insulation systems used in stator windings of high-voltage electrical machines. It provides enough background information for the reader to understand the subsequent chapters of this document. There are several different types of rotating machines in operation and therefore, a complete description is beyond the scope of this document. The research performed in this project was focused on the stator windings of high-voltage machines (e.g., rated voltage of 2.4 kV_{RMS} and above) and therefore, the provided information pertains to this type of machine. For more information regarding the construction of rotating machines in general, the reader can refer to the following references: (Stone, Culbert, Boulter & Dhirani, 2014), (Boulder & Stone, 2004), (Bomben, Mottershead, & Klempner, 2020) and (Klemper & Kerszenbaum, 2018).

1.1 Introduction to rotating machines

Rotating electrical machines are made up of three different main components: a) the magnetic core, b) the rotor and c) the stator. Figure 1.1 shows an example of a horizontal rotating machine with all three components displayed and with the stator winding highlighted in yellow.

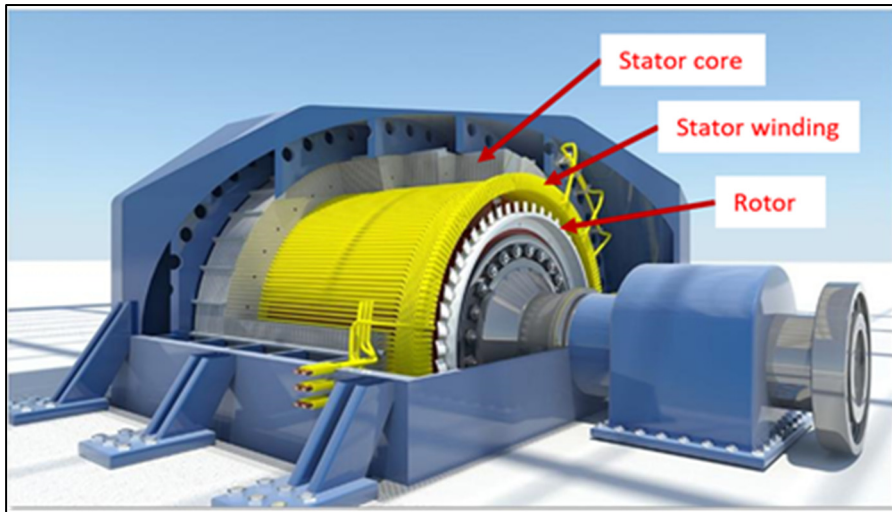


Figure 1.1 Image showing the three different main components of an electrical machine
Adapted from OMICRON (2023, p. 5)

The magnetic core is made of several thin insulated steel laminations that are stacked together to form a close magnetic path. Its main function is to carry the magnetic flux. In case of a synchronous generator, the current circulating in the rotor winding creates the magnetic flux in the core, which induces a current in the stator winding. Figure 1.2 shows a simple diagram of a stator core while figure 1.3 shows a picture of a magnetic core.

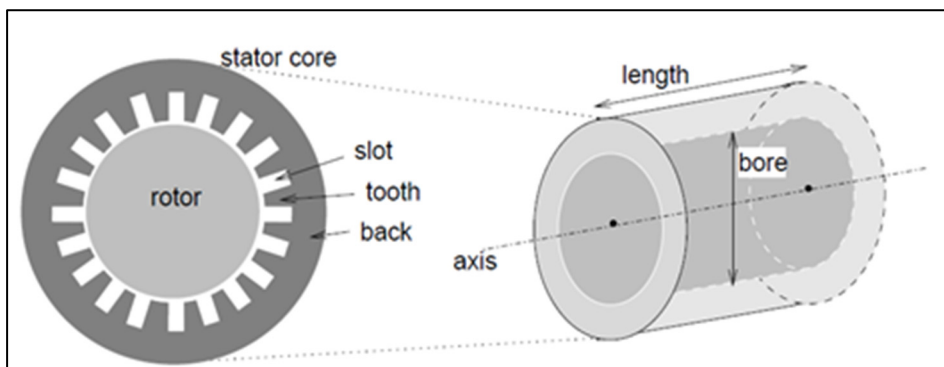


Figure 1.2 Image of a magnetic core
Taken from OMICRON (2021, p. 2)



Figure 1.3 Picture of a magnetic core being assembled
Taken from OMICRON (2021, p. 2)

The rotor is the rotating part and generally operates at voltages below 600 V_{DC} (Stone et al., 2014, p. 38). It is attached to the shaft which is connected to a mechanical device (e.g., turbine, pump, compressor, etc.). Its main function is to convert the mechanical energy into electrical energy by inducing a flux in the magnetic core in case of a generator. In case of a motor, the rotor delivers a mechanical torque to the mechanical load.

The stator winding is the stationary part and is responsible for inducing the magnetic flux into the core in case of a motor. In case of a generator, it is responsible for carrying the current induced by the circulating magnetic flux inside the core. They can operate at voltages up to 28 kV_{RMS} (Stone et al., 2014, p. 558) but typically in North America, it is common for high-voltage machines to operate at 13.8 kV_{RMS}. Their insulation systems can be subjected to high electric fields (e.g., in comparison to rotor windings). Due to additional constraint created by the high operating electric field, the construction of this insulation system is usually the most complex inside a rotating machine. Figure 1.4 shows a picture of a stator windings inserted inside a magnetic core.



Figure 1.4 Picture of a stator winding of a 230 MW turbo generator
Taken from Lachance & Oetl (2020, p. 435)

All these components are made from numerous different parts and a complete description is beyond the scope of this document. The following section describes the construction of stator windings.

1.2 Construction of stator windings

The stator winding is made of several turns of insulated copper conductors which are wrapped around the teeth of the magnetic core. To achieve this, individual coils or bars are inserted inside the stator core. The main difference between a coil and a bar is that one coil contains several turns, while a bar can be referred as a half turn. Bars are used in large machines while coils are used in medium size machines. A picture of stator coils sitting inside a simulated core is shown in figure 1.5 while a picture of stator bars is shown in figure 1.6.



Figure 1.5 Picture of stator coils
Taken from OMICRON (2023, p. 30)



Figure 1.6 Picture of stator bars
Taken from OMICRON (2023, p. 30)

When inserted inside the core, each coil or bar extends past the core edges, where they are connected in series or in parallel to form a complete winding. Some machines can have one or several windings connected in parallel per phase. In this case, each winding is formed of

several coils or bars connected in series. Figure 1.7 shows a sketch of a winding diagram with two windings per phase. Figure 1.8 shows an example of an actual winding diagram, which is used to illustrate the electrical circuit of the individual windings inside the core.

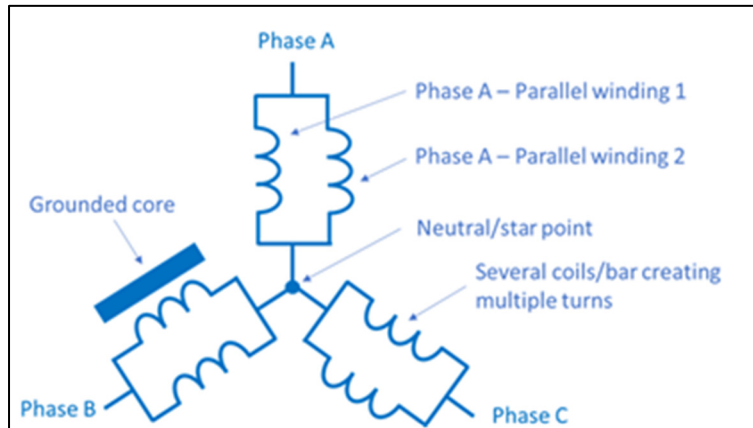


Figure 1.7 Simplified sketch of a three-phase electrical machine with two circuits per phase

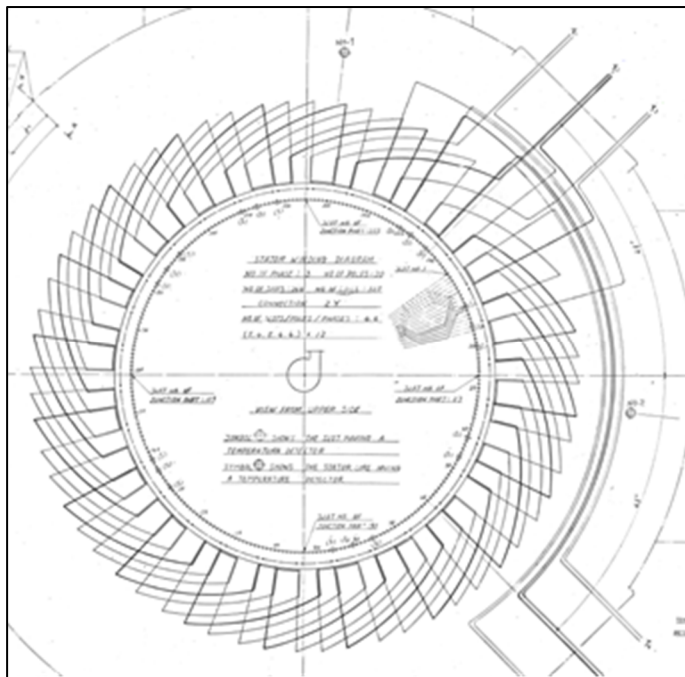


Figure 1.8 Picture of a stator winding diagram of a hydro-generator

The section of the coils or bars which is located inside the core is called the slot portion or the straight part, while the section extending past the core is named the endwinding or overhang area. Figure 1.9 shows a labeled picture of the slot portion and the endwinding area of a stator winding.

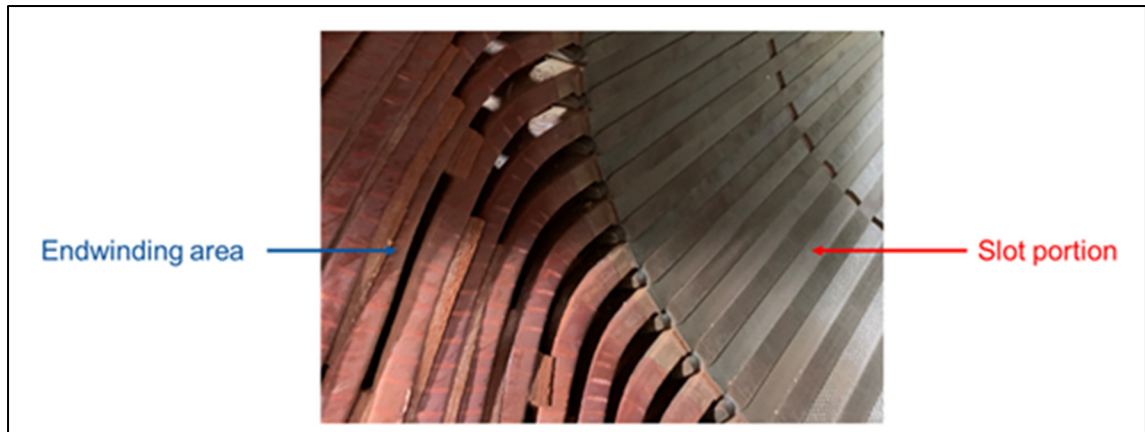


Figure 1.9 Picture of a stator winding making the distinction between the slot portion and the endwinding area

Stator coils and bars are made of conductive material (usually copper) in the middle, which is surrounded with electrical insulation, to prevent the center conductors which are energized at high-voltage potential during operation, from getting in contact with the grounded core. Depending on the voltage rating, different designs are used. If the conductors need to have a large cross-section area for higher current-carrying capability than several smaller subconductors, called strands, are used in parallel to improve the flexibility and to reduce eddy-current losses. Each strand must therefore be insulated from each other using a thin insulation layer. When coils are used instead of bars, it is frequent to have several turns per coil. Therefore, each turn must therefore be thinly insulated from each other's. Figure 1.10 shows a cross-sectional cut of a stator bar and a stator coil with three turns.

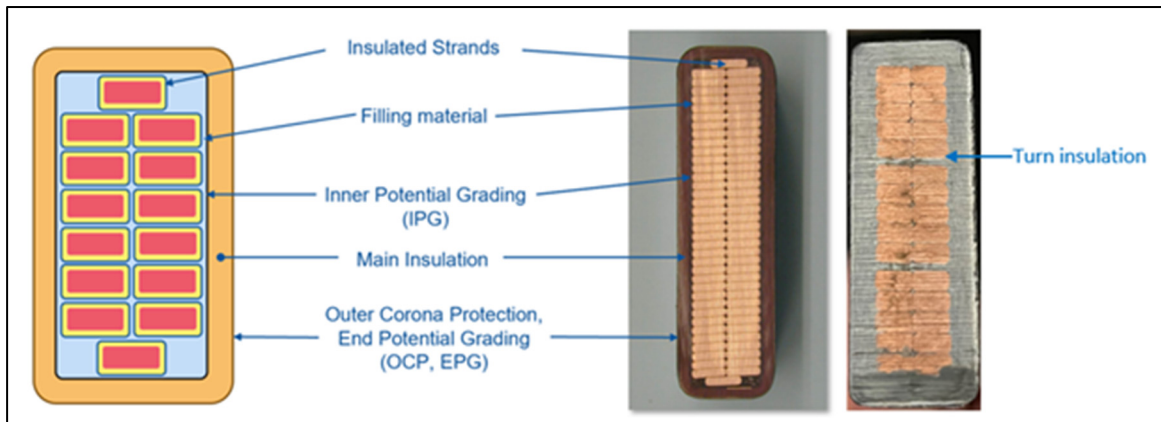


Figure 1.10 Cross-sectional cuts of a stator bar and a stator coil
Adapted from OMICRON (2023, p. 34)

For machines rated at 4 kV and above, a semi conductive layer, also referred to outer corona protection (OCP), is added to the surface of the coils and bars on the straight sections, which are within the stator core teeth. For machines rated at 6 kV and above, a stress grading relief coating, also called end potential grading (EPG), is added to the surface of the coils and bars, on both ends, when they exit the slots. The OCP and the EPG are connected through a small overlap section. Each component is explained in more details in the following sections.

1.2.1 Strand insulation

The strands are used for both mechanical and electrical reasons. If a solid conductor which is big enough to carry the needed current would be used, the coils and bars would be very difficult to bend to the desired shape. Therefore, using smaller conductors improves the flexibility and, makes it easier to shape the object to the desired shape.

It is well known that AC current tends to flow on the outside surface of a conductor. This phenomenon is called skin effect. For example, the skin depth of cooper is 8.5 mm at 60 Hz (Stone et al., 2014, p. 16). Therefore, in theory, if the conductor has a radius of more than 8.5 mm, there will be no current flowing past the skin depth. To improve efficiency and reduce I^2R losses, several small strands are used in parallel to form the main conductor.

Strands must be insulated from each other's to maintain their electrical benefits. The strand insulation must withstand only a few volts but must have good thermal properties. Nowadays, strand insulation is usually made of a combination of glass fibers and polyester.

1.2.2 Turn insulation

On medium size machines (usually 50 to 100 MVA), stator windings are made from coils which are connected in series. Each coil typically has between 2 and 12 turns. The voltage that each coil sees in operation is the line to ground operating voltage of the machine divided by the total number of turns in one winding. For example, in a 4,160-volt rated stator winding (or 2,400-volt rated line to ground), the winding may have 10 coils connected in series, with each coil consisting of 10 turns, for a total of 100 turns. The maximum voltage between turns in operation will be 24 V. Depending on the design of the machine, the voltage across each turn will range from 10 V_{RMS} to 250 V_{RMS} (Stone et al., 2014, p. 18).

In the past, the turn insulation and strand insulation used to be different. However, since the 1970s, many manufacturers use the same insulation for strands (previously described) and turns (Stone et al., 2014, p.18)..

1.2.3 Main or groundwall insulation

The main bundle of conductors is insulated from the stator core. This part of the insulation system is called the bulk insulation or the main insulation and is designed to withstand the full operating voltage of the machine. The main insulation is significantly thicker in comparison to the previously mentioned turn and strand insulation.

In general, an insulating tape is wrapped around the bundle of conductors. The main insulation tape nowadays mainly consists of glass carrier with mica flakes acting as barriers. Mica shows excellent electrical behavior with high specific resistance, high resistivity against partial discharges (PD) and decent thermal conductivity. The mica is then partly impregnated with a bonding agent, such as epoxy or previously polyester or asphalt, to increase the mechanical

strength of the insulation. The tape can be applied by hand or using machines. Figure 1.11 shows a picture of a taping machine.

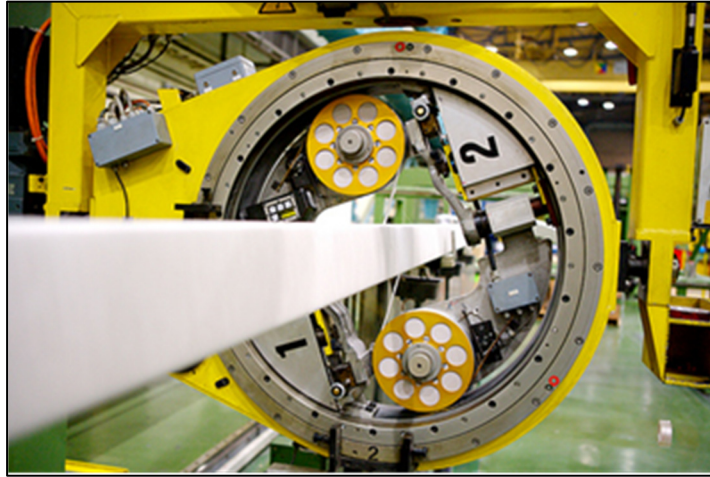


Figure 1.11 Picture of a taping
Taken from OMICRON (2023, p. 37)

There are two main manufacturing processes. The first alternative is named resin rich and defines the use of mica tape which is already impregnated by a B-stage or pre-cured epoxy. The coils are placed into a heated press, which squeezes out the excess of resin, filling-up the gaps between the different layers of tape. The other alternative is called vacuum pressure impregnated (VPI) and uses what can be described as dry tape. The coils are then put inside a tank, where vacuum is created, and epoxy resin injected prior curing.

1.2.4 Outer corona protection (OCP)

The outer corona protection (OCP) or groundwall partial discharge suppression refer to a semi-conductive layer which is applied in the straight section of the coil on top of the last mica tape layer. In operation, it is in direct contact with the magnetic core to bridge the microscopic air gaps that can occur between the uneven core laminations and the insulation of the coils or bars. This prevents the occurrence of partial discharges (PD). It is usually applied on machines with a rated voltage of 4 kV and above. Figure 1.12 shows an image where the OCP is used to bridge the microscopic gaps between the core and the insulation.

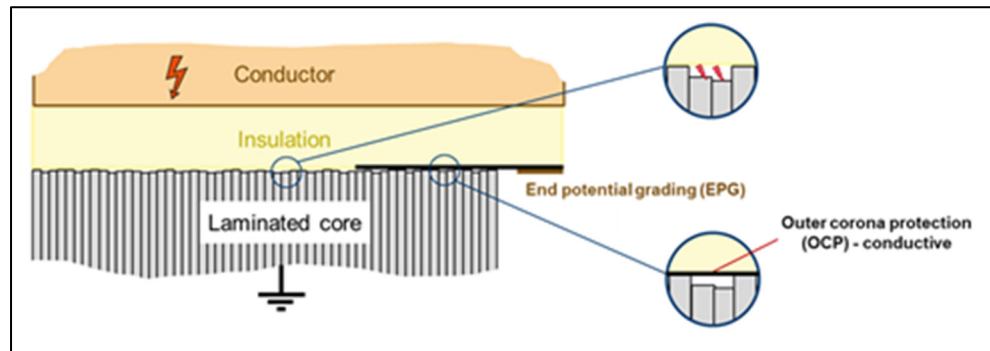


Figure 1.12 Image showing the use of OCP material
Taken from OMICRON (2023, p. 43)

1.2.5 End potential grading (EPG)

The end potential grading is a semiconductive area in the end winding of machines rated at 6 kV and above. It is installed where the coils transition from the slot section to the end winding area. This paint or tape is responsible for a defined and controlled reduction of the high electric field that would appear near the grounded core. Even if the insulation is applied in the end winding area, there is a capacitive coupling that exists which results of a high electric field area, near the grounded core, at the exit of the slots. Without the EPG, high tangential electric field would appear on the surface of the coil insulation near the magnetic core which could cause partial discharges. Nowadays, the main component of EPG is silicon carbide (SiC), which results in a non-linear conduction behavior. Figure 1.13 shows a picture of a stator coil with the OCP and EPG identified. Figure 1.14 shows the theoretical electric field distribution when an energized conductor exits a grounded enclosure without the use of stress grading methods. Figure 1.15 shows the difference in energized components with and without EPG.

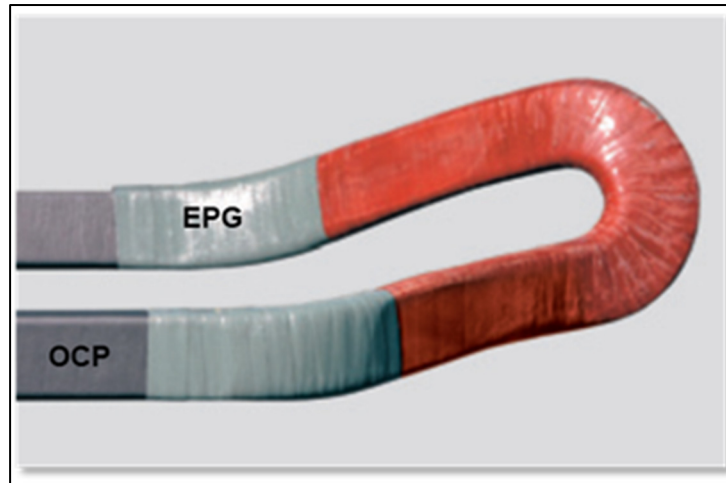


Figure 1.13 Picture of a stator coil showing the OCP and the EPG area
Taken from OMICRON (2023, p. 42)

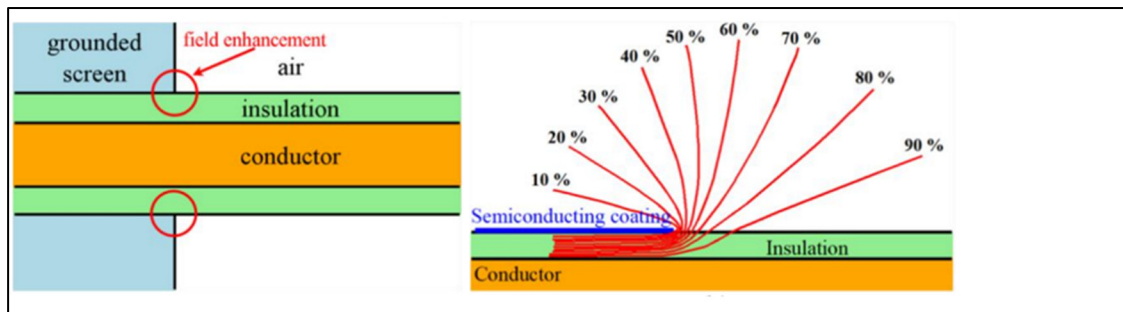


Figure 1.14 Energized insulated conductor passing through a grounded metallic screen. (left) Typical configuration. (right) Equipotential lines and stress distribution
Taken from Can-Otiz et al. (2021, p. 2)

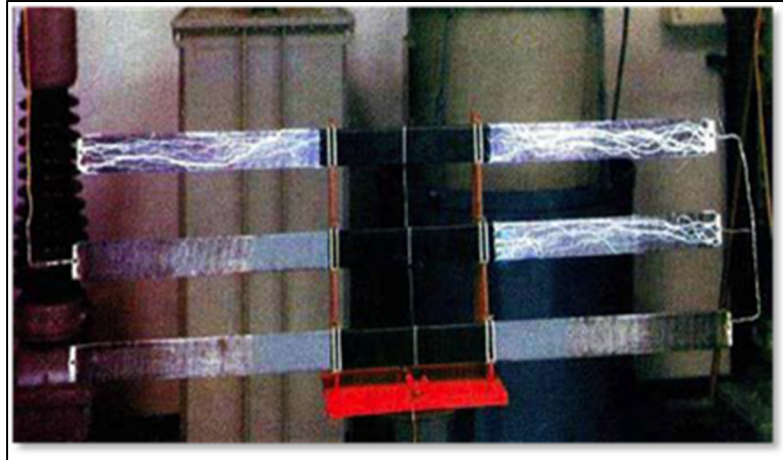


Figure 1.15 Picture of an experiment showing the discharges occurring when no EPG is used
Taken from OMICRON (2023, p. 45)

1.2.6 Other components

In addition to the aforementioned components, fillers are added in the surroundings of each coil, in the slot section. There are different solutions available on the market, but they all serve the purpose of maintaining the coils in place during operation. Wedges are also added on top of each slot sections, which lock and maintain the coils in place inside each slot. Another component that is sometimes see is the inner corona protection (ICP). The ICP serves a similar function than the previously mentioned OCP but, is installed as the first layer, next to the bundle of main conductors. It is generally installed on very high-voltage machines (Stone et al., 2014) and is not covered in this work.

CHAPTER 2

DEGRADATION MECHANISMS AND CURRENT ELECTRICAL DIAGNOSTIC METHODS FOR STATOR WINDINGS

2.1 Degradation mechanisms in stator windings

Degradation can be defined by the losses of effectiveness of a specific object to perform a given task. Therefore, for stator winding insulation systems, this can be seen as the reduction of electrical insulation properties. If left unattended, the outcome can be an in-service failure which results in damaged components and temporary loss of production. In the worst case, an in-service failure can result in the complete and permanent loss of the asset, in addition to create a significant safety hazard for nearby personnel.

As emphasis by Stone (2014), most of the time, failure does not happen suddenly but, is rather the result of a progressive deterioration process affecting the properties of the insulation system, until it can no longer sustain the operating voltage, or a transient event.

There are numerous causes that can initiate and sustain such degradation process. Several statistics regarding the causes of failure in high voltage rotating machines are available: (Evans, 1981), (Bomba, Gross & Kaiser, 2005) and (CIGRE, 2003). The survey carried out by CIGRE study committee SC11 EG11.02 (CIGRE, 2003) provides the results of an investigation of the root cause of 69 hydro generators failures. From these results, 56% showed insulation damage, while the other major contributors were being attributed to mechanical, thermal and bearing damages, as depicted in figure 2.1.

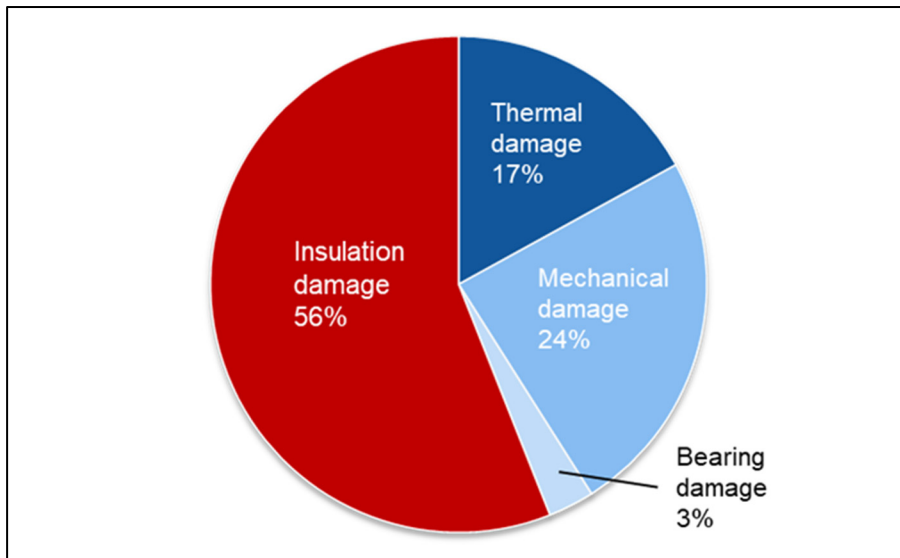


Figure 2.1 Attributed causes of failure from 69 hydro generators
Taken from OMICRON (2023, p. 4)

Usually, the degradation process is gradual and is caused by one or a combination of stresses. For stator windings, the acronym TEAM, used for thermal, electrical, ambient, and mechanical, is often used to describe the most common families of stresses encountered by operating rotating machines.

2.1.1 Thermal stress

Stator winding insulation systems are inherently thermally stressed during operation. The high operating temperature can lead to the oxidation of the organic insulation of stator windings (Stone et al., 2014, p. 49). Overtime, this process tends to separate the different layers of mica papers and create voids and/or delamination in the winding. Those voids can lead to partial discharges (PD), which will deteriorate slowly the epoxy between the tape layers. It also tends to make the insulation more brittle. Another well-known thermal degradation process is due to load cycling of the rotating machines. This usually creates a thermal cycle in which, the components expand when the machine is operating at high load and shrink when operating at low load. The copper used in the main conductor bundle and the insulation compound used as the main insulation have different expansion coefficients. Therefore, if this process happens too rapidly, debonding of the main conductor stack and the main insulation can happen.

2.1.2 Electrical stress

The main electrical stress present in high-voltage stator windings is partial discharges. PDs are small and located dielectric breakdowns which only partially bridge the insulation (IEC, 2015, p. 8). When it happens, a local bombardment of electrons and ions will occur, which will break the chemical bonds of organic material (Ravindra & Wolfgang, 2022). Over time, PD will erode the insulation enough to decrease the dielectric strength of the insulation until failure happens.

The main causes of PDs in stator windings are:

- Internal discharges occurring in the main insulation because of voids and delamination.
- Slot discharges which refer to discharges occurring between the insulation and the magnetic core, in the slot. This can occur for example if no OCP layer is added to the insulation, if the OCP layer is abraded because of excessive vibration while the machine is in operation or, because of other ageing mechanisms.
- PD occurring at the transition from the slot section to the end-winding area. This could occur if the compound used for the EPG is not conductive enough or not applied over a sufficient distance. PD can also occur due to the degradation of the EPG over time, because of ageing.
- Discharges between bars in the endwinding area because of bad clearances or contamination.

2.1.3 Ambient stress

Ambient stresses refer to many external factors of the machines. Most often, ambient stresses are the results of an accumulation of a foreign substance on the surface of the insulation. Most notably, oil leaking from bearings, dust or by-products of a manufacturing process, moisture, and carbon powder from exciter brushes. The most common outcome is an increase of operating temperature or/and surface discharges on the outside of the insulation.

2.1.4 Mechanical stress

The operation of rotating machines creates different electromechanical forces. One mechanical stress is caused by the power frequency current circulating in the windings, which will give rises vibration of the coils if they are not adequately maintained in place (Stone, 2014). This vibration can lead to the abrasion of the OCP, and eventually, the abrasion of the main insulation.

2.2 Current electrical diagnostic methods for stator windings

Electrical tests are conducted for a variety of reasons on stator windings. They are performed to verify the quality of newly manufactured components, to assess newly installed windings, to periodically verify the insulation as maintenance tests, for diagnostics in case of problems and for failure root cause analysis or remaining life assessment. Therefore, a variety of electrical tests have made their way into asset operator's testing procedures. Some of those tests are performed online, while the machine is in operation while others are performed offline, with the machine being removed from service and disconnected from the network.

On an operation perspective, there is usually a preference for online diagnostic methods. The reasons are that no outage is required to perform the tests and that usually, only one person is needed to collect the data, which makes the test rather inexpensive (in comparison with offline tests). During those tests, the machine is also operating under actual conditions and therefore, the effects of vibration and temperature will be taken into consideration while collecting the data. On a maintenance and diagnostic perspective, offline testing is usually preferred as, there are far more tests which can be performed. Most of those tests will also provide more information in comparison with the data collected online.

The investigations described in this document are focused on the diagnostics of high-voltage electrical machines using offline diagnostic methods. The following section describes some of the most performed offline electrical tests for stator winding insulation system. For a more comprehensive list of offline and online diagnostic methods, the readers can consult the following references (Stone, 2014) and (IEEE, 2016).

2.2.1 Insulation resistance

Insulation resistance (IR) is defined as the ratio of the voltage and the current after the application of a DC voltage between the main conductor bundle and the ground. It is measured by applying a DC voltage step across the insulation (most of time, negative) and measuring the current using an ammeter. The resistance can therefore easily be obtained using Ohm's law.

The resistance value obtained after 60 seconds of application is the typical reported IR value. The higher measured value, the better is the condition of the insulation. For more information regarding this test, readers can refer to (Gupta & Culbert, 1992) and (IEEE, 2014).

2.2.2 Polarization index

The polarization index (PI) is the ratio of insulation resistance, as described in section 2.2.1, at ten minutes (600 seconds) to the one measured after one minute (60 seconds). The big advantage of the PI value over IR is that it is less temperature and geometry dependent. The value measured after 1 minute usually includes the polarization losses, conduction losses and surface leakage losses while the value measured after 10 minutes, includes in theory, only the conduction and surface leakage losses. The ratio between the value measured at 10 minutes and the one measured at 1 minute is an indication of how important the conduction and surface leakage losses are in comparison with the total losses. Generally, if the PI is below 2, the winding is considered wet or contaminated and not fit for operation. If the PI is above 2, the winding is considered satisfactory for operation. For more information regarding this test, readers can refer to (Gupta & Culbert, 1992) and (IEEE, 2014).

2.2.3 Polarization and depolarization current analysis

In a PDC measurement, A DC voltage is applied, between the main conductor bundle and ground, for a duration of 10 minutes or more. The winding is then discharged to ground through an ammeter. During both stages, the current is measured continuously and typically reported every second on a graph. When switching to the discharge current, the time is reset to zero to superimpose the measured charging current and the discharge current, using a logarithmic scaling for display. The discharge current is also displayed as a positive current to facilitate the

comparison with the charging current. The difference between the curves is used to perform the assessment, as well as the shape of the curves. Other values can also be derived and used of the assessment. For more information regarding this test, readers can refer to (IEEE, 2014), (Hudon, Amyot, Bernier, David & Essalini, 2018) and (Soltani & David, 2006).

2.2.4 Direct-voltage ramp test

Starting from zero, a DC voltage is applied and increased linearly at a constant rate between the main conductor bundle and ground while the current is measured. The current is plotted on a two-dimensional diagram, in reference to the applied voltage. Since the voltage is increased linearly at a constant rate, the current will theoretically stay close to a constant value equaled to the rate of voltage increase multiplied by the test object capacitance. The assessment is performed by looking at the shape of the measured current curve. A deviation from the expected linear current curve is an indication that the insulation is compromised. For more information regarding this test, readers can refer to (IEEE, 2002) and (Hudon, Amyot, Bernier, David & Essalini, 2018).

2.2.5 Dissipation factor measurement

The dissipation factor measurement is a measurement of the losses in the insulation. An AC voltage near or at power frequency (typically 50 Hz or 60 Hz) is applied between the conductor bundle and the ground. The current flowing in the test object is measured using a shunt resistor and compared to a current which is in quadrature to the applied voltage. This current is called reference current. This reference current is obtained by connecting a low loss capacitor in parallel to the test object and measuring the current flowing through it. The higher the losses, the more at risk is the insulation. Certain deterioration processes, such as thermal ageing, conductive contamination and moisture absorption will increase the losses over time. Therefore, trending this value can reveal if the winding has deteriorated over a given period of time.

A variation of the test called tip-up is also commonly performed. The tip-up test is the ratio between two different loss values measured at two different voltages. It is an indirect way of

measuring partial discharges. Traditionally the measurement has been performed at 20% of the rated line to ground voltage and at 100 % of the line to ground voltage. The measurement at 20% is meant to only include the losses from the polarization processes and from the leakage current while the measurement at 100% will also include the losses from partial discharge activities. For the measurement performed on individual components such as coils and bars, the test is performed using guard electrodes, which removes the loss contribution from the EPG. When the test is performed in the field on complete stator winding, the loss contribution from the EPG cannot be mitigated and gives rise to an elevated tip-up, regardless of if significant PD activities is present or not. This will be addressed in more details later in this document. For more information regarding this test, readers can refer to (IEEE, 2001) and (IEC 2015).

2.2.6 Partial discharge measurements

The partial discharge test measures the current pulses that is created by a PD activity within an insulation system. The theory of PD is very comprehensive, and a complete description is beyond the scope of this document. However, a basic understanding of the phenomenon is provided and is helpful from this point onward. A PD is a localized dielectric breakdown of a small portion of an insulation system under electrical stress (IEC, 2015, p.8). They can occur when the local electric field exceeds the local dielectric strength, at a given location, within or at the surface of an energized dielectric. Typical examples of such locations are void within solid or liquid insulation systems and protrusions. For stator windings of high-voltage electrical machines specifically, those defects can be a sharp edge adjacent to the main conductor bundle, imperfections in the taping process of newly manufactured components, thermal degradation of the polymer, mechanical stress from vibration and mechanical stress from thermal expansion. This was emphasized by (Vogelsang & al., 2003), (Vogelsang & al., 2006) and (Bruetsch & al., 2008) Each PD event creates localized heating and deteriorates the insulation by eroding the organic material.

PD events generate current pulses. At its origin, if the discharge occurs in atmospheric air, this pulse has a rise time of just a few nanoseconds and contains a theoretical constant broad

frequency spectrum, from DC to up to several hundred of megahertz (MHz). Therefore, PD can be detected using different technologies.

For individual components and complete stator windings, the test is usually performed according to IEC60270, IEC60034-27-2 (IEC, 2015) or IEEE 1434 (IEEE, 2014). The winding is energized using a sinusoidal alternative voltage at power frequency for the measurement and the voltage level is increased by steps. A coupling capacitor is installed in parallel to the winding, connected at the line terminal of the machines. When a PD occurs, it generates a current pulse that will travel from the defect site to the coupling capacitor. A measuring impedance is connected in series with the coupling capacitor to capture the PD current pulse and send it to a PD instrument. PD magnitude is most often expressed using the apparent charge, in picocoulombs or nanocoulombs. Typically, the higher the value, the more deterioration there is. For more information regarding this test, readers can refer to (IEEE, 2014), (IEC, 2006) and (IEC, 2012).

CHAPTER 3

ELECTRIC PROPERTIES OF DIELECTRIC MATERIALS

There are two main families of materials when looking at their electrical properties, conductors, and insulators (also called dielectric materials). Conductors have a significant number of free charges and therefore, as their name implies, have good conductivity properties when immersed in an electric field. On the other end, in ideal dielectric materials, there is no free charges because all positive and negative charges are bound together. A third category of materials also exists, the semiconductors. However, they are not included in this work.

In this chapter, the focus is on the description of electric properties of solid dielectric materials which are used in stator winding insulation systems.

3.1 Conduction in dielectric materials

In dielectric materials, there are no free charges and therefore, charge transport is mainly created by ionic conduction and not by the movement of electrons. Ions can be introduced in dielectric materials for different reasons (manufacturing, impurities, contaminations, etc.). These ions can move under the influence of an external electric field. Unlike polarization mechanisms, conduction is a continuous phenomenon and results in a constant current proportional to the external applied electric field (Fournie & Coelho, 2000).

The conductivity of a specific material is usually express as the dc conductivity σ_{dc} . Another commonly used parameter to describe the conductivity is the dc resistivity ρ_{dc} such as:

$$\rho_{dc} = \frac{1}{\sigma_{dc}} \Omega \cdot m \quad (3.1)$$

3.2 Electric polarization in static electric field

As mentioned previously, there are no free charges in ideal dielectric materials. Instead, the positive and negative charges are bound together as the molecules, atoms and ions of that material share their electrons. In the absence of external electric field, the molecules in a dielectric material are usually distributed so there is no existing internal electric field. However, when a dielectric material is exposed to an external electric field, the charges can't move freely to the boundaries of the dielectric material. Instead, they tend to move locally (vibration, rotation, distancing between negative and positive charges) to align themselves in the direction of the electric field. At a microscopic level, this results in localized changes in the field distribution inside the dielectric material. In a more macroscopic level, it also results in an overall electric field which is opposite to the external applied electric field. This phenomenon is called polarization.

3.2.1 Introduction to electric polarization

Electric polarization mechanisms can be caused by the orientation of permanent or induced electric dipoles when immersed in an external electric field (David, 2010). An electric dipole has two electric charges q of opposite polarity that are separated by a given distance \vec{l} , as shown in figure 3.1.

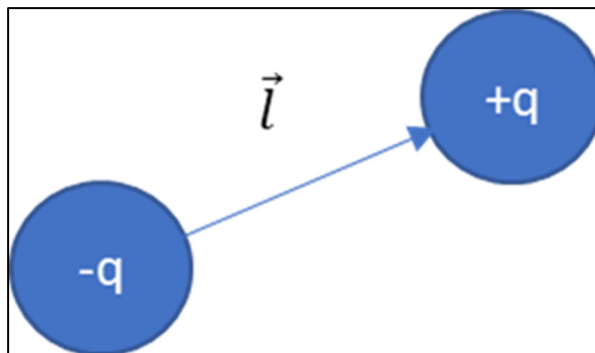


Figure 3.1 Electric dipole
Adapted from Fournie & Coelho (2000, p. 3)

Permanent dipoles are produced by asymmetrical molecules that have a permanent displacement of the positive and negative charge centers even without external field applied. Typical examples of polar materials are water (H₂O), polyvinyl chloride (PVC) and some epoxy resins. On the other hand, induced dipoles are created by the separation of positive and negative charges when expose to an electric field. When the electric field is removed, the atoms of such molecules return to their original distribution.

A specific dipole moment is defined by the following equation:

$$\vec{p} = q\vec{l} \quad (3.2)$$

Since the location and charge magnitude of each dipole within a dielectric material is generally unknown, their behavior is usually expressed as a vector summation of all dipole moments per unit volume. This is done by introducing the electric polarization vector \vec{P} .

$$\vec{P} = \frac{1}{\Omega} \sum_{i \in \Omega} \vec{p}_i \quad (3.3)$$

where Ω is the volume in the dielectric. Without external electric field being applied to the dielectric material, the dipoles are randomly oriented, and the overall vector summation \vec{P} of their dipole moment is zero. When an external electric field \vec{E} is applied to the dielectric material, the dipole moments will align themselves with the direction of the electric field. This alignment is caused by the electromotive force that is created by the electric field (Serway & Jewett, 2009). Figure 3.2 shows the orientation of the dipoles prior and after the application of an external electric field.

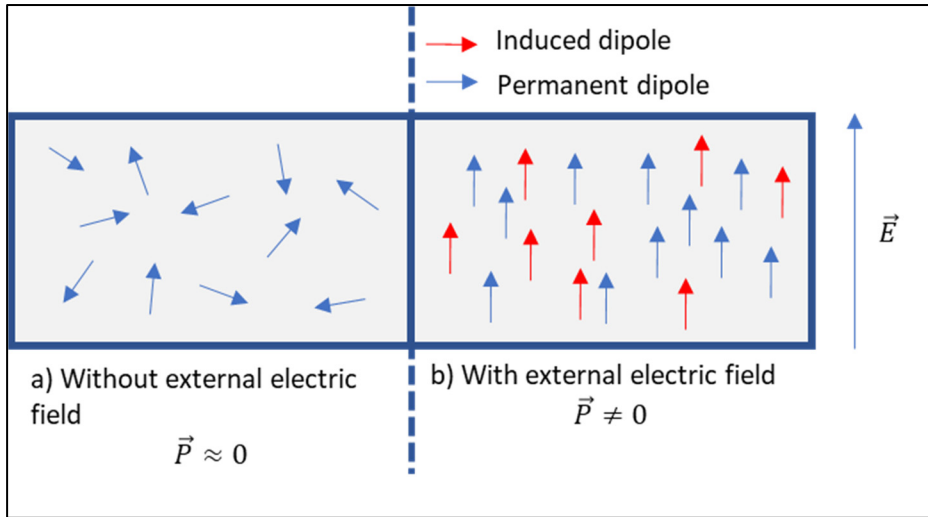


Figure 3.2 Electric polarization from a dielectric material

In theory, the polarization of dielectric materials can be proportional to the applied external electric field, in case of linear dielectric, or can be disproportional to the applied external electric field, in case of non-linear dielectric. However, in practice, almost all dielectric material used in electrical apparatus can be considered linear. Even when nonlinear dielectric materials are used, the applied electric field is usually low enough for the dielectric to operate in the linear region of their polarization curves \vec{P} vs \vec{E} (David, 2010).

3.2.2 Electric permittivity

Polarization mechanisms are usually quantified using the permittivity ϵ . The higher the value of ϵ is for a specific insulation system, the more polarization mechanisms there are inside the material upon the application of an electric field. Let's use an example to explain what this term concretely means. Two electrodes are installed on the boundaries of a vacuum space and a static electric field \vec{E} is applied as illustrated in figure 3.2. A surface charge density σ_0 is created on each electrode as to maintain the electric field across the vacuum space. This surface charge density is defined by the following equations:

$$\sigma_0 = \vec{D}_0 \cdot \vec{n} \quad (3.4)$$

where \vec{n} is a vector that is orthogonal to the direction vectors to the plane and \vec{D}_0 is the charge density vector of vacuum and is defined by the following equation:

$$\vec{D}_0 = \epsilon_0 \vec{E}_0 \quad (3.5)$$

ϵ_0 is the vacuum permittivity ($\epsilon_0 = 8,85 \times 10^{-12} F/m$). Here, since no dielectric material is present, we define $\vec{E} = \vec{E}_0$.

Now, let's introduce a dielectric material between the same two electrodes, as shown in figure 3.3.

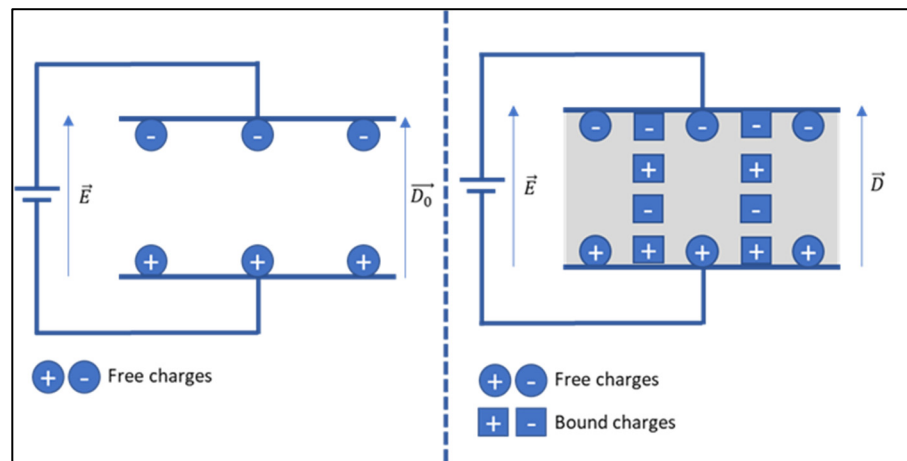


Figure 3.3 Charge accumulation on the surface of the electrodes (left: surface charge accumulation in vacuum and right: charge density created in a dielectric material)

As explained earlier, the dipoles will align themselves with the applied external electric field (polarization) and therefore, a charge density σ_p will be created to compensate the effect of polarization. The total charge density \vec{D} then becomes:

$$\sigma_p = \vec{P} \cdot \vec{n} \quad (3.6)$$

$$\vec{D} = \vec{D}_0 + \vec{P} = \epsilon_0 \vec{E}_0 + \vec{P} \quad (3.7)$$

Since only linear dielectric materials are considered, the polarization \vec{P} is proportional to the electric field \vec{E} and therefore, the following equation can be written:

$$\vec{P} = \epsilon_0 \chi \vec{E} \quad (3.8)$$

Where χ is the dimensionless electric susceptibility. In linear and isotropic dielectric materials, this term is constant and independent of the magnitude of the electric field \vec{E} . The susceptibility can also be expressed as the ratio of the charge density of the space filled with a dielectric \vec{D} over the charge density \vec{D}_0 of vacuum. The absolute permittivity ϵ of a material can be defined by introducing the relative permittivity ϵ_r of a specific material following this equation:

$$\vec{D} = \epsilon_0 (1 + \chi) \vec{E} = \epsilon_0 \epsilon_r \vec{E} = \epsilon \vec{E} \quad (3.9)$$

In general, for practical application of electrical insulation systems, a lower permittivity is preferred as fewer dielectric losses are expected. A few examples of relative permittivity of dielectric materials used in stator winding insulation systems are shown in table 3.1. It is important to mention that permittivity values are not constant and can be dependent on temperature and the frequency of the electric field (Kuchler, 2018).

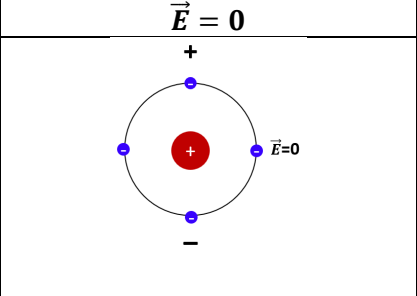
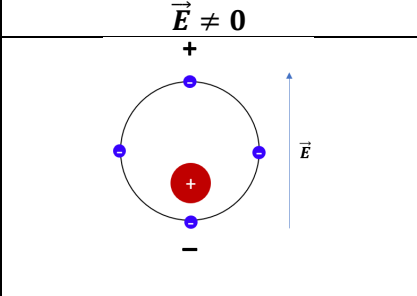
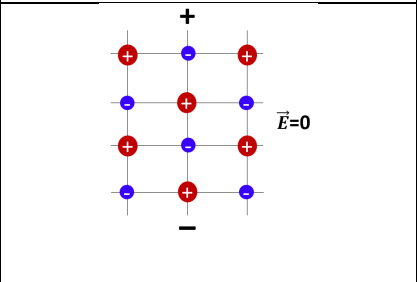
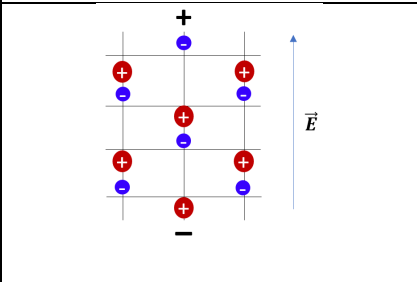
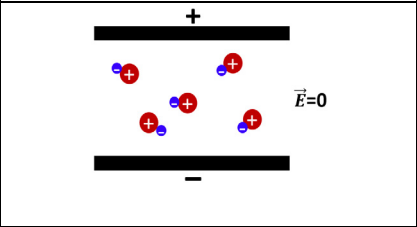
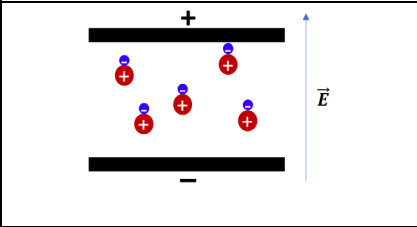
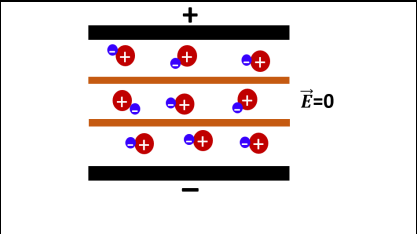
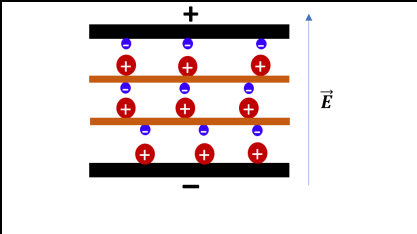
Table 3.1 Relative permittivity of different materials

Material	Relative permittivity
Vacuum	1
Air	1.0006
Polyester resin	2.8 - 4.5
Epoxy resin	3.5 – 5.8
Asphalt	4 - 10
Mica	7

3.2.3 Electric polarization mechanisms

In the previous section, the electric polarization was described as one global behavior. However, there are different types of polarization mechanisms. Some can involve larger local displacement as others can be quicker to appear following the application of an external electric field. It is important to mention that under a constant electric field, the electric polarization is not a continuous phenomenon. It has a finite time and will not contribute to a continuous current. Table 3.2 summarizes the main polarization mechanisms involved in typical insulation systems.

Table 3.2 Schematics of different polarization mechanism
Adapted from David (2010, p.6)

Polarization mechanism	$\vec{E} = 0$	$\vec{E} \neq 0$
Electronic or atomic		
Molecular or grid		
Orientalional		
Boundary or interfacial		

Electronic or atomic polarization are the results of induced dipoles. The positive nucleus and the negative electron clouds are shifted according to the applied electric field. The molecular or grid polarization is also caused by induced dipoles. Those molecules are built up by atoms that are bound together. Their electron distribution is symmetrical and therefore, they have no permanent dipole moments when no electric field is applied. When an electric field is applied, the electrons and nuclei will shift, and the atoms remain bond together. Electronic and molecular polarization happen very quickly following the application of an external electric field (optical and infrared frequencies).

Orientational polarization occurs when an electric field is applied to polar molecules. Those molecules have permanent dipole moments and when there is no external applied electric field, they are randomly oriented as to have no overall polarization. However, when an electric field is applied, the molecules will tend to align themselves in the direction of the electric field.

Interfacial polarization doesn't occur in homogenous insulation systems. However, there are several practical applications where inhomogeneous insulation systems are used. Common examples are the oil-paper insulation system used in power transformers or the epoxy-mica insulation system used in stator windings. In inhomogeneous insulation systems, induced dipoles are created by the separation of positive and negative charges at the boundaries of two dielectric materials with different permittivity or conductivity.

Permittivity values can be influenced by temperature and the frequency of the applied electric field. The mobility of some dipoles increases with temperature. Therefore, as temperature increased from their frozen stage, an increase relative permittivity is expected. If the temperature is further increased, the relative permittivity decreases because of the destruction of dipole orientation due to thermal agitation and collisions. In short, the influence of the electromotive force is reduced in comparison to the random thermal agitation of the molecules. In addition, mass inertia and interaction of the dipoles can create time delays between the electric field application and the dipoles. This affects mainly larger dipoles and is less applicable for electrons. Therefore, among the previously described polarization mechanisms, some of them occurs almost instantaneously following the application of the electric field (electronic and molecular) while others might take more time before occurring (orientational and interfacial). Generally, the relative permittivity decreases with increasing frequency in steps, which are associated with the stepwise drop-out of different polarization processes (Kuchler, 2018).

3.3 Electric polarization in time domain

Most of the phenomena described in the previous sections were for constant electric field, meaning \vec{E} is constant and the effect of time on the polarization processes was not discussed.

However, in practical application, the applied electric field \vec{E} is time dependent and so are the polarization mechanisms.

Let first consider the simple example of a heterogenous dielectric made of a layer of vacuum and a layer of a solid dielectric material as shown in figure 3.4.

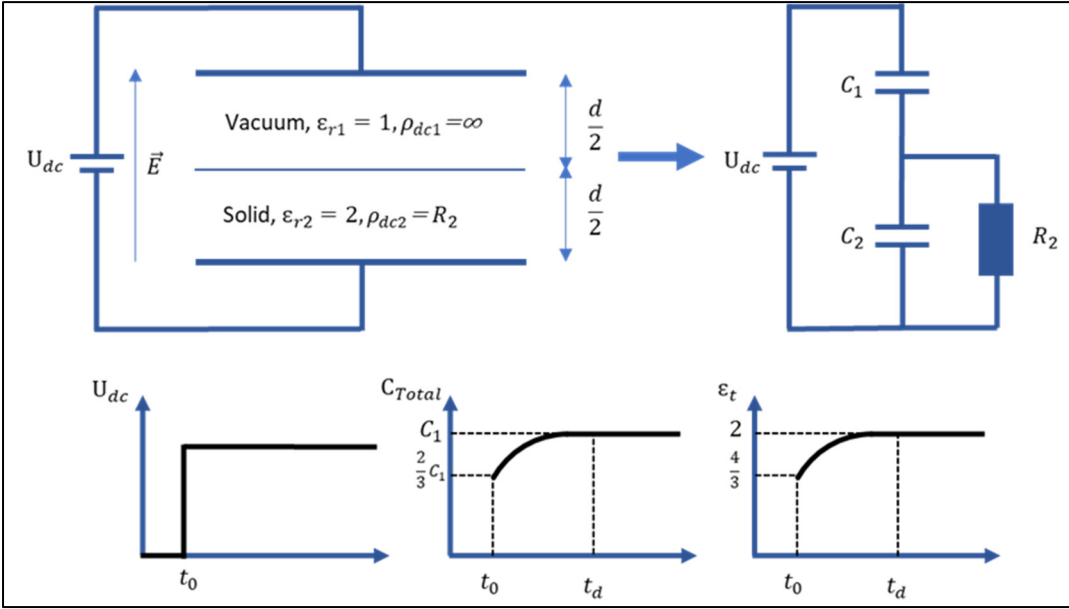


Figure 3.4 Polarization under direct voltage
Adapted from Ravindra & Wolfgang (2022, p. 353)

Before the application of a voltage (at $t < t_0$), the capacitance of such system is given by:

$$\frac{1}{C_{Total}} = \frac{C_1 C_2}{C_1 + C_2} \quad (3.10)$$

Since ϵ_{r2} is equal to $2\epsilon_{r1}$, C_2 is equal to $2C_1$ and C_{Total} is equal to $\frac{2}{3}C_1$.

The capacitance of a system is directly linked to the relative permittivity as given by:

$$C = \frac{\epsilon \cdot A}{d} \quad (3.11)$$

Therefore, before the application of a voltage (at $t < t_0$), the total relative permittivity of such system is given by:

$$C = \frac{\epsilon \cdot A}{d} \quad (3.12)$$

$$\epsilon_t = \frac{4}{3}$$

Following the application of a DC voltage at $t=t_0$, a displacement of charges occurs in the vacuum space and in the solid dielectric in opposition to the sudden application of the electric field. The capacitance C_2 is then progressively discharged in the resistance R_2 . Let's consider t_d the time where C_2 is completely discharged. At that time, the full voltage is across C_1 . Therefore, after a delay of t_d , the total capacitance of the system is equal to C_1 . If $C_{Total} = C_1$, the total permittivity becomes:

$$\frac{\epsilon_t \cdot A}{d} = \frac{\epsilon_{r1} \cdot A}{\frac{d}{2}} \quad (3.13)$$

$$\epsilon_t = 2$$

This time is referred to as relaxation time. It varies depending on the polarization mechanisms and the dielectric materials involved.

To consider the time dependency of the electric field, the following equation is introduced:

$$D(t) = \epsilon_0 E(t) + P(t) \quad (3.14)$$

It was previously mentioned that there is a time delay between the application of the electric field and the movements at a microscopic level. As an example, let's consider the application of a voltage step of a short duration (Δt) which is applied across two electrodes over a dielectric material. To consider that time delay, the dielectric response function $f(t)$ is introduced as follows:

$$P(t) = \epsilon_0 (E \Delta t) f(t) \quad (3.15)$$

In electrical engineering applications, it is more practical to express these phenomena using voltage and current. The complete mathematical development is available in (David, 2010). Following the application of a voltage step such as:

$$U(t) = \begin{cases} 0, & \text{for } t < 0 \\ U_0, & \text{for } 0 \leq t \end{cases}$$

The following equation is obtained for the current circulating in the dielectric:

$$I(t) = \frac{C_0\sigma}{\varepsilon_0} U_0 + U_0 C_0 [\delta(t) + f(t)] \quad (3.16)$$

The term $\frac{C_0\sigma}{\varepsilon_0} U_0$ represents the direct current (DC) contribution and is caused by the conduction phenomenon described in section 3.1. The second term represents the current induced by the movement of free charges at the surface of the electrodes or also called displacement current. The last term is the current contribution from the different polarization mechanisms. The polarization can be divided into fast polarization processes and slow polarization processes. The fast polarization processes occur almost instantly following the application of the electric field while there is a delay before the slow polarization processes occur.

Now, let's consider the case where a short-circuit is applied across the dielectric material after a time t_c such as:

$$U(t) = \begin{cases} 0, & \text{for } t < 0 \\ U_0, & \text{for } 0 \leq t \leq t_c \\ 0, & \text{for } t > t_c \end{cases}$$

The equation of the current becomes:

$$I(t) = \begin{cases} \frac{C_0\sigma}{\varepsilon_0} U_0 + U_0 C_0 [\delta(t) + f(t)], & \text{for } 0 \leq t \leq t_c \\ -U_0 C_0 [\delta(t - t_c) + f(t - t_c) - f(t)], & \text{for } t > t_c \end{cases} \quad (3.17)$$

The current circulating after t_c is called the discharge current while the current prior t_c is called the charging current. Both currents (charging and discharge) are nearly symmetrical. During the discharge phase, there is no conduction anymore since no voltage is applied. The discharge current also has an additional polarization equation $f(t)$, which represents the memory effect of the dielectric (Jonscher, 1983). For a long charging time, the contribution of the memory effect becomes insignificant (David, 2010).

Every dielectric material has their own dielectric response function $f(t)$. Attempts have been made in the past to have general models to describe the dielectric response functions of different dielectric materials (Helgeson, 2000). Figure 3.5 shows the measured charging and discharge currents on a newly manufactured 175 MVA hydro generator.

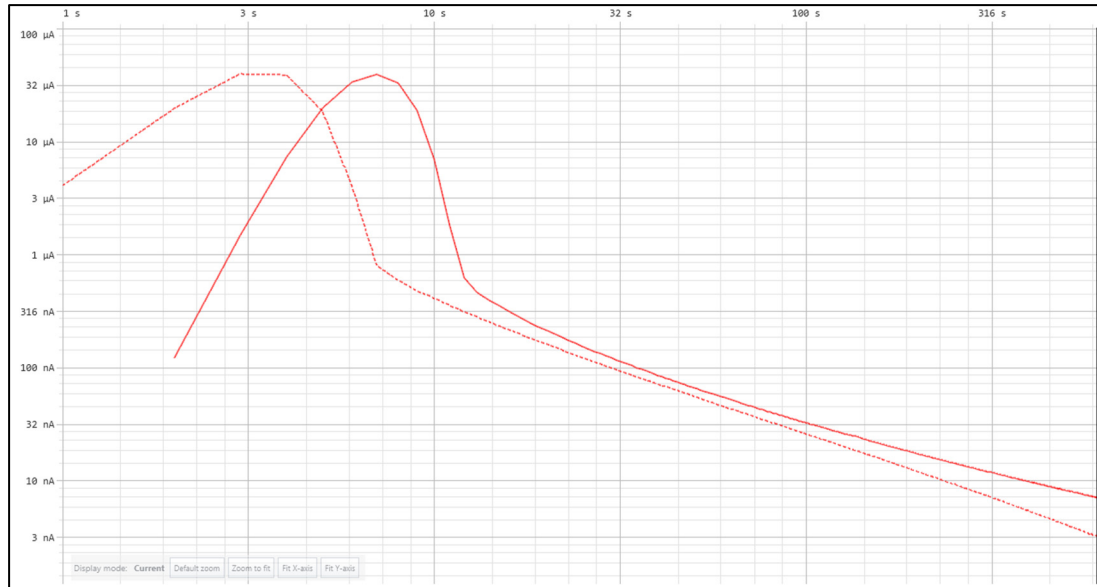


Figure 3.5 Example of a measured polarization (solid) and depolarization (dash) current on a hydro generator

3.4 Electric polarization in variable field

Most of the electric insulation systems used in stator windings are subjected to alternative sinusoidal electric field such as

$$E(t) = E_{peak}[\sin(\omega t) + \phi] \quad (3.18)$$

Therefore, it makes sense to discuss the electric polarization behaviors in the frequency domain. It is possible to obtain the conversion of equation 3.16 using Fourier transform. The mathematical conversion is available in (David, 2010). This conversion results in the following equation for the circulating current when a dielectric material is stressed by a periodic sinusoidal electric field.

$$I^*(\omega) = \omega C_0 \left[\left(\frac{\sigma}{\omega \epsilon_0} + \epsilon_r''(\omega) \right) + j \epsilon_r'(\omega) \right] U^*(\omega) \quad (3.19)$$

The terms $\frac{\sigma}{\omega \epsilon_0}$ and $\epsilon_r''(\omega)$ respectively represents the conduction losses, created by the conduction current, and the dielectric losses, created by the polarization mechanisms. For an ideal dielectric material, it can be assumed that $\frac{\sigma}{\omega \epsilon_0} = \epsilon_r''(\omega) = 0$. Therefore, the current is leading the voltage by a phase angle of 90° . As the losses increase in a dielectric material, the phase angle between voltage and the current decreases. Figure 3.6 shows the phase diagram of the current and the voltage for a lossy dielectric material.

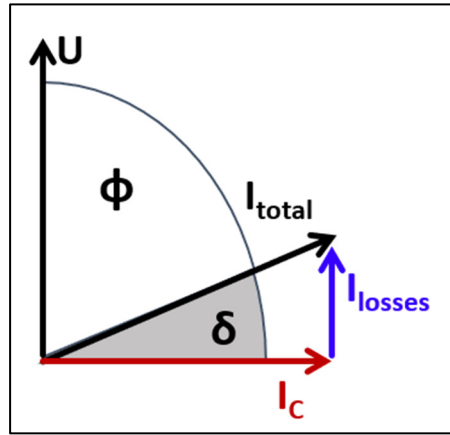


Figure 3.6 Phasor diagram representing the applied voltage U and the measured current with corresponding loss angles

In engineering, electrical insulation systems are usually characterized using the tangent delta ($\tan \delta$) and the dissipation factor (DF) such as

$$\tan \delta(\omega) = DF(\omega) = \frac{\frac{\sigma}{\omega \epsilon_0} + \epsilon_r''(\omega)}{\epsilon_r'(\omega)} \quad (3.20)$$

In the United States and Canada, test technicians and engineers usually use the power factor ($\cos \phi$) instead of the tangent delta or dissipation factor. The power factor is the cosine of the

angle between the applied voltage and current. For a value below 10%, the power factor is very similar to the tangent delta (IEEE, 2001).

Another way to express the dielectric behavior of a material is the concept of complex capacitance. This representation is often used by academia and researchers. From the previously shown current equation 3.19, we can see that:

$$I^*(\omega) = j\omega C^*(\omega)U^*(\omega) \quad (3.21)$$

The complex capacity is:

$$C^*(\omega) = C'(\omega) - jC''(\omega) = C_0[\epsilon_r'(\omega) - j(\epsilon_r''(\omega) + (\frac{\sigma}{\omega\epsilon_0}))] \quad (3.22)$$

The tangent delta can be link to the complex capacity using the following equation:

$$\tan \delta(\omega) = \frac{C''(\omega)}{C'(\omega)} \quad (3.23)$$

It was previously mentioned that, upon the application of a static electric field, the polarization mechanisms begin with a certain time lag. When the applied electric field is variable in time, such as it is the case with a sinusoidal voltage waveform, some polarization mechanisms will begin to occur below a given frequency, which would provide the required time lag for the molecules to follow the electric field. The regions of the frequency spectrum where neglectable losses are observed result in a constant real permittivity value. For example, figure 3.7 shows the frequency dependence of different polarization mechanisms.

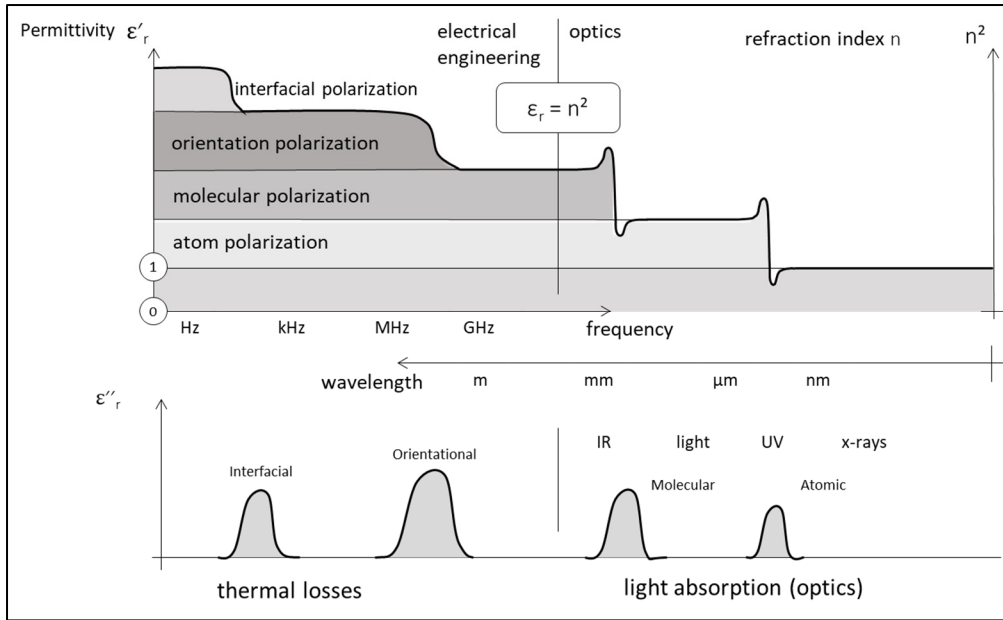


Figure 3.7 Sketch showing the frequency dependence of different polarization mechanism

Taken from OMICRON (2019, p. 7)

3.5 Application for stator winding insulation systems

The electric properties of a given material, namely the conductivity and the losses, whether these are expressed as the complex capacitance, tangent delta or power factor, are directly affected by the composition of the sample. Therefore, an insulation sample that has been contaminated with unwanted substances can exhibit higher conductivity and losses as it would be expected for a healthy sample.

The explanations and calculations provided above in this chapter were mainly applicable to individual insulation materials. Individual and homogeneous materials are significantly simpler than complete insulation systems. Among other factors, temperature, ambient condition, material geometry and composition are often known and/or controlled. This makes the determination of dielectric properties of homogenous materials, derived from electrical measurements, more accurate, in comparison with complex insulation systems used in electric apparatus. The electrical measurements of dielectric properties will be covered in the next chapter.

The construction of stator winding insulation systems was briefly explained in chapter 1, where its complexity was highlighted. Such system is made of a combination of different insulation materials (mica, glass fiber and epoxy resin), in addition to semiconductive layers and non-linear material (EPG). Each of these materials will have their own conductivity and complex permittivity. Their quantity, exact composition and geometry may also not be known at the time of the measurements, which makes it impossible to obtain electric properties. In such insulation system, the measured dielectric response may be very different from the one of either material alone (Gafvert, 2004). Therefore, the measured material properties have little diagnostic values for condition assessment.

Rather than looking at the derived material properties, comparative measurements are more useful in the context of condition assessment. Such example can include comparisons between measured dielectric responses on a same insulation system over time or comparisons between measured dielectric responses over similar equipment and/or insulation systems.

As an example, the main dielectric in stator winding insulation system is made of several layers of mica tape which has been impregnated with epoxy resin. If the impregnation and curing processes were performed successfully, it can be expected that only a minimal gas content will be present between the different tape layers. For this example, the gas content will be neglected. In this work, the electric properties of individual material was not measured. However, it is available in the literature from previous work. From (Stone, 2014), the power-frequency relative permittivity is about 4 and a typical loss tangent of 0.5% measured at 60 Hz for newly manufactured stator windings. However, measurements in (David, 2010) showed the dielectric properties of mica can vary from relative permittivity of about 7 or 8 and loss tangent of 3×10^{-4} at 100 Hz, to about 10 and 1×10^{-2} at 1 mHz. Also, in table 2 derived from (Kuchler, 2018), the relative permittivity can vary from 3.5 to 5.8. It can therefore be difficult to obtain reliable expected values. An operating machine will see its insulation system deteriorate over time. Mainly, the organic part of the insulation such as epoxy or polyester will change chemically over time. Thermal ageing can result in oxidation, which tends to increase the number of polar contaminants within the insulation. As seen previously in this chapter, the increase in polar groups would result in additional polarization losses within the insulation and

therefore, after some time, an increase in the initial typical loss-tangent value of 0.5% can be expected (Stone & al., 2014), (Hao & Gao, 2016) and (Goffeux, Krecke, Comte, Cottet & Fruth, 1998).

CHAPTER 4

ARTIFICIAL AGEING OF TEST OBJECTS

Three stator coils were used as test specimens to investigate the effects of insulation deterioration on the measured dielectric frequency response (DFR). The resin-based insulation system of stator windings is manufactured with a life expectancy of approximately 25 years (Sumereder, 2008). However, many machines have been reported to last past those 25-year mark. Therefore, manufacturers and operators often rely on accelerated ageing processes to verify that their design will last the life expectancy of the products. For rotating machines, there are two main dielectrics accelerated ageing tests that some specimens of newly manufactured components need to go through: the thermocycling (TC) test, according to IEEE 1310 (IEEE, 2012) and the voltage endurance test (VET), according to IEEE 1043 (IEEE, 1997) and IEEE 1553 (IEEE, 2003). These tests are briefly described in the following sections.

The three stator coils went through both the TC and VET, according to the mentioned IEEE standards. Since all the coils successfully passed those two ageing tests without any failure, a third stage was added to further deteriorate the coils. At different moments during the accelerated ageing tests, DFR, PD and conventional DF measurements were taken at different intervals to evaluate the deterioration of the insulation throughout the ageing process. The PD and DF results were used as a comparison to evaluate the effectiveness of the DFR measurements. The test setups of the different measurements are described in chapter 5. The current chapter provides a description of the test specimens and of the three different accelerated aging tests.

4.1 Stator coil specimens

The specimens were three (3) extra coils from a recently manufactured hydro generator. They are identified as coil 07, 19 and 20. They had a rated voltage of 13.8 kV and are of thermal class F. They had three turns per coil and the main insulation thickness was approximately 3.3 mm. A schematic showing the dimension (in inches) of the slot portion of the coils is available

in figure 4.1 while a picture of the stator coils, sitting inside a transport case, is available in figure 4.2.

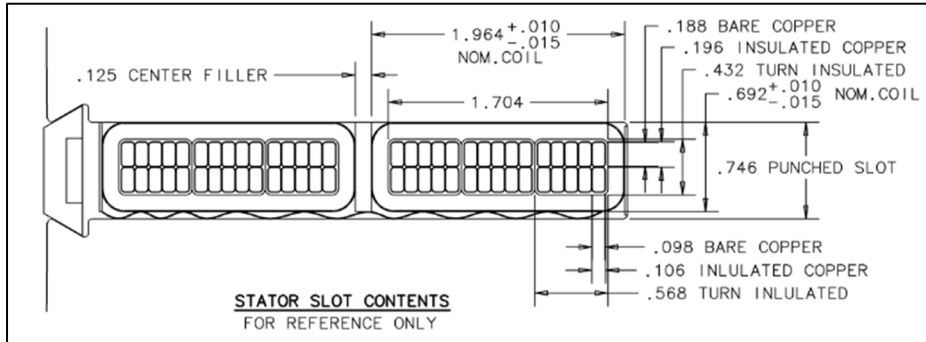


Figure 4.1 Schematic showing the cross-sectional dimensions of a stator coil



Figure 4.2 Picture of the three stator coils used as test specimens

4.2 Thermal cycling test

During normal operation, thermal cycling can occur when the load of a machine changes rapidly, causing the current and thus, the conductor temperature to change swiftly from a low temperature and to high temperature or, from the other way around from a high temperature to a low temperature. As the conductor temperature rises or decreases, the materials expand and

contract. The thermal coefficient of expansion of the insulation and of the conductor are different. Therefore, the thermal changes can gradually create cracks in the insulation, delamination between the insulation and the conductors or, simply delamination between different layers of the insulation. The process was briefly introduced in chapter 2.

Thermal cycling tests mimic the behavior described in the previous paragraph. It is usually performed to evaluate the ability of the coil to resist the thermal cycling failure process described earlier. In North America, the test is usually performed according to IEEE 1310. The document is intended to ensure that results from different organizations are comparable.

The thermal cycling is achieved by connecting some coil specimens together and by circulating an AC current through the formed closed circuit. Usually, four coils are used for the test, including one dummy coil. The definition of dummy coil is described later in this paragraph. The current must be sufficient to raise the temperature of the copper to the thermal class temperature of the insulation system under test. In the case of this experiment, the coils were of thermal class F and therefore, the temperature was raised to 155 degrees Celsius in approximately 42 minutes. When the upper temperature was reached, the current was decreased back to zero and fans were used to cool down the coils to a temperature of 40 degrees Celsius in approximately 42 minutes. This sequence is considered one cycle and is repeated 500 times (total ageing is 500 cycles). During this test, no high voltage is applied beside the small voltage drop that is built across the complete circuit formed by the coils. The temperature is monitored using what is called a dummy coil. Holes are drilled at different locations in the dummy coil and thermocouples are inserted to monitor the temperature. A connection schematic is available in figure 4.3 while a picture of the thermocycling test bench is available in figure 4.4.

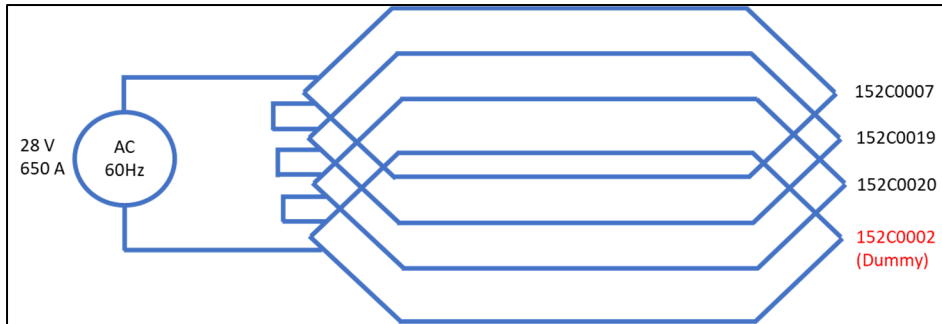


Figure 4.3 Connection diagram of the coils for the thermal cycling test



Figure 4.4 Picture of the test bench for the thermal cycling test

The ageing cycle was stopped after 100, 250 and 500 cycles to take DFR and PD measurements.

4.3 Voltage endurance test at elevated temperature

The voltage endurance test is usually performed to predict the behavior of the electrical insulation during long time voltage exposure. During a voltage endurance test, a voltage is applied to an insulation system that is higher than the expected operating voltage and the time to failure is measured, At the same time, the test specimens are also subjected to high temperature.

The test is standardized by IEEE 1043 and IEEE 1553. For 13.8 kV coils, they can be tested at either 30 kV_{RMS} or 35 kV_{RMS}, with a minimum acceptable time to failure of either 400h or 250h respectively (referred to schedule A or schedule B). The 35 kV_{RMS} test is considered more

stringent and therefore, a failure before the end of the test is more likely. For this reason, we decided to use schedule A as the ageing procedure for the voltage endurance test.

All three coils were connected in parallel and a voltage of 30 kV_{RMS} at 60 Hz was applied. The coils were also heated to reach a surface temperature of 90 degrees Celsius using heater plates installed on the grounded slot parts of the coils. A connection schematic is available in figure 4.5 while a picture of the voltage endurance test bench is available in figure 4.6.

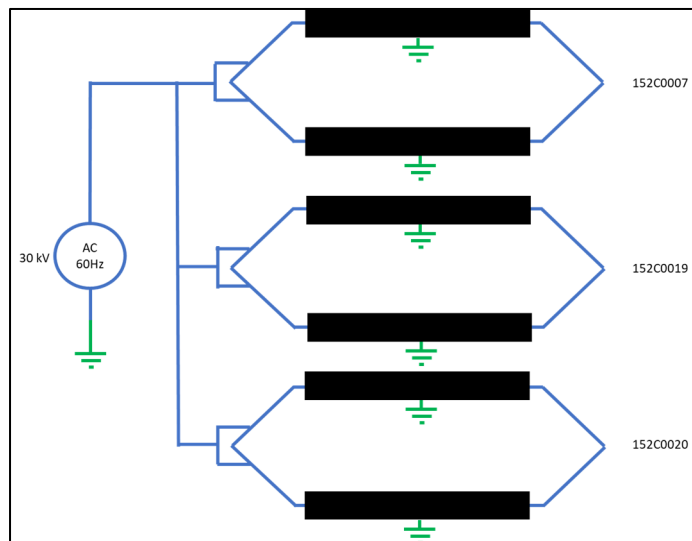


Figure 4.5 Connection diagram of the coils for the voltage endurance test



Figure 4.6 Picture of the test bench for the voltage endurance test

4.4 Voltage endurance test at room temperature

Since no failures occurred during VET and that limited deterioration were observed, it was decided to perform an additional voltage endurance test to deteriorate the insulation until failure. During this test the stator core was simulated by using aluminum metal L-shaped plate, clamped on the slot sections of the coil. The plates were 48 inches long, leaving approximately 2 inches of exposed OCP at both ends of each leg.

The additional voltage endurance tests were performed with the coils being at an ambient room temperature of 22 degrees Celsius. Due to the limitation of the voltage source, the coils were energized individually at a voltage of 30 kV_{RMS} and a frequency of 60 Hz. Even though the coils were not artificially heated during the test, the resistive losses of the EPG would heat the coils significantly. Figure 4.7 shows an infrared picture of one coil taken three hours after the application of the voltage. At equilibrium, the outer surface temperature of the straight part reached approximately 50 degrees Celsius. A picture of the voltage endurance test bench is available in figure 4.8.

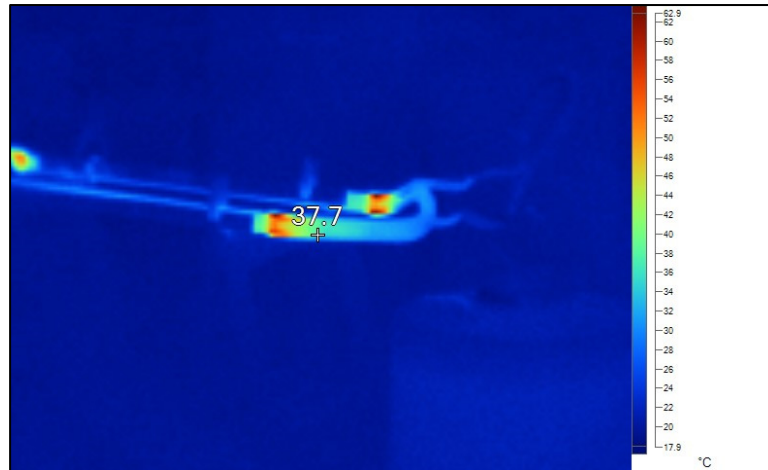


Figure 4.7 Picture of the coil three hours after the beginning of the stage 3 ageing process

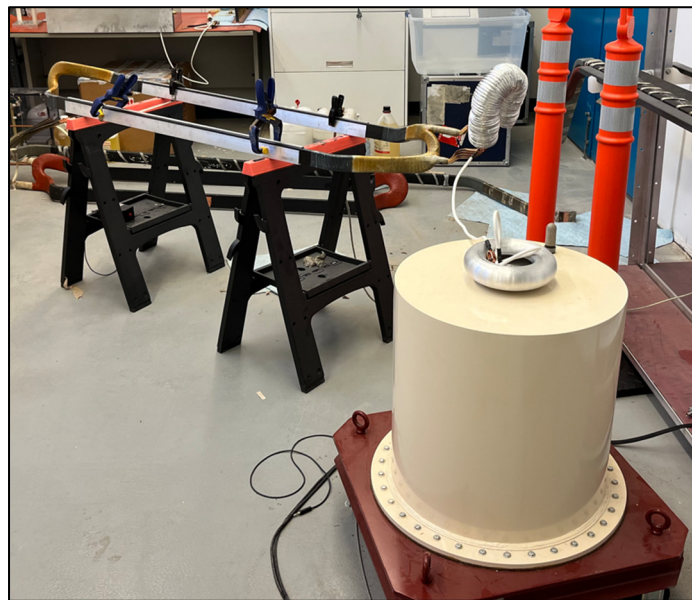


Figure 4.8 Picture of the test bench for the voltage endurance test at room temperature

The ageing cycle was stopped at different intervals to take DFR and PD measurements. Additionally, for coil 07, conventional DF measurements were also performed at different voltage levels, at 60 Hz.

For coil 19, a failure occurred after 823 hours of total VET time (423 hours after the beginning of the VET at room temperature). For coil 07, no failure occurred after 1613 hours of total VET time (1213 hours after the beginning of the VET at room temperature). Therefore, it was decided to increase the applied voltage from 30 kV_{RMS} to 35 kV_{RMS}. A failure occurred after 155 hours. For coil 20, the voltage was increased from 30 kV_{RMS} to 35 kV_{RMS} after 628 hours of total VET time (228 hours after the beginning of the kV_{RMS} at room temperature). A failure occurred after 91 hours.

CHAPTER 5

DESCRIPTION OF THE TEST PROCEDURES

Throughout the previously described artificial ageing stages, different dielectric tests were performed to evaluate the level of deterioration of each stator coils. For the TC and VET tests, from now on referred respectively as stage 1 and stage 2, all three coils were aged simultaneously, and the dielectric measurements were performed during the same visits for all three coils. Therefore, the time between measurements were identical among all test specimens. However, during the VET at room temperature, from now on referred as stage 3 when $30 \text{ kV}_{\text{RMS}}$ was applied and stage 4 when $35 \text{ kV}_{\text{RMS}}$ was applied, the test specimens were aged individually. The measurements were also taken at random intervals, depending on the availability of the test operator.

For all three coils, DFR measurements and PD measurements were performed every time the tests were stopped. However, for coil 07, conventional DF measurements were also performed when the VET at room temperature was stopped. Table 5.1 summarizes which dielectric measurements were performed for each interval.

Table 5.1 Summary of the performed dielectric measurements

	Coil 07			Coil 19			Coil 20		
	DFR	PD	DF	DFR	PD	DF	DFR	PD	DF
Reference	X	X		X	X		X	X	
TC 100 cycles	X	X		X	X		X	X	
TC 250 cycles	X	X		X	X		X	X	
TC 500 cycles	X	X		X	X		X	X	
VET 208h	X	X		X	X		X	X	
VET 400h	X	X		X	X		X	X	
VET 589h	X	X	X						
VET 615h				X	X				
VET 628h ¹							X	X	
VET 719h							Dielectric failure		
VET 769h	X	X	X	X	X				
VET 823h				Dielectric failure					
VET 922h	X	X	X						
VET 1230h	X	X	X						
VET 1613h ¹	X	X	X						
VET 1768h	Dielectric failure								

Note ¹ Applied voltage increased to 35 kV_{rms}.

The following section describes the test procedures for each dielectric measurement. The test results are presented in chapter 7.

5.1 Dielectric frequency response (DFR) measurements

The theoretical principles of DFR measurements were previously explained in chapter 3. The current chapter presents the practical aspect of the measurements including the test setup and the measurement parameters.

The DFR measurements were performed using the DIRANA (OMICRON, 2022) from OMICRON. The equipment uses a patented algorithm which combines the results from measurements performed in the time domain and in the frequency domain. The DFR results at frequencies of 100 mHz and higher are measured in the frequency domain while the DFR results at frequencies lower than 100 mHz are measured in the time domain. The reason of using such a combined algorithm is to decrease the overall required time to perform the measurements. Other commercially available instruments use different methods to reduce the overall time of a DFR measurement (MEGGER, 2020). As mentioned in chapter 3, the measurement in the frequency domain is performed by applying a sinusoidal voltage of a

specific frequency and measuring the phase shift between the circulating current and the applied voltage. However, when doing a measurement at lower frequency, a complete cycle can take lots of time. For example, a single cycle at 1 mHz takes 1000 seconds to complete. It is also worthwhile to consider that the equipment needs several samples to obtain the value measured at one specific frequency. In the other end, it is not possible to obtain the DFR of the higher frequencies using time-domain spectroscopy.

It was explained in chapter 3 that it is possible to convert the data obtained from time domain measurements in the frequency domain using Fourier transform. The DIRANA also converts the data from the time domain measurements into the frequency domain. To this end, the equipment uses the polarization current to convert the data in the frequency domain. However, the algorithm that is used is proprietary and can't be disclosed in this document. To verify the accuracy of the algorithm, measurements were performed on the same test objects in the time domain (PDC) and in the frequency domain (FDS). The results for one coil and one bar are shown in figure 5.1, where the x-axis shows the applied frequencies, and the y-axis shows the measured DF. These test objects were not the same as the ones used for the experiments described in this document. However, their insulation system was similar. The results are very similar.

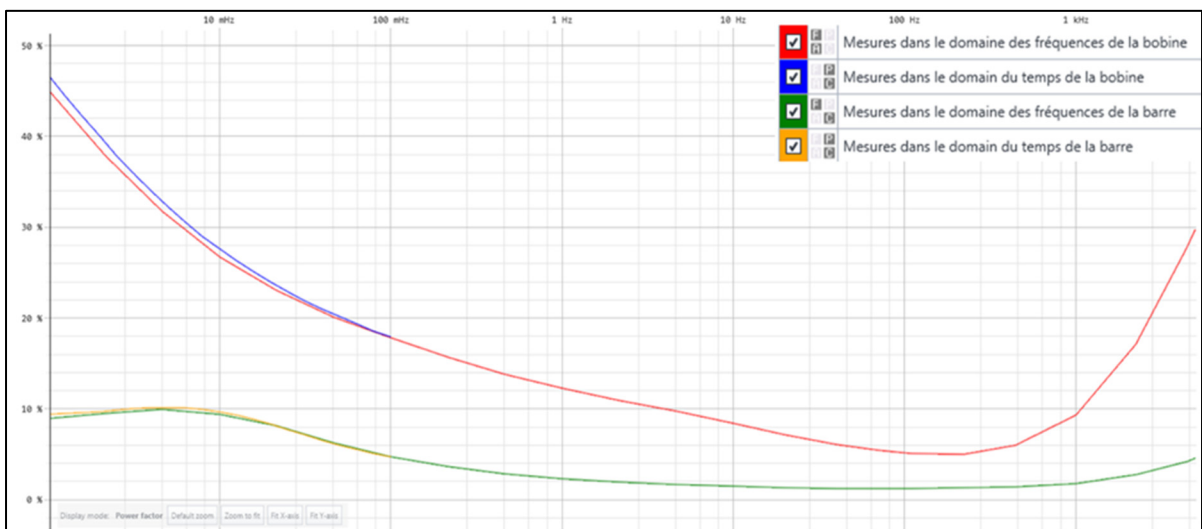


Figure 5.1 Comparison of the obtained DFR curves for the measurements using PDC and FDS, for two different test objects

The DIRANA has one voltage output and two current measuring inputs. Therefore, in theory, two different test objects can be measured at the same time. However, for our measurements, only one input was used and the coils were tested individually. The output of the DIRANA is not connected to ground (floating). For the measurements, the two straight parts of the coils were shorted together using a flexible aluminum braid and both ends of the coil's conductor bundle were shorted together. The voltage was applied to the conductor and the current was measured from the flexible braid using input 1 of the DIRANA. For each measurement, the DFR was measured between 5 kHz and 1 mHz, using a sinusoidal waveform of 200 V_{PEAK} for the frequency domain measurements and, using a voltage step of 200 V for the measurements in the time domain. A schematic of the test setup is available in figure 5.2.

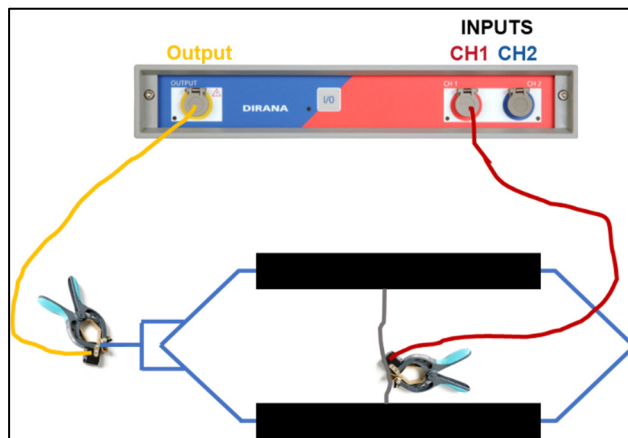


Figure 5.2 Image of the test setup used for DFR measurement

In theory, higher measured dissipation factors are usually the results of abnormal or deteriorated insulation systems.

5.2 Partial discharge (PD) measurements

The theory of PD was briefly introduced in section 2.2.6.

PD measurements were performed using the MPD800 (OMICRON, 2021) from OMICRON. All measurements were done in accordance with IEC60270 (IEC, 2015). For the measurements, a coupling capacitor of 1 nF was used to decouple the PD signals. A calibration was performed prior each measurement by applying a 100 pC charge using a calibrated calibrator CAL542 (OMICRON, 2022) from OMICRON.

Prior the measurements, each phase was conditioned by applying a sinusoidal voltage of 13.8 kV_{RMS} for a period of 120 seconds. The conditioning period is described in (IEEE, 2014); (IEC, 2006) and is used to obtain stable, repeatable, and comparable PD measurement results. PD magnitudes, which is expressed in picocoulombs (pC) or nanocoulombs (nC), usually tend to decrease upon energization. Following the conditioning period, the measurements were performed by applying a voltage from 0 V up to 13.8 kV_{RMS} in steps of 2 kV_{RMS} and with a duration of 30 seconds at a frequency of 60 Hz. The digital filters of the PD instrument were set with a center frequency of 250 kHz and a bandwidth of 300 kHz for all measurements. The charge values are weighted according to table 1 of IEC60270 (Q_{IEC}). This weighting process is automatically done by the MPD800. The reported values in this document are the average of the Q_{IEC} values over a period of 20 seconds. This averaging is automatically done by the MPD800. Figure 5.3 shows a schematic of the test setup, figure 5.4 shows a picture of the test setup and figure 5.5 shows the applied voltage profile for the PD measurements.

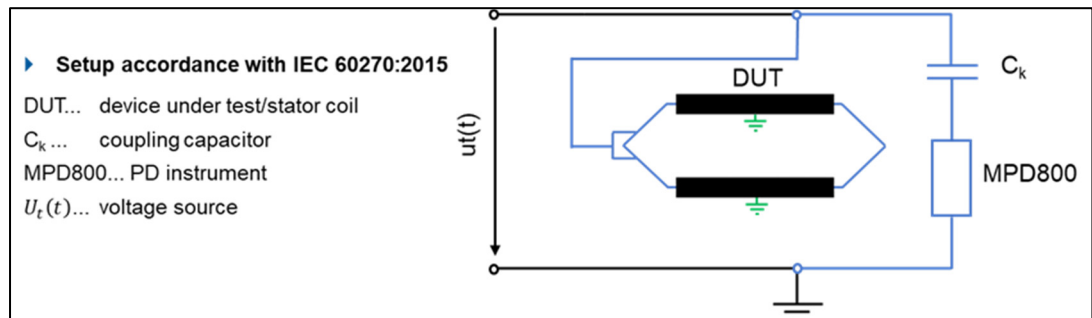


Figure 5.3 Schematic of the test setup used for PD measurements

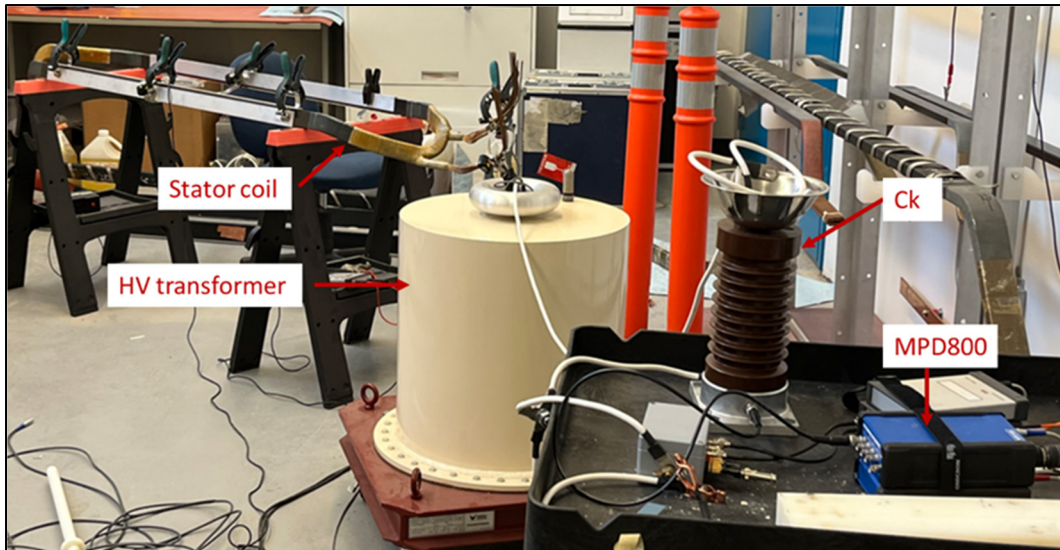


Figure 5.4 Picture of the test setup during PD measurements

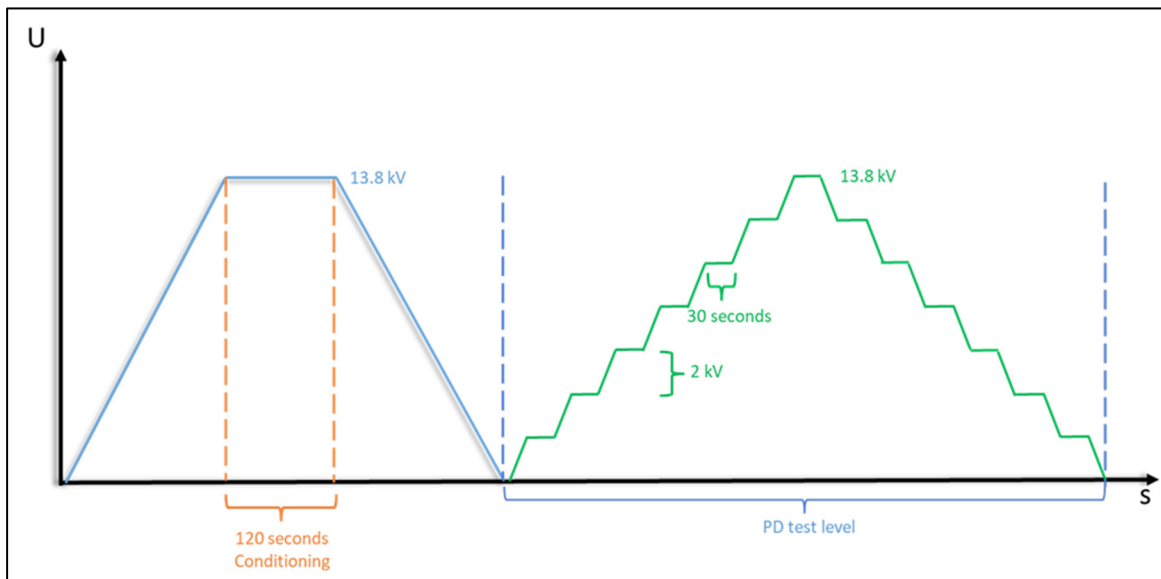


Figure 5.5 Applied voltage test sequence used for the PD measurements

In theory, higher measured PD magnitudes are usually the results of abnormal or deteriorated insulation systems. However, certain types of PD activities are more critical than others. Therefore, it is often useful to extract another parameter from the PD measurements: the phase-resolved partial discharge (PRPD) diagram. The PRPD diagram is a widely used representation which plots each PD events on the same diagram, where the x-axis is the phase angle of the

applied voltage waveform, and the y-axis is the charge magnitude of each detected PD events. A color code is used to highlight areas of the diagram where PD events occur more often. Specific diagrams are associated with specific anomalies for rotating machines. Figure 5.6 shows a simplified schematic describing how the PRPD diagram is built and figure 5.7 shows different examples of PRPD diagrams, which are associated to a specific type of defect. For more information regarding the PRPD diagrams, readers can look at references (IEEE, 2014); (IEC, 2006).

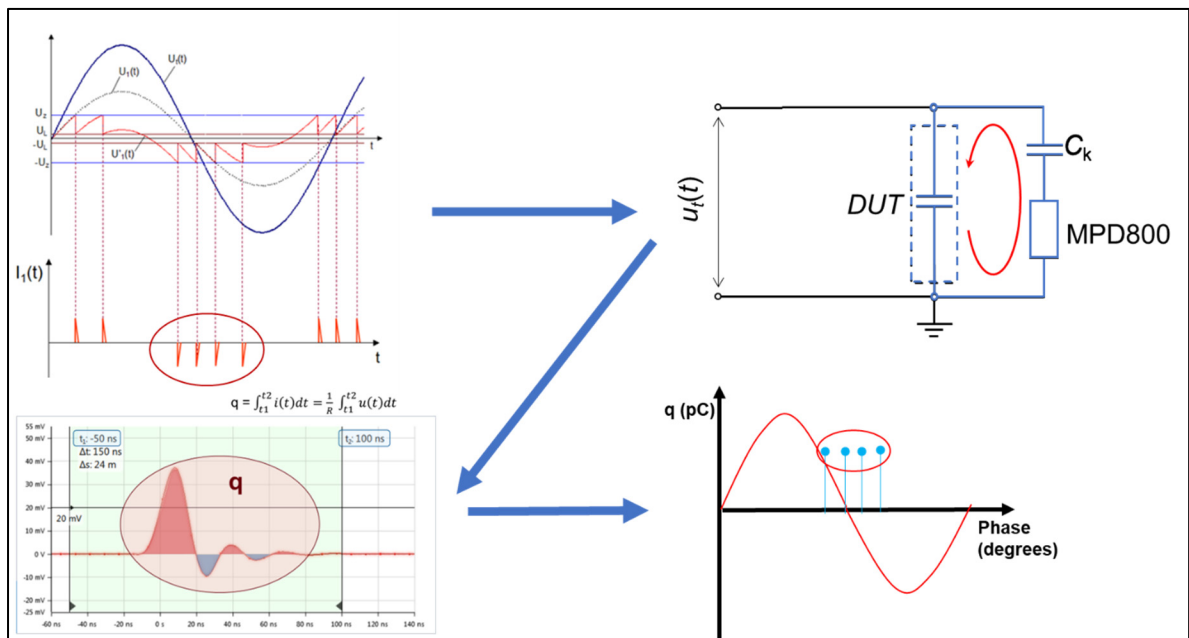


Figure 5.6 Simplified schematic describing how the PRPD diagram is built
Taken from OMICRON (2020, p. 17)

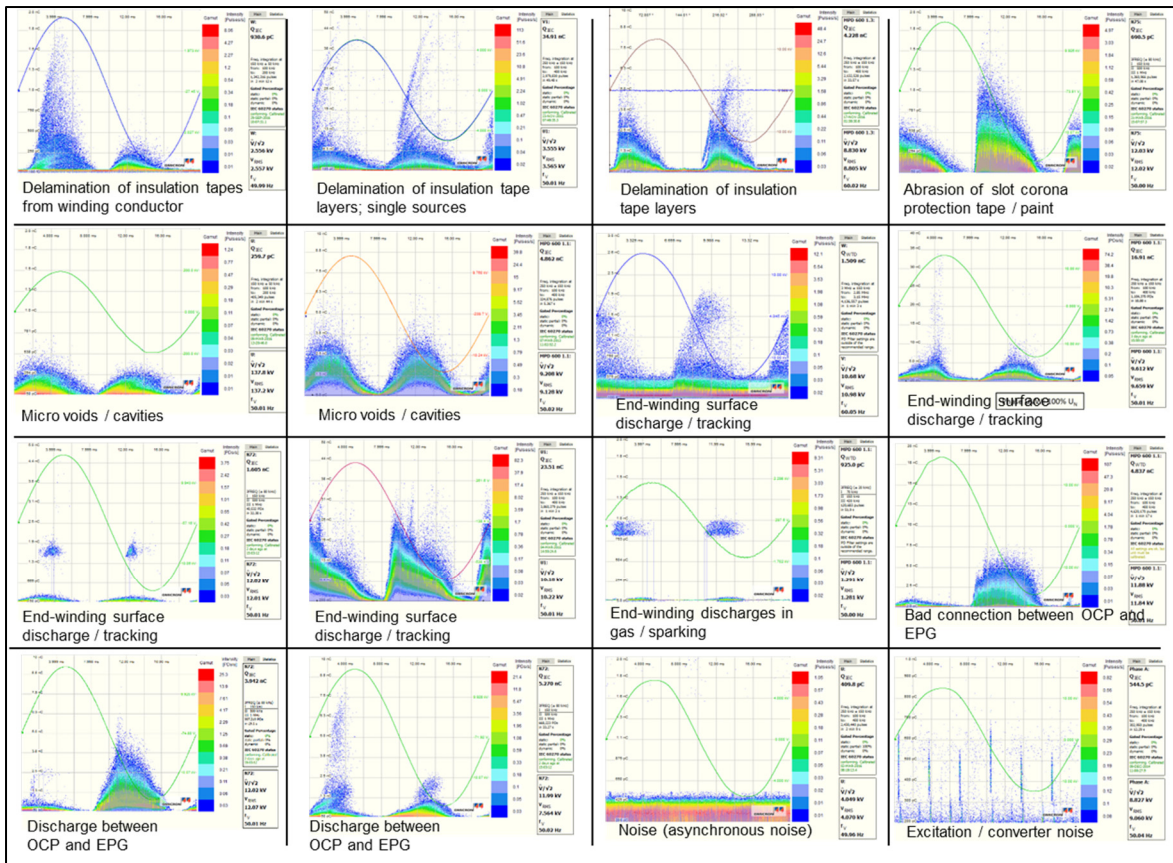


Figure 5.7 Examples of PRPD diagrams associated with typical defects on stator windings
Taken fromOMICRON (2023, p. 355)

5.3 Conventional dissipation factor (DF) measurements

An introduction to dissipation factor (DF) measurements was done in section 2.2.5. The dissipation factor was measured using the TANDO700 (OMICRON, 2017) fromOMICRON. The measuring principle is similar to the DFR measurements described earlier but, for one single frequency (60 Hz). The TANDO700 has two measuring units (impedances). One of those units is connected in series with a low-loss reference capacitor while the second unit is connected in series with the ground path of the test object. The two measured currents are then compared to extract the losses of the test object. The current flowing in the reference capacitor is assumed to with low loss and with a phase angle of 90 degrees in reference to the applied voltage. The reference capacitor used for the measurements at a value of 1 nF and measurements were performed at 0.4 kV_{RMS}, 2 kV_{RMS}, 4 kV_{RMS}, 6 kV_{RMS} and 8 kV_{RMS}.

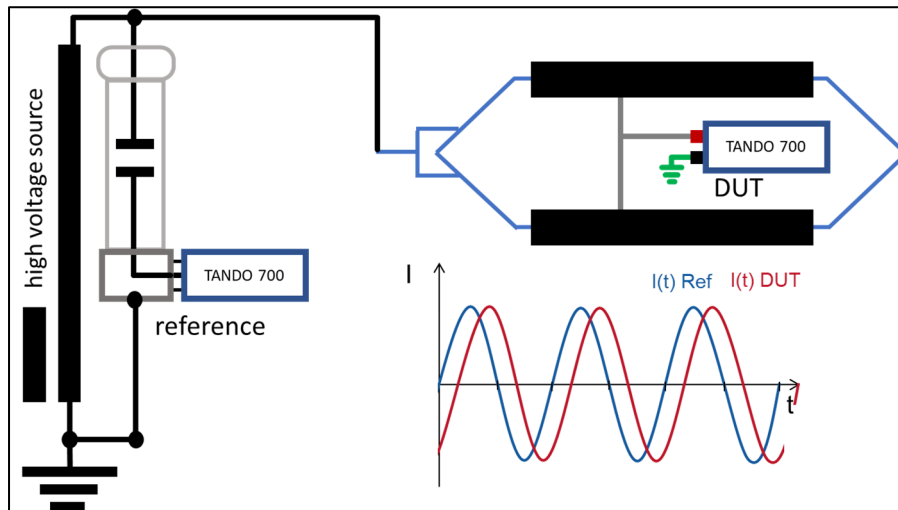


Figure 5.8 Schematic of the test setup used for the conventional DF measurements

In theory, higher measured dissipation factors are usually the results of abnormal or deteriorated insulation systems.

CHAPTER 6

INFLUENCE OF END POTENTIAL GRADING ON DIELECTRIC LOSS MEASUREMENTS

The end potential grading material was briefly introduced in section 1.1.5. However, because of its strong influence on dielectric loss measurements, a more detailed description is provided in this section.

In the slot sections of stator windings, the electric field is well defined and controlled by a system similar to two-plane-electrodes which consists of the conductor bundle and the OCP. As explained in section 1.1.4, the OCP is a semi-conductive layer that is applied on the surface of the last insulation layer, within the slot sections of stator coils and bars for machines with rated voltages of 4 kV_{RMS} and higher. This system creates a well controlled and fairly homogenous electric field distribution in the solid insulation, which typically varies between 2.7 kV/mm for the middle and 5.1 kV/mm for the corners of a 13.8 kV bar, without cavities (David, 2021). The resistivity of the OCP is typically around 0.3 to 10 kΩ per square (Stone, 2014)) and is very small in comparison with the impedance and resistance of the insulation. Therefore, it can be considered that the OCP is maintained to ground potential along its whole length by several contacts with the grounded magnetic core (see figure 1.12). In the endwinding area where no OCP is used, the surface of the insulation is near the same potential as the conductor, because of the high impedance coupling between the outer surface of the insulation and the nearest ground in this region. Without field control methods, the electric field would be concentrated at the end of the OCP where the winding transitions from inside to outside of the core. Depending on the rated voltage of the machine, this could potentially lead to PD activities at the end of the OCP if the breakdown voltage of the surrounding air is reached. Figure 1.14 showed the theoretical electric field distribution when an energized high-voltage conductor exits a grounded enclosure without the use of stress grading methods. On rotating machines, the EPG fulfilled the stress grading method and is applied as a tape or a paint on machines rated at 6 kV_{RMS} and above (Stone, 2014).

EPG coatings are made using grains of silicon carbide (SiC). Small particles of SiC are held in a resin-type based material which can be cured the same way as the main insulation material. This compound has usually just enough conductivity to carry the capacitive current from the main conductor through the insulation without a significant increase in the electric field along its surface (Taylor, 2006). The design of the EPG results in a non-linear V-I curve where, the current increases exponentially as the voltage is increased beyond a certain threshold. Therefore, when there is an increase of the electric field along the surface of the EPG, the resistance will decrease which will prevent the electric field to increase beyond a certain critical value. This value is related to the breakdown voltage of the air. The exact V-I curves depend on many factors such as the level of metallurgical purity and the dosage used in the mixture during manufacturing. The exact mixture used for stator windings is proprietary to most machine manufacturers and varies depending on the design needs (Conley & Frost, 2005). Figure 6.1 shows the V-I curves of three different mixtures of EPG used for stator windings.

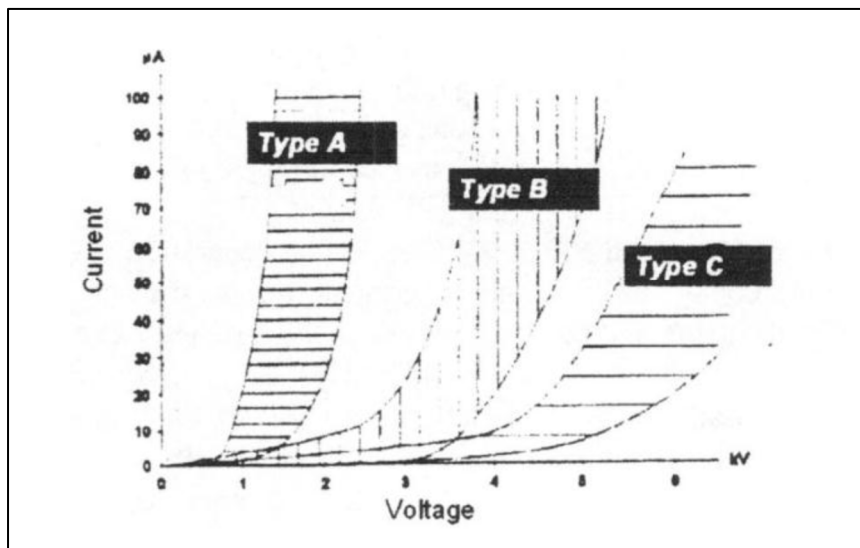


Figure 6.1 Typical V-I curves of EPG
Taken from Conley & Frost (2005, p. 92)

6.1 Frequency dependency

Even though the resistive grading of the EPG is theoretically not frequency dependent (in the frequency range of interest), the capacitive current flowing through the insulation underneath the EPG layer changes with frequency. The combination of the insulation and the EPG is

designed to have the desired V-I curve at power frequency, or at higher frequencies in case of inverter-fed machines (Stone & al., 2014). However, the behavior can be quite different for other frequencies. For example, at low electric field, the conductivity of the EPG is very small (see figure 7.6). When the applied frequency is 60 Hz, the 8.33 milliseconds (ms) half cycle doesn't provide enough time for the charges to migrate at the boundaries of the EPG and the insulation. However, if the frequency is decreased and the field maintained at the same low value, the AC half-cycle duration will increase and eventually, will provide enough time for the charge to migrate at the interface of the insulation underneath the EPG and the EPG itself. This situation is similar to the situation previously explained in figure 3.4. Once that charge migration is completed and that the insulation is fully charged. There is no more interfacial polarization involved (between the EPG and the insulation) and the remaining current circulating on the surface of the EPG will decrease significantly to the conduction level, which as mentioned previously, is very low. The total length of the EPG will therefore be at ground potential because of the connection with the OCP. This will result in the extension of the ground electrodes beyond the OCP. Therefore, the capacitance measured at low frequencies will include the capacitance value of the insulation underneath the EPG, in addition to the capacitance of the insulation within the slot, or underneath the OCP. Depending on the length of the EPG and the length of the slot section, this may have a significant effect on a capacitance measurement at low frequency if compared to a measurement at power frequency. For example, typically, the slot sections of turbo generator are significantly longer than the ones on hydro-generator. Therefore, the effect of the EPG will be less on a turbo generator, in comparison to a hydro generator, in which the slots are shorter. The effect will also be visible on DF measurements as well. As the measuring frequencies are decreased, there will be a specific time interval or applied frequency where the conditions for the previously mentioned interfacial polarization phenomenon are optimal. This will result in a loss peak in the measured DFR curves. This loss peak can be several orders of magnitude higher than what can be typically expected on a low loss material. If the frequency of the applied voltage is further decreased, then the losses will start decreasing as well after the previously mentioned loss peak (Taylor, 2006); (Taylor & Edin, 2010); (Cheng, Taylor, Werelius, Abideen & Hao, 2020).

Some experiments were done on coil specimen 02 after it had served as a dummy coil for the thermal cycling ageing test described in section 4.2. The capacitance and dielectric losses of the EPG and of the slot parts were measured independently using the DIRANA and guard electrodes. Conductive copper tapes were wrapped around the end of the EPG, near the connection to the OCP, and a small section of the OCP was removed to completely isolate each EPG, from the OCP in the slot sections of the coil. Using guarding techniques for dielectric loss measurements on individual coils and bars is a common practice for manufacturers. Some of those techniques are described in IEEE 286 (IEEE, 2001). Figure 6.2 shows a picture of one of the installed guard electrodes.

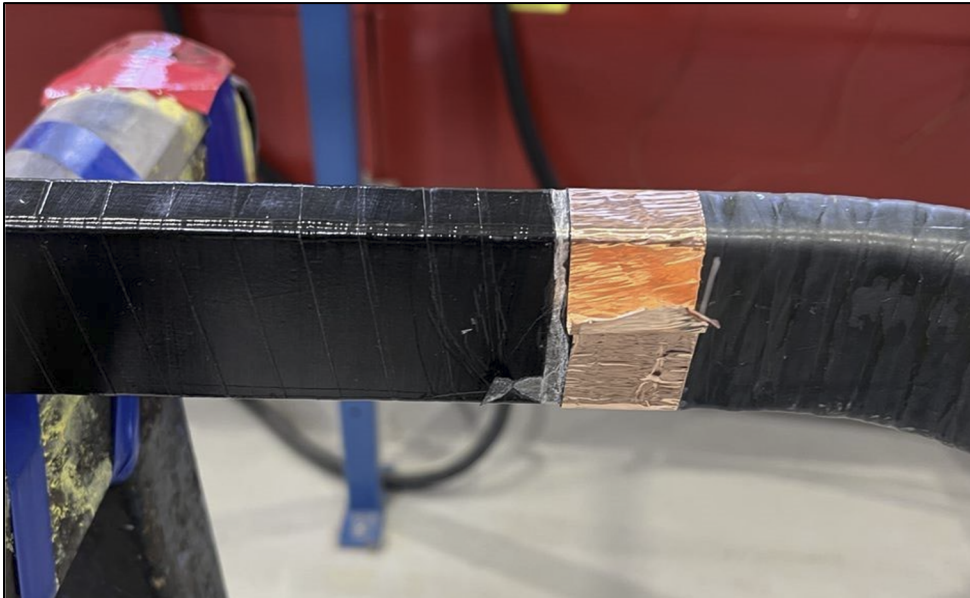


Figure 6.2 Picture of one of the guard electrodes installed on coil 02

The two slot sections of the coil were connected to the first input of the DIRANA while the four guard electrodes were connected to the second input. The applied test voltage was $141 V_{RMS}$. In addition, unguarded measurements were done prior the coil was used as a dummy coil for the thermal cycle test. Figure 6.3 and figure 6.4 show the real capacitance and complex capacitance measured simultaneously and independently as a function of frequency. The curve of an unguarded measurement is also displayed for comparison. The unguarded measurements and the guarded measurements were not taken at the same stage of ageing. However, the

unguarded measurement offers a realistic comparison. The relationship between dissipation factor and complex capacitance was previously explained in section 3.4.

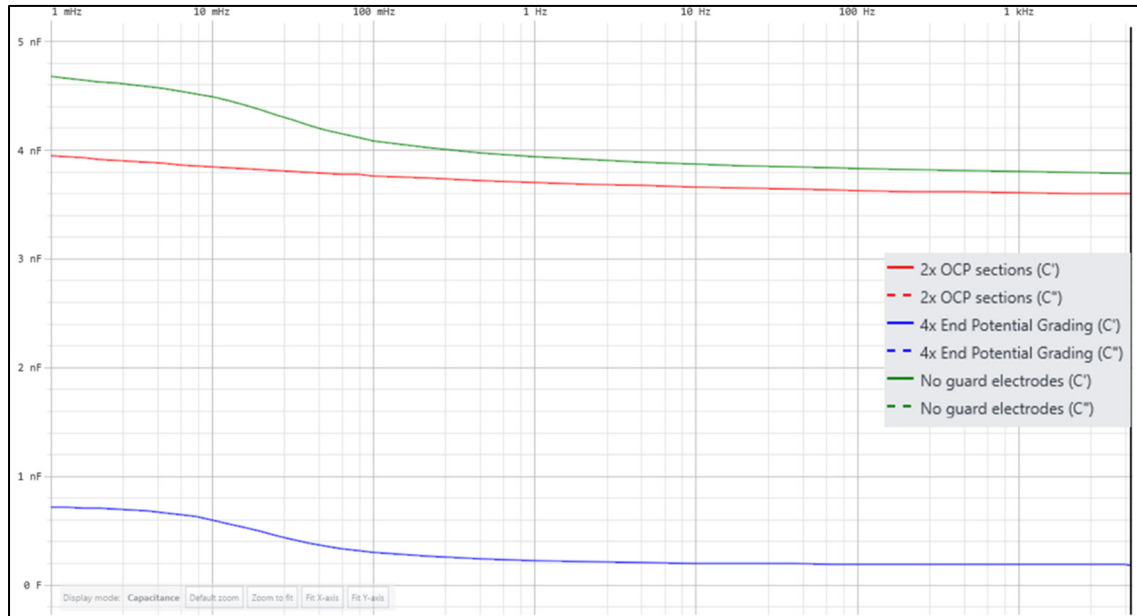


Figure 6.3 Guarded and unguarded measured real capacitance of the slot sections and the EPG sections using linear Y-scaling

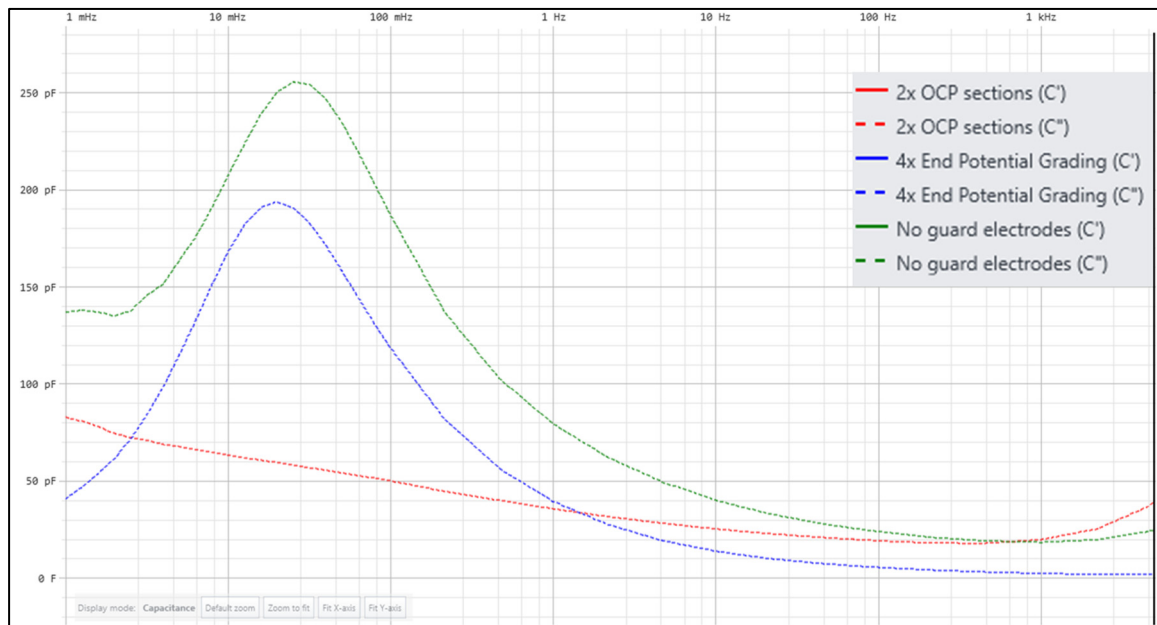


Figure 6.4 Guarded measured imaginary capacitance of the slot sections and the EPG sections using linear Y-scaling

The measured capacitance from the guarded EPG is constant at approximately 195 pF from 5 kHz down to approximately 10 Hz. At those frequencies, it is believed that the duration of each half cycle is not long enough at the applied voltage to initiate the interfacial polarization between the EPG and the insulation. At lower frequencies, the capacitance increases rapidly and reaches a maximum value of approximately 720 pF at 1 mHz. This significant increase in measured capacitance is caused by the polarization of the insulation underneath the EPG length. The total length of the OCP sections of the coil is 107 inches long. This total length has a measured capacitance of 3.640 nF at 60 Hz and of 3.950 nF at 1 mHz, which yields a capacitance of approximately 34 pF per inch (if measured at 60 Hz) or of 37 pF per inch (if measured at 1 mHz). This variation in capacitance in the OCP region is due to the insulation system's own frequency dependency of capacitance. Each EPG section of the coil is applied over 5 inches. Therefore, once the insulation underneath the EPG becomes completely polarized, a capacitance value between 680 pF and 740 pF for the insulation underneath the EPG can be expected. If enough time is allowed for the polarization of the insulation underneath the EPG, a loss peak is visible in the imaginary capacitance of the EPG. In the case of coil 02, those losses are even higher than the total measured losses of the OCP sections of the coil. When comparing the guarded measurements to the unguarded measurement, the loss peak seems to have moved towards lower frequencies for the guarded measurement in comparison to the unguarded measurement. This peak displacement is due to the thermal cycle process and is explained in section 7.1.1. As explained previously, the unguarded measurements were taken prior thermal cycle while the guarded measurements were performed after 500 cycles of thermal cycle.

6.2 Voltage dependency

The voltage dependency of the EPG sections of rotating machines is well known and has been studied extensively in the past by different authors (Taylor & Edin, 2010); (Cheng & al., 2020); (David & Lamarre, 2007); (Taylor, 2010). As the voltage is increased, less time is required for the polarization of the insulation underneath the EPG sections. This phenomenon was explained in chapter 3 and in section 6.1. In (Taylor, 2010), the author measured the complex capacitance of a simulated taped bar where he applied an EPG tape on the surface of a tube of

PTFE (polytetrafluoroethylene), which was mounted on the outer surface of a copper tube. The measurements were done over a wide range of frequencies and using different voltage levels. It was concluded that as the voltage level is increased, the loss peak previously mentioned in section 6.1 moves to higher frequencies. Different experiments were also done on real stator bars and coils by other authors (Cheng & al., 2020); (David & Lamarre, 2007) with similar results. The measured curves available in (Taylor, 2010) are shown in figure 6.5.

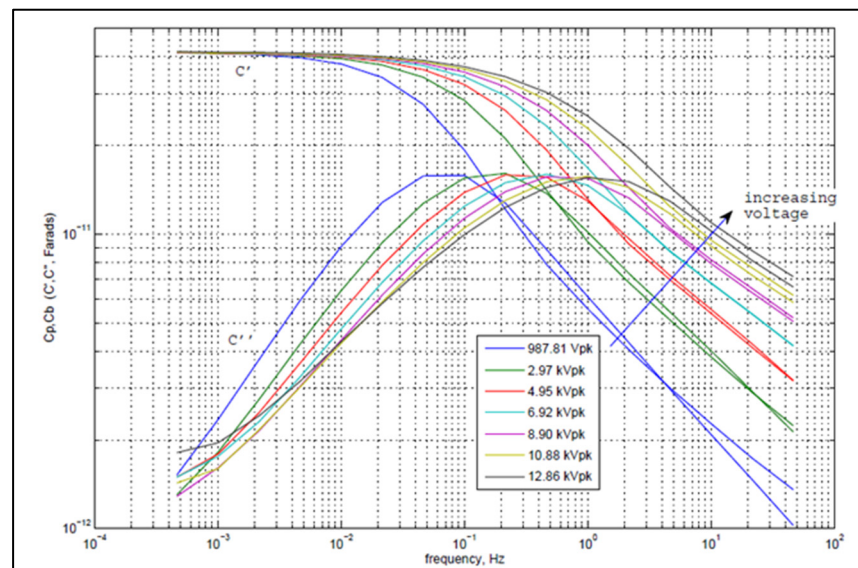


Figure 6.5 Complex capacitance measured from the PTFE tube
Taken from Taylor (2010, p. 186)

The voltage dependency of the EPG sections of rotating machines has significant influence on dielectric loss measurements. When the voltage is increased, the loss peak moves to higher frequencies and will interfere with the conventional dielectric loss measurements performed at power frequency (typically 60 Hz). The influence can be such that the losses of the EPG become predominant in the total measured losses, potentially hiding the losses generated by a defect that could occur in the slot sections. To mitigate this, manufacturers install guard electrodes when performing the measurements on individual components, such as bars and coils, as part of their quality assurance control procedures. However, it is not practical to install guard electrodes on complete stator windings. Therefore, it is expected that conventional

dielectric loss measurements, such as DF measurements, on complete stator windings will be highly influenced by the EPG, and to some extent, much more sensitive to changes in the resistivity of the EPG coating or in the insulation underneath it rather than in the main insulation in the slot sections.

Conventional DF measurements and capacitance measurements were performed on coil 07 after 589 hours of total VET time. As it will be seen in chapter 7, only limited deterioration was noticed on every test performed at that stage of the ageing process. The DF measurements were performed with the use of temporary installed guard electrodes. The guard electrodes were made in a similar way as what was shown in figure 6.2. However, no physical gaps were introduced between the OCP and the EPG sections, as to not damage the insulation of the coil for the rest of the experiments. Measurements were performed at different voltages to investigate the influence on the EPG on the total measured losses. Figure 6.6 shows a picture of two of the temporary guard electrodes. Figure 6.7 shows the measured losses for the EPG and for the slot sections while figure 6.8 shows the difference between the DF measurements performed with and without temporarily installed guard electrodes.



Figure 6.6 Picture of one of the guard electrodes installed on coil 07

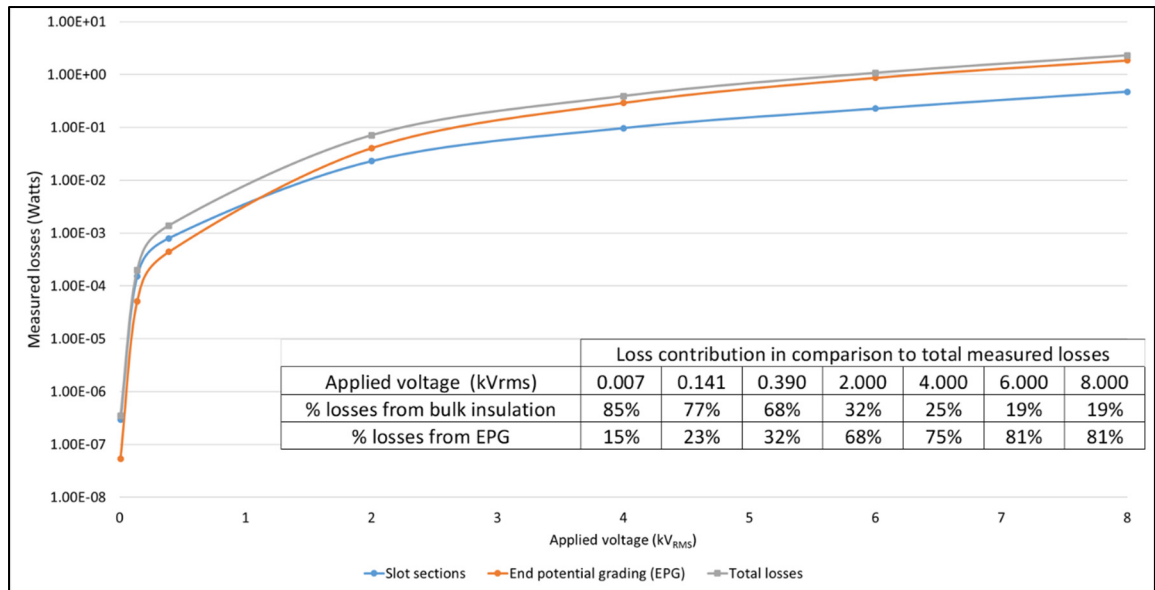


Figure 6.7 Guarded measured losses of the slot sections and the EPG sections

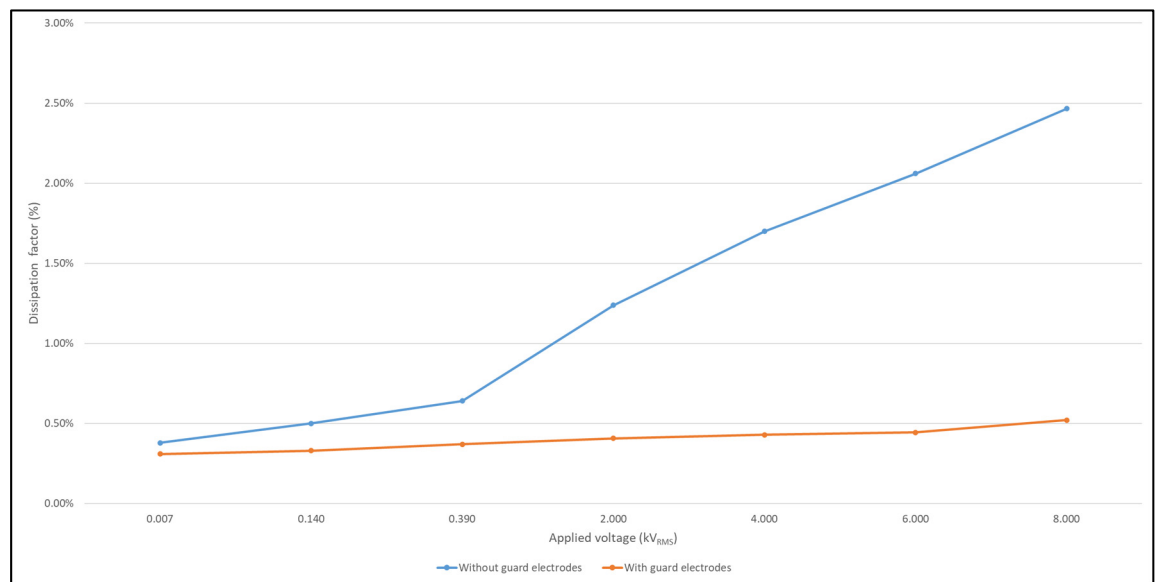


Figure 6.8 Comparison of DF measurements when performed with and without temporarily installed guard electrodes

When energized using a frequency of 60 Hz and at voltages below 1 kV_{RMS}, the loss contribution of the slot sections is the main contributor to the total measured losses. It can therefore be assumed that the measurement is more sensitive to defects within this section of

the coil. At voltages above 1 kV_{RMS}, the losses occurring from the interface between the EPG and the main insulation become predominant. At a voltage level of 8 kV_{RMS}, the losses from the slot sections are only approximately 19% of the total measured losses. The loss contributions are very similar for voltages of 6 kV_{RMS} and 8 kV_{RMS}. A probable explanation for this is an increase of losses in the slot section due to increased PD activities, at 8 kV_{RMS} in comparison to 6 kV_{RMS} (see figure 6.9). Nevertheless, they remain low in comparison to the total measured losses.

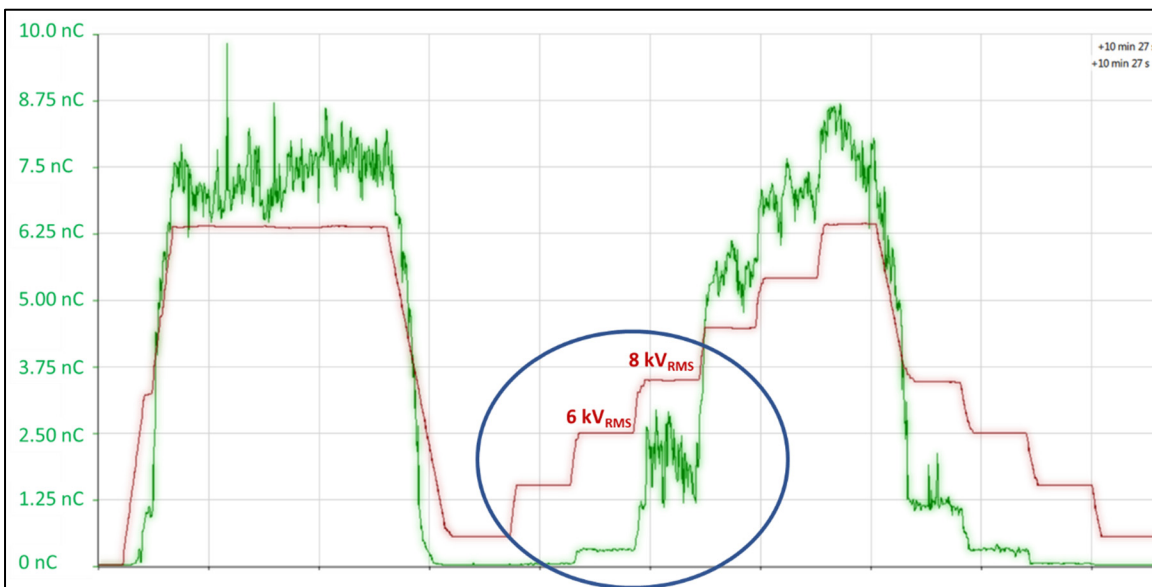


Figure 6.9 Measured apparent charge on coil 07 after 589 hours of VET showing the significant increase in PD activities from 6 kV_{RMS} to 8 kV_{RMS}

The sensitivity of the defects occurring in the slot sections decreases as the voltage is increased. This creates a challenge when conventional DF measurements are used as a diagnostic tool on complete stator windings as, it is impossible to know whether the measured losses are occurring because of the loss peak previously mentioned or because of deteriorated insulation within the slot sections of the machine. Therefore, being able to identify and assess the loss peak, or being attentive to the lower frequency range from the DFR curves could potentially offer the possibility to discriminate defects between the EPG and the slot sections.

Figure 6.8 shows that the temporary guarding technique used in our experiment was successful in mitigating the loss contributions from the interface between the EPG and the main

insulation. The loss contribution of the guarded measurement is only slightly voltage sensitive. The increase in measured losses for the guarded measurement is probably due to PD activities, which occur at higher voltages. In comparison, the unguarded measurement is significantly voltage sensitive.

6.3 Modeling of EPG

In the previous sections, the influences of the applied voltage frequency and magnitude were explained using the available literature and practical DFR measurements.

In this section, simulation models are used to show the influence of the EPG on the measured data. The simplest model that can be used to model the relaxation mechanisms of insulation systems is a conventional lumped-element model made of a resistance and a capacitor. This simple R-C lumped circuit is known as a pure Debye response and represents a specific polarization mechanism that could occur in a homogeneous material. The Debye model uses a simple R-C circuit to mathematically represent the equilibrium state of independent dipoles. Even though this model is less applicable to solid dielectrics because of the strong interaction between the dipoles, its use has been popular in the literature due to its simplicity (Taylor, 2006). We will use this model to show the dependence of the loss peak on the resistivity of the EPG coating. Figure 6.10 shows an electrical circuit equivalent to the Debye equations:

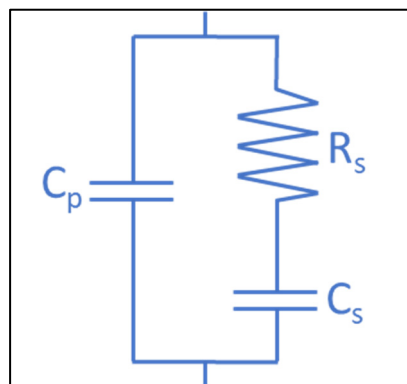


Figure 6.10 R-C circuit equivalent to Debye equations

Let's consider that R_s is the resistance of the EPG coating and C_p is the capacitance of the system measured at high frequency. The capacitor C_s is the capacitance of the insulation underneath the EPG section, measured at low frequencies, with the subtraction of C_p . For simplicity, let's consider that the conduction losses of the insulation are insignificant. The resistor R_s and the capacitor C_s represents a polarization mechanism, with a relaxation time of $\tau=RC$. We can use the following equation to describe this branch mathematically:

$$C' - jC'' = C_p + \frac{C_s}{1 + j\omega R_s C_s} \quad (6.1)$$

As mentioned in section 6.1, guarded measurements were performed on coil 02, where the complex capacitance of the slot sections and the EPG were measured independently. The capacitive component of the system at high frequency (1 kHz) was measured at approximately 190 pF. The resistivity of the EPG coating on coil 02 was not measured during our investigations. However, since the purpose of this simulation is to show the influence of the resistivity of the coating on the position of the relaxation peak, arbitrary values were selected. Those values are similar to the values measured on identical coils, available in figure 7.6. The resulting simulated real capacitance and imaginary capacitance are available in figure 6.11 and figure 6.12. The measured complex capacitance of the EPG section for coil 02 is as well plotted in the same figure for comparison.

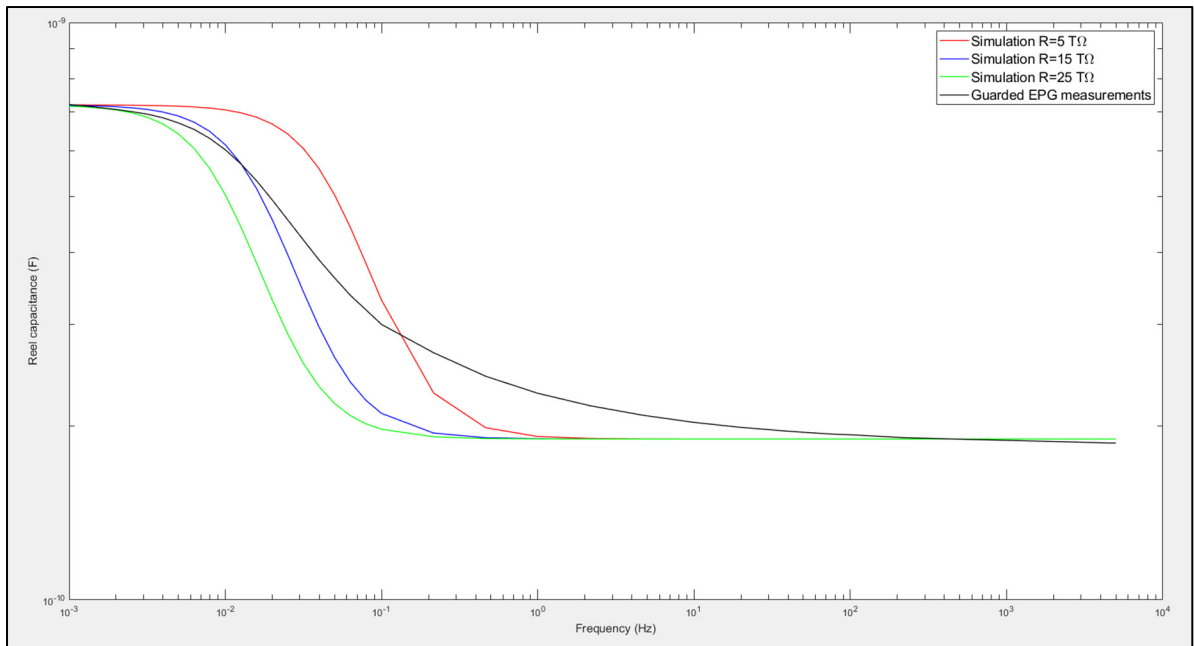


Figure 6.11 Simulated real capacitance of a simple R-C circuit using three different values of resistance of the EPG coating and, experimental results from a guarded measurement for coil 02

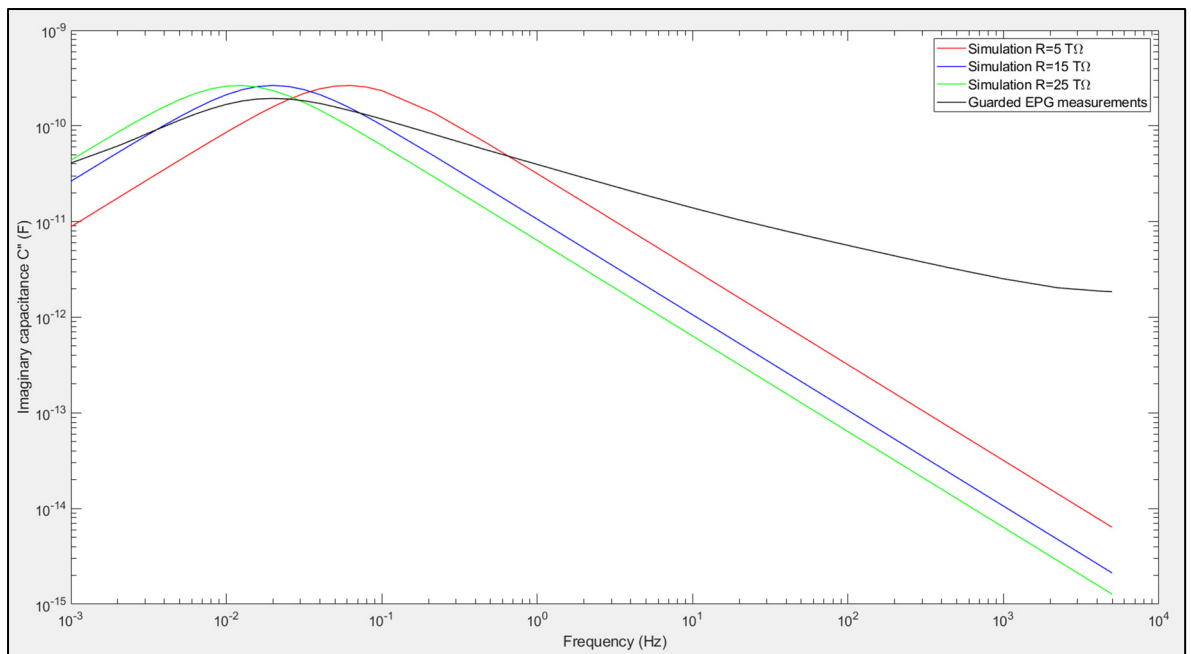


Figure 6.12 Simulated imaginary capacitance of a simple R-C circuit using three different values of resistance of the EPG coating and, experimental results from a guarded measurement for coil 02

Figure 6.12 shows that the loss peak is highly influenced by the resistivity values of the EPG coating. As the resistance is increased, the loss peak moves to lower frequencies. However, if the resistance is decreased, the loss peak moves to higher frequencies. The resistivity coating of the EPG is voltage dependent. As the voltage is increased, the resistivity will decrease and therefore, the loss peak is expected to move towards higher frequencies as the applied voltage is increased. This example correlates what was previously explained in sections 6.1 and 6.2.

Some variations on the Debye model are also used sometimes on polymers, with added empirical parameters which are used to adjust and fine-tuned the response for a better fit to the experimental data (Taylor, 2006). The equation 6.2 shows the added empirical parameters to equation 6.1. Figure 6.13 and figure 6.14 show the simulation using $R=25 \text{ T}\Omega$, $k_1=k_2=0.7$.

$$C' - jC'' = C_p + \frac{C_s}{(1 + (j\omega R_s C_s)^{k_1})^{k_2}} \quad (6.2)$$

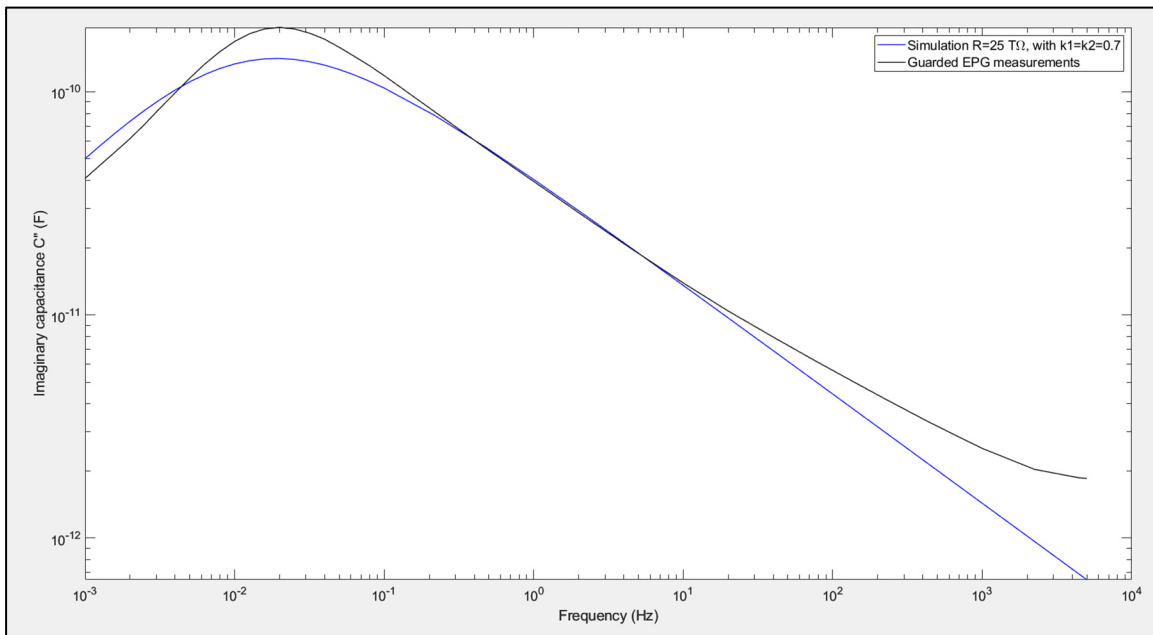


Figure 6.11 Simulated imaginary capacitance of a simple R-C with empirical parameters and, experimental results from a guarded measurement for coil 02

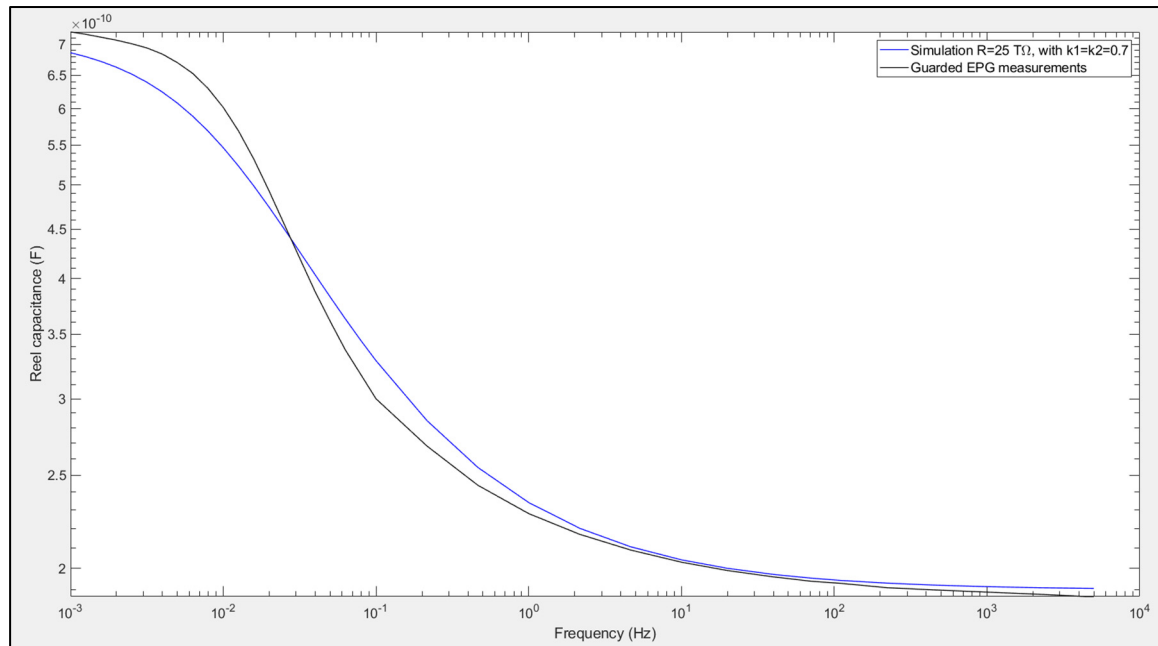


Figure 6.12 Simulated real capacitance of a simple R-C with empirical parameters and, experimental results from a guarded measurement for coil 02

The modeled curves do not fit the experimental data accurately. Even though the variation of the Debye model using empirical parameters does improve the situation, there are still discrepancies between the modeled curves and the experimental data. This is because the electric properties of EPG coatings cannot be modeled accurately as a lumped capacitance. Instead, a distributed-parameter system such as a transmission line should be used to model the EPG sections (Taylor, 2006). However, the simple Debye model provides enough information to visualize some of the phenomena related to the EPG previously explained earlier in this chapter.

As mentioned, the results of the simulation using the Debye model was only intended to simulate a single polarization mechanism. The fit would be much worse if the simulation using the Debye model was compared to the experimental results from an unguarded measurement. Alternatively for a better empirical mathematical fit of complete dielectric response including conduction and multiple polarization mechanisms, the Havriliak-Negami (HN) model (Pinto & al., 2023) can provide more accurate results for polymeric materials. According to that

model and with the addition of a term to consider the conductivity of the insulation system, the complex permittivity can be expressed as:

$$\varepsilon^*(\omega) = b(j\omega)^{n-1} + \sum_{k=1}^N \left[\frac{\Delta\varepsilon_k}{(1 + (j\omega\tau_k)^{\alpha_k})^{\beta_k}} + \varepsilon_{\infty k} \right] \quad (6.3)$$

Where ω is the angular frequency; n is an exponential factor between 0 and 1; τ_k is the relaxation time related to a relaxation process k ; $\Delta\varepsilon_k$ is the dielectric strength; $\varepsilon_{\infty k}$ is ε' at much higher frequencies than the one of the relaxation process; α_k is a width parameter, characteristic of the slope at the low frequency side of the relaxation peak; β_k is the asymmetry parameter, with $-\alpha_k\beta_k$ determining the slope at the high frequency side of the relaxation peak; N is the number of total relaxations observed in the studied range of frequencies and temperatures (Pinto & al., 2023). The term $b(j\omega)^{n-1}$ expresses the conductivity of the material.

Figure 6.15 shows the results from the simulation using the empirical HN model and the measured experimental data from an unguarded measurement, performed on coil 07 after 208 hours of VET.

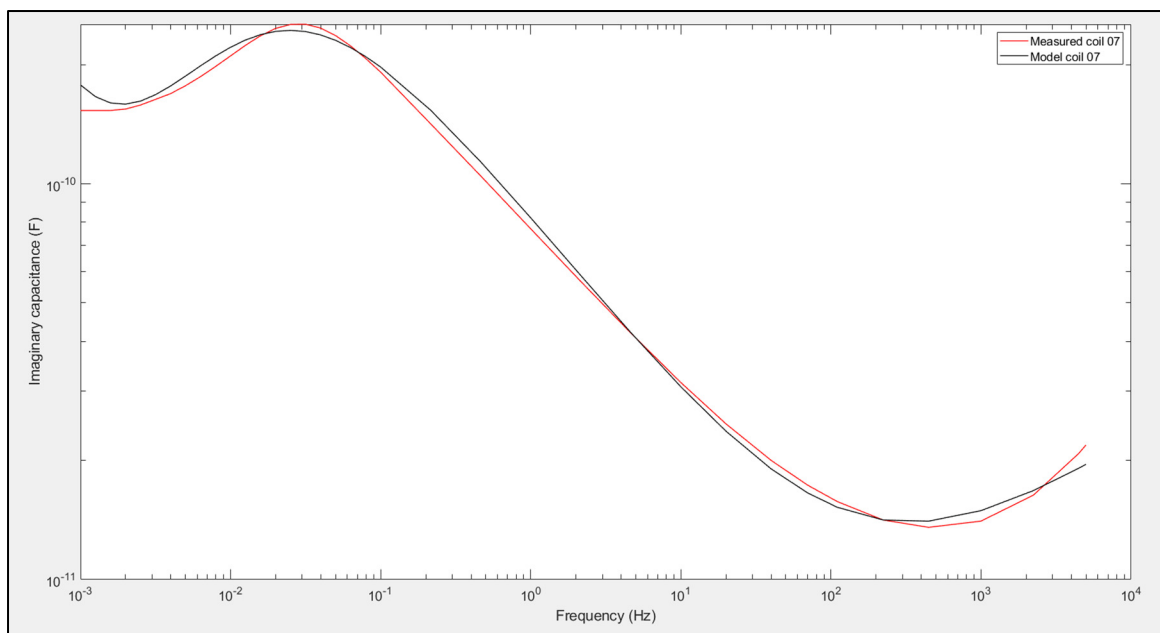


Figure 6.13 Simulated imaginary capacitance using the HN model compared with the measured imaginary capacitance of coil 07, after 208 hours of VET

CHAPTER 7

RESULTS OF MEASUREMENTS

This chapter summarizes the results from the experiments and from the measurements described in chapters 4 and 5. The results of each coil are presented and analyzed separately in three different sections. The coils are introduced in a numerical order, starting with the results of coil 07, then coil 19 and coil 20. Coil 07 was the one that was aged with the highest number of hours through VET and on which all dielectric tests were performed. Therefore, phenomena that were present in all three coils are explained in more detail using coil 07 as the main example. Analysis of the results that were not seen in every coil are presented and detailed in their respective sections.

7.1 Coil 07

Coil 07 failed after 1768 hours of total VET time. The last dielectric measurements prior failure were performed after 1613 hours of total VET time after which, the voltage was increased from 30 kV_{RMS} to 35 kV_{RMS}.

7.1.1 Results of DFR measurements

Figure 7.1 and figure 7.2 show all the measured DFR curves respectively represented using a linear and logarithmic scaling for the y-axis. Those measurements were taken at the intervals described in table 5.1.

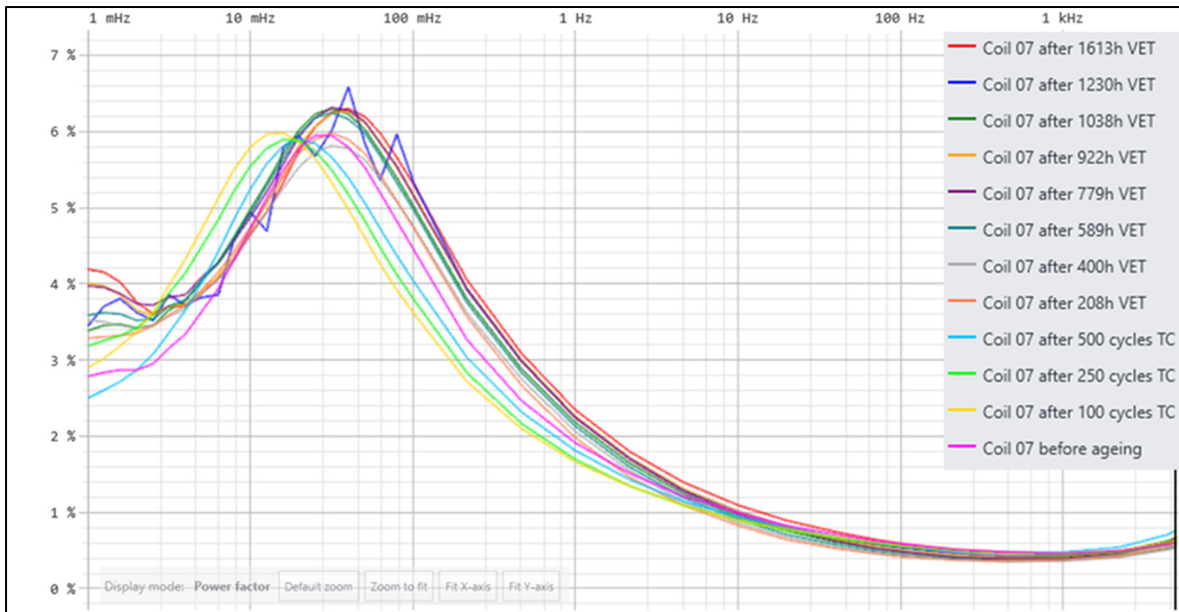


Figure 7.1 Power factor curves measured on coil 07 using a linear scaling for the y-axis

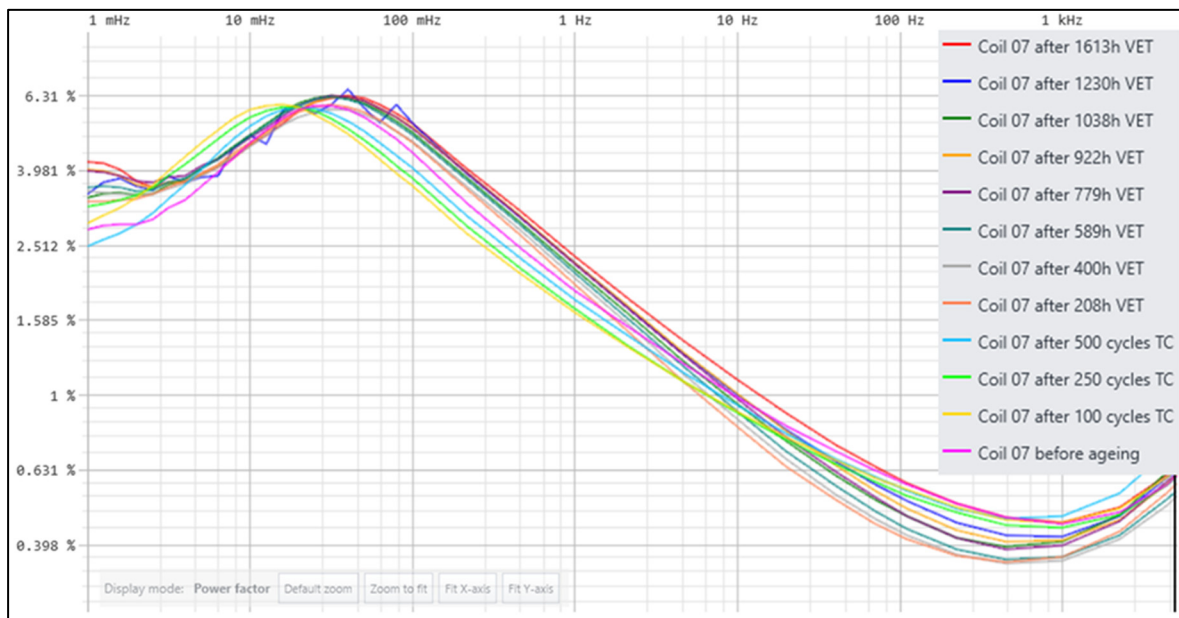


Figure 7.2 Power factor curves measured on coil 07 using a logarithmic scaling for the y-axis

The DFR curve measured after 1230 hours of VET (in dark blue in figure 7.1 and figure 7.2) was disturbed by interferences at frequencies below 100 mHz. However, it does not interfere significantly with the overall interpretation of the data.

Every measured DFR curves include a loss peak, in the frequency range between 10 mHz to 100 mHz. The presence of the loss peak was previously explained in chapter 6.

To improve the visualization of the curves presented in figure 7.1 and figure 7.2, the data is summarized in table 7.1 where the measured DF values at some of the measured frequencies are indicated as a function of the measurement interval.

Table 7.1 Summary of the measured DF values for coil 07 from figure 7.1 and figure 7.2

	1 mHz	10 mHz	100 mHz	1 Hz	10 Hz	60 Hz	100 Hz	1 kHz	5 kHz
Reference	2.78%	4.72%	4.46%	1.91%	0.99%	0.65%	0.59%	0.45%	0.60%
100 cycles	2.90%	5.79%	3.62%	1.66%	0.90%	0.62%	0.57%	0.46%	0.63%
250 cycles	3.19%	5.54%	3.80%	1.70%	0.89%	0.60%	0.55%	0.44%	0.60%
500 cycles	2.51%	5.24%	4.05%	1.81%	0.94%	0.62%	0.57%	0.47%	0.76%
208h VET	3.29%	4.74%	4.74%	1.98%	0.82%	0.47%	0.42%	0.37%	0.58%
400h VET	3.51%	4.63%	4.75%	2.06%	0.86%	0.49%	0.43%	0.36%	0.53%
589h VET	3.59%	4.93%	4.97%	2.12%	0.90%	0.51%	0.45%	0.37%	0.55%
779h VET	3.97%	4.88%	5.16%	2.25%	0.98%	0.56%	0.49%	0.40%	0.67%
922h VET	4.00%	4.70%	5.18%	2.26%	1.01%	0.58%	0.51%	0.41%	0.61%
1038h VET	3.38%	4.97%	5.03%	2.18%	0.95%	0.55%	0.48%	0.41%	0.65%
1230h VET	3.46%	4.95%	5.34%	2.25%	1.00%	0.60%	0.54%	0.42%	0.62%
1613h VET	4.19%	4.65%	5.31%	2.35%	1.10%	0.67%	0.60%	0.46%	0.67%

As the accelerated ageing process progressed in time, the measured DFR values tend to increase over the whole frequency range. This is expected as the deterioration of the insulation is likely to generate additional losses, as mentioned in chapters 2 and 3. An exception is an initial decrease in DF values after the coil was aged through thermal cycle. During that interval, the measured DF values slightly decreased for the measured frequencies of 10 Hz and above. For example, the value measured at 60 Hz decreased from 0.65% to 0.62%. The decrease in dielectric losses after thermal cycle ageing is a phenomenon which has been encountered by other authors (Farahani, Borsi & Gockenbach, 2006); (Calo, Catalano & del Valle, 2020);

(Soltani, David & Lamarre, 2010) during similar investigations. They attributed additional curing of the epoxy resin as the main reason. When a coil is first impregnated, the capacitance of the coil increased as, the resin replaces the air between the different tape layers. As the resin is cured, its viscosity increases and the resin solidifies, which decreases the relative permittivity of the insulation and thus the capacitance (Stone and al., 2014, p. 341). It does seem that this additional curing also occurred during the first 208 hours of VET. At that time, the measured DF values at 60 Hz decreased to 0.47%. As a reminder, the first 400 hours of VET were performed at a monitor temperature of 90 degrees Celsius at the surface of the OCP using heater plates. It is possible that it contributed to additional curing for the first 208 hours of VET. Following this initial decrease, the measured DF values increased as the ageing process progressed.

Additionally, the loss peak created by the interface of the EPG and the main insulation initially moves to the lower frequencies during thermal cycle ageing. This can be explained by an increase in the resistivity of the EPG coating or by an increase of capacitance of the insulation underneath the EPG section. As demonstrated in chapter 6, if the resistance of the coating increases, the polarization is delayed by the reduced current flowing on the surface of the EPG section, increasing the relaxation time. Similarly, if the capacitance increases but the resistivity of the EPG coating stays the same, the relaxation time is also increased as there are more molecules to be polarized. The latter explanation is less likely to occur as, an increase in capacitance would mean that the geometrical surface of the endwinding has changed or that a material with higher permittivity was introduced in the insulation underneath the EPG sections, such as water. Moisture ingress is unlikely as, the coils were in controlled temperature and humidity level environment for the duration of the tests. Figure 7.3 and figure 7.4 respectively show the measured imaginary capacitance and the real capacitance throughout the accelerated ageing processes. Figure 7.4 shows that the measured real capacitance slightly decreased as the thermal cycle ageing progressed, which aligns with the assumption of additional curing of the resin. Therefore, a decrease of conductivity of the EPG coating is more likely to have occurred. As explained in chapter 6, SiC tapes are made of SiC grains and resin. It is possible that, as for the main insulation, additional curing of the resin in the EPG tape occurred. In

(Conley & Frost, 2005), the author has measured a decrease in surface conductivity of a B-stage resin rich SiC tape after curing, compared to before curing.

During the subsequent stages of accelerated ageing process and following the initial decrease in losses, the DFR curves were seen increasing with time exposure to the VET. Figure 7.3 and figure 7.4 show some of the curves of the measured real capacitance and imaginary capacitance for stages 2 and 3 of the accelerated ageing processes.

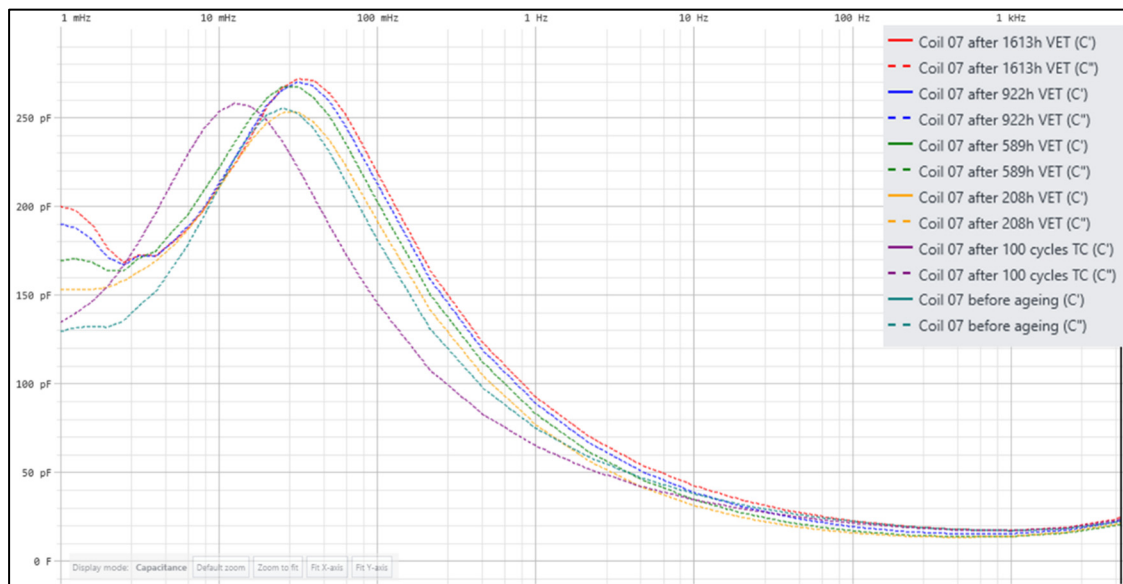


Figure 7.3 Summarized curves of the imaginary capacitance for coil 07

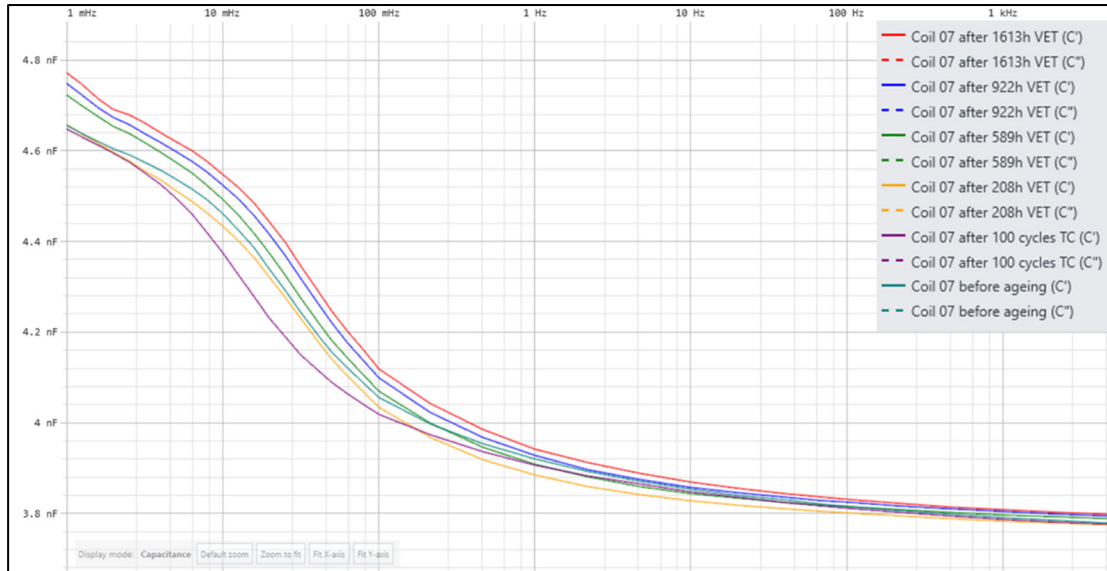


Figure 7.4 Summarized curves of the real capacitance for coil 07

After the initial decreased during thermal cycling, the loss peak is seen moving towards higher frequencies during VET. The magnitude of the loss peak also increases during ageing. Possible explanations are a decrease in the resistivity of the EPG coating or a decrease in the capacitance underneath the EPG layers. Figure 7.4 shows that the measured real capacitance increased over the whole frequency range with exposure to VET. Therefore, a decrease of resistivity of the EPG coating is more likely to have caused the displacement of the relaxation peak to higher frequencies. To confirm the decrease in resistivity of the EPG, measurements were performed on all three coils after failure and, on one unaged coil that was available from the same group of coils from the manufacturer. The measurements were performed by placing electrodes on one of the four EPG sections of each coil. The selection of which EPG section specifically was done randomly. One electrode was connected to the output of a DC high-voltage source while the other electrode was connected to an ammeter. Figure 7.5 shows a schematic of the test setup while figure 7.6 shows the results for all four measured EPG sections.

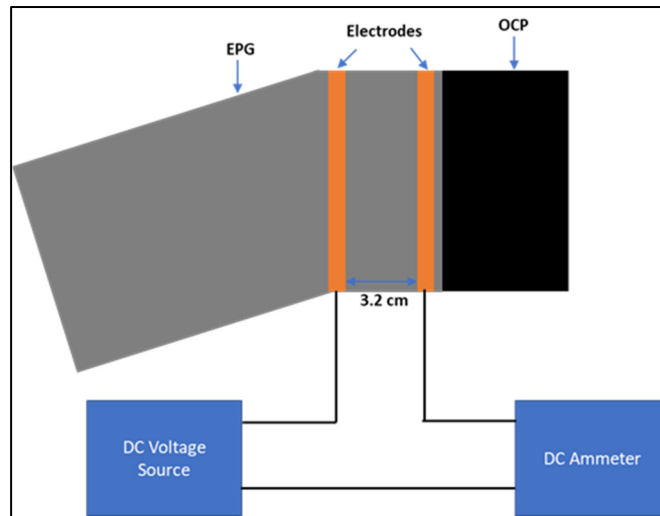


Figure 7.5 Schematic of the test setup for the measurements of the resistivity of the EPG coating

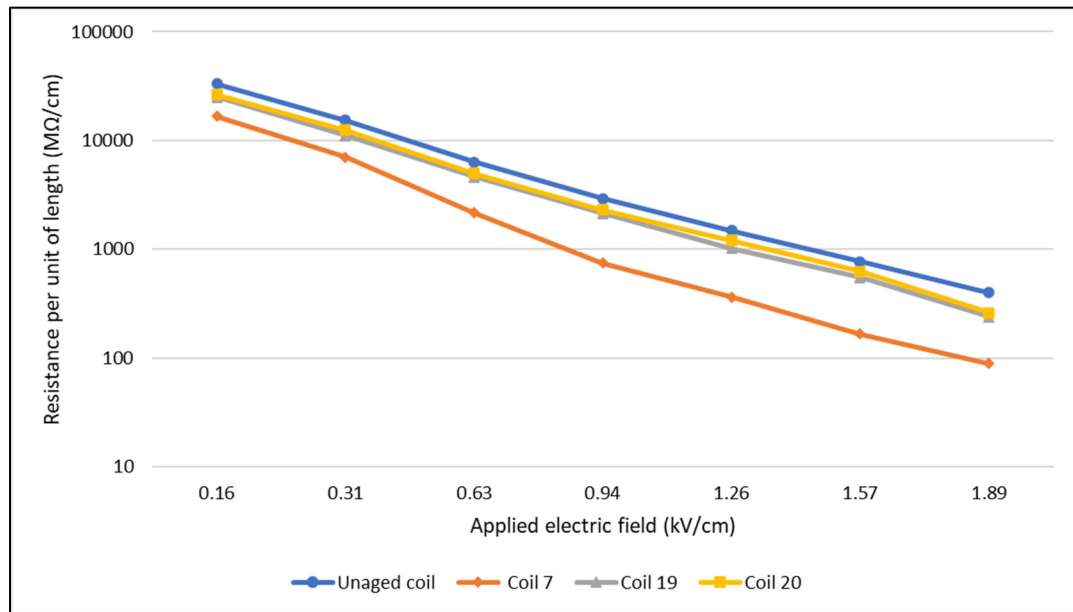


Figure 7.6 Measured resistance per unit of length of the EPG

The surface resistivity measured on the EPG sections of the coils that were exposed to VET are all lower in comparison to the EPG section of the unaged coil. The EPG section of coil 07 was the most affected with the lowest measured surface resistivity, followed respectively by the EPG of coil 19 and, then from coil 20. Therefore, it does seem that there is a relationship

between the time of exposure to VET of the EPG sections and the decrease of surface resistivity. Lower surface resistivity values were measured on the EPG sections from the coils that were subjected to the most hours of VET. Even though discrepancies can exist between the surface resistivity of the different EPG sections right after manufacturing and before ageing, the lower values in comparison to the unaged coil are in good correlation with the previously mentioned displacement of the relaxation peak towards higher frequencies. It can therefore be concluded that, as the coils aged through VET, the surface resistivity of the EPG sections decreased.

In (Conley & Frost, 2005), the effect of voltage endurance on B-stage resin rich SiC based tape was also investigated. It was shown that the surface resistivity of the voltage grading tape tends to decrease with time exposure to voltage endurance. This was also confirmed in (David, 2007). The decrease in resistivity of the grading tape will result in faster polarization of the insulation underneath the EPG and the displacement of the loss peak to higher frequencies (David, 2007). The decrease in resistivity of the coating can result in a decreased performance of the EPG, which can be detrimental to the stator winding.

As mentioned before, the DF values were seen increasing throughout stages 2 and 3 of the ageing process. The increase in DF values was more significant when measured at 1 mHz, in comparison to when measured at 60 Hz. A possible explanation is the frequency dependency of the capacitive current circulating in the insulation. When the capacitance is decreased, the capacitive current is proportionally reduced. However, if the losses remain constant, the DF will increase as the frequency is decreased. This can only partly explain the more significant increase in DF values seen at 1 mHz compared to 60 Hz. In figure 7.3, the increase in measured imaginary capacitance is higher when measured at 1 mHz compared to 60 Hz. This indicates higher losses, independently of the measured capacitive current. Another explanation can potentially be the contribution from conduction current from the EPG sections. It was previously mentioned that the resistivity of the EPG coatings is believed to decrease as the coil is exposed to VET. Therefore, this can result in higher conduction current as the coil aged and therefore, higher losses. However, it can be seen in figure 6.4 that the contribution of the losses

for low voltage at 1 mHz are mainly from the slot sections and not from the EPG sections in case of unaged coil. This can also be seen for the losses measured at 60 Hz in figure 6.7 as well, when the applied voltage is low. The increase in losses at 1 mHz was also noticeable during stage 1 of the accelerating process (thermal cycle). During that time, as it was previously mentioned, the resistivity of the EPG coating is believed to have increased, which would have resulted in lower measured losses. At this time, it is unknown if the increase of the losses at 1 mHz can be attributed to the EPG or to the slot section. It was previously explained in section 6.1 that the measurements at low frequency include the losses from the interfacial polarization between the EPG and the insulation. It is also possible that additional losses from other interfacial polarization mechanisms are also measured such as between the OCP and the insulation and, between the organic and inorganic material. In chapter 5, it was shown that the EPG sections were at much higher temperature than the rest of the coil during stage 3 of the accelerated ageing process. Nevertheless, the experimental data does show that the values measured at 1 mHz are more sensitive to ageing than the values measured at power frequencies.

7.1.2 Results of PD measurements

Figure 7.7 shows the trend of the measured apparent charge as Q_{IEC} over the whole ageing process. The values displayed in the graph is the average of the Q_{IEC} values obtained over a period of 20 seconds, at a voltage level of 8 kV_{RMS}. Table 7.2 shows the evolution of the PRPD diagrams built over a period of 20 seconds, at a voltage level of 8 kV_{RMS}.

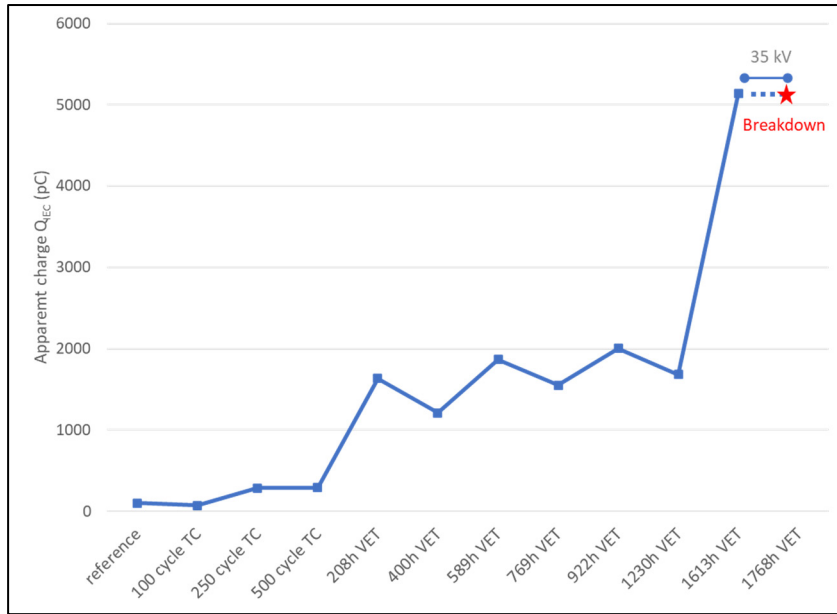


Figure 7.7 Trend of the measured apparent charge for coil 07

Table 7.2 Measured PRPD patterns at different stages of the ageing process of coil 07

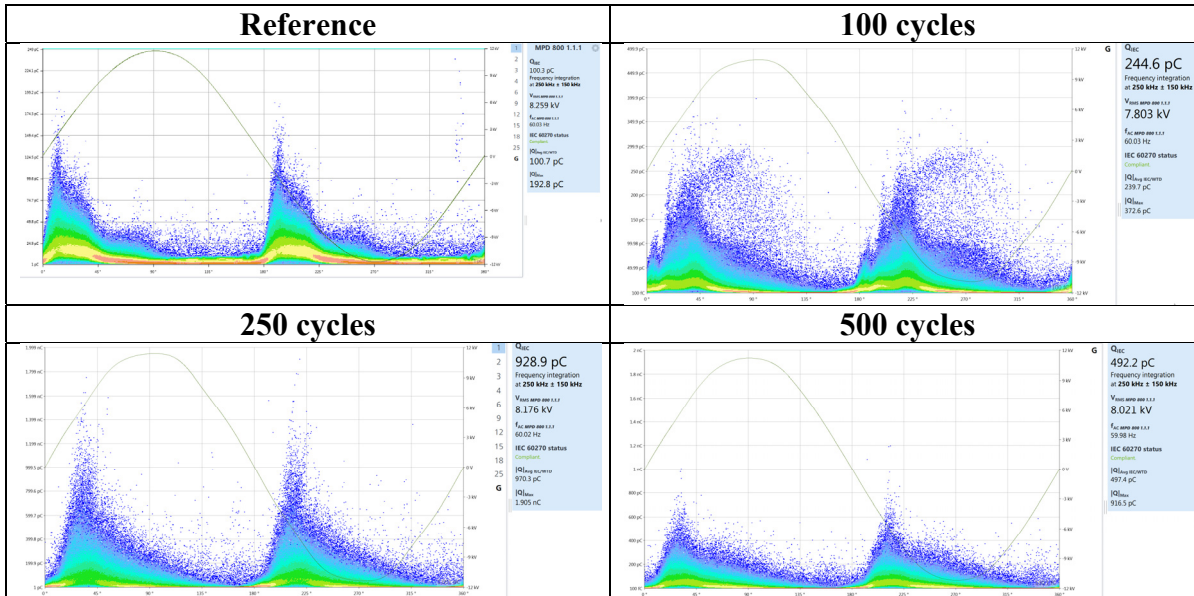
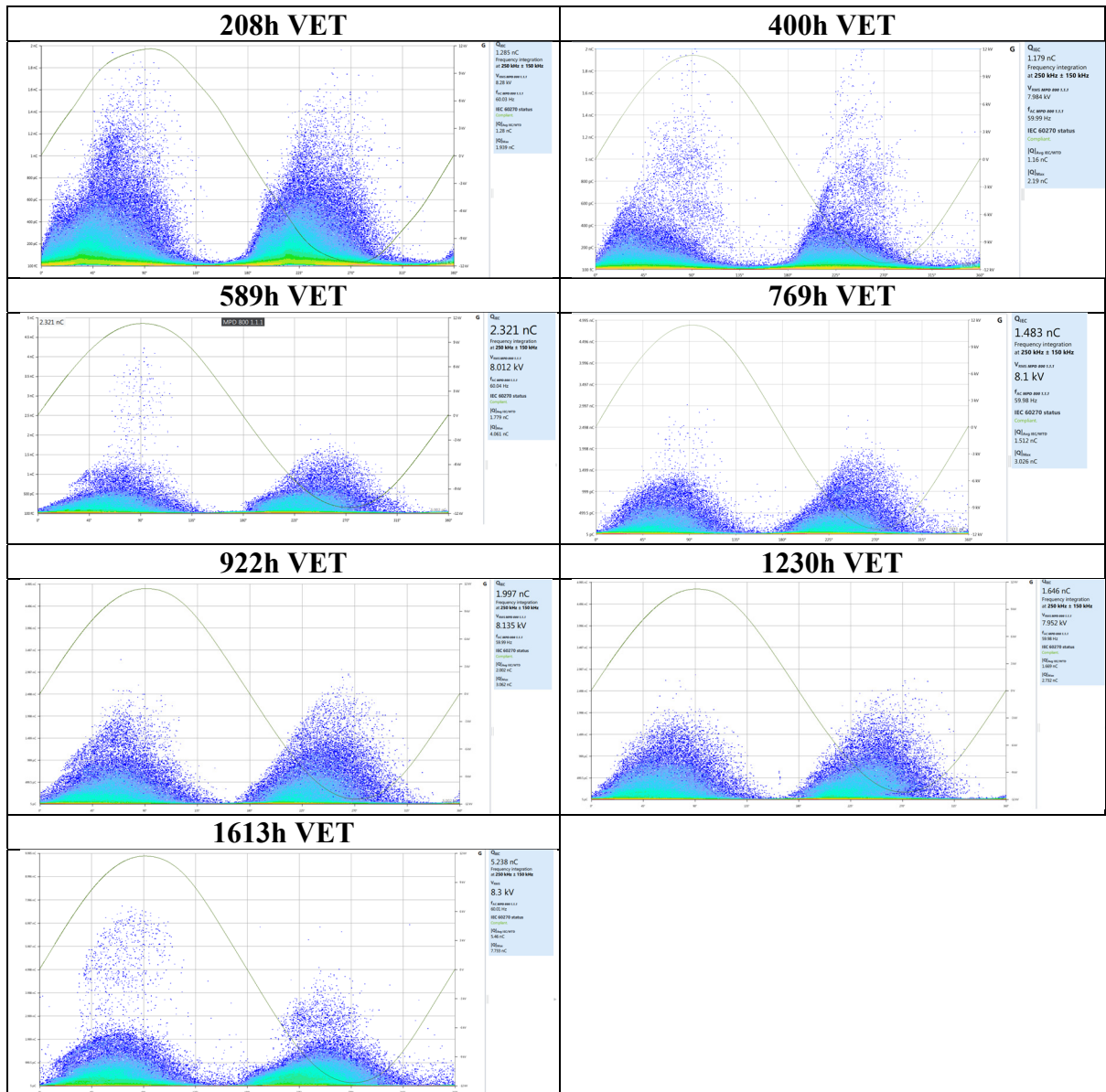


Table 7.3 Measured PRPD patterns at different stages of the ageing process of coil 07 (cont'd)



The PD magnitude Q_{IEC} increased significantly at two occasions during the ageing process: after the first interval of VET and during the last measurements prior failure. The reference PD magnitude was approximately 100 pC before the ageing process began while it reached more than 5,200 pC during the measurement prior failure. Even though there are no globally accepted PD limits for stator coils and bars, it can be assumed that significant deterioration took place during the whole ageing process. When comparing the measured PRPD diagrams

with the ones in figure 5.7, it seems that discharges due to cavities and delamination between tape layers were the main contributors of the measured PRPD patterns on coil 07. During the last measurement, discharges of higher magnitude and low repetition rates were captured predominantly during the first half cycle of the AC sine wave. While symmetrical PRPD patterns indicate PD activities within the insulation, a higher PD magnitude measured during the positive half cycle of the sine wave indicates PD activities occurring in contact with an energized electrode, such as the main conductor bundle. This can occur when cavities are present between the conductors and the first insulation layer. This type of defect is usually considered important as, the electric field is usually stronger closer to the main conductor bundle and therefore, discharges of higher magnitude are likely to occur.

7.1.3 Results of DF measurements

Figure 7.8 shows the trend of the measured DF at 60 Hz.

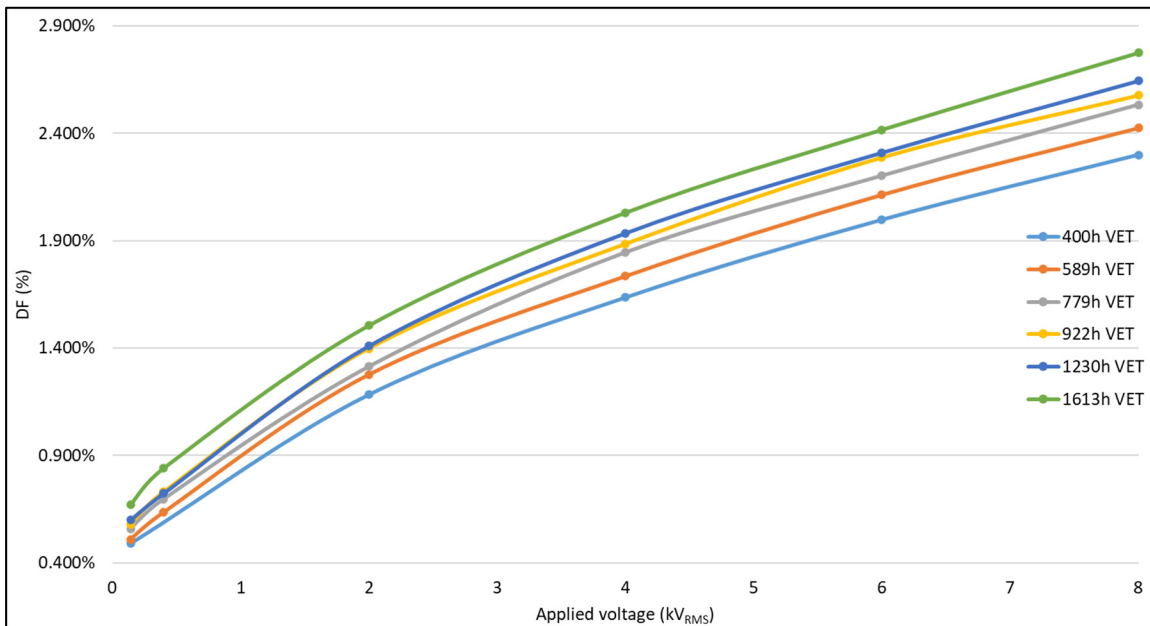


Figure 7.8 Measured DF measurements at 60 Hz at different stages of the ageing process

The measured DF values increased during the whole process of VET, between 400h and 1613h. The increase was more significant when measured at 8 kV_{RMS} compared to lower voltages.

Guarded measurements were also performed after 589 hours of VET and 1613 hours of VET. The results are shown in figure 7.9.

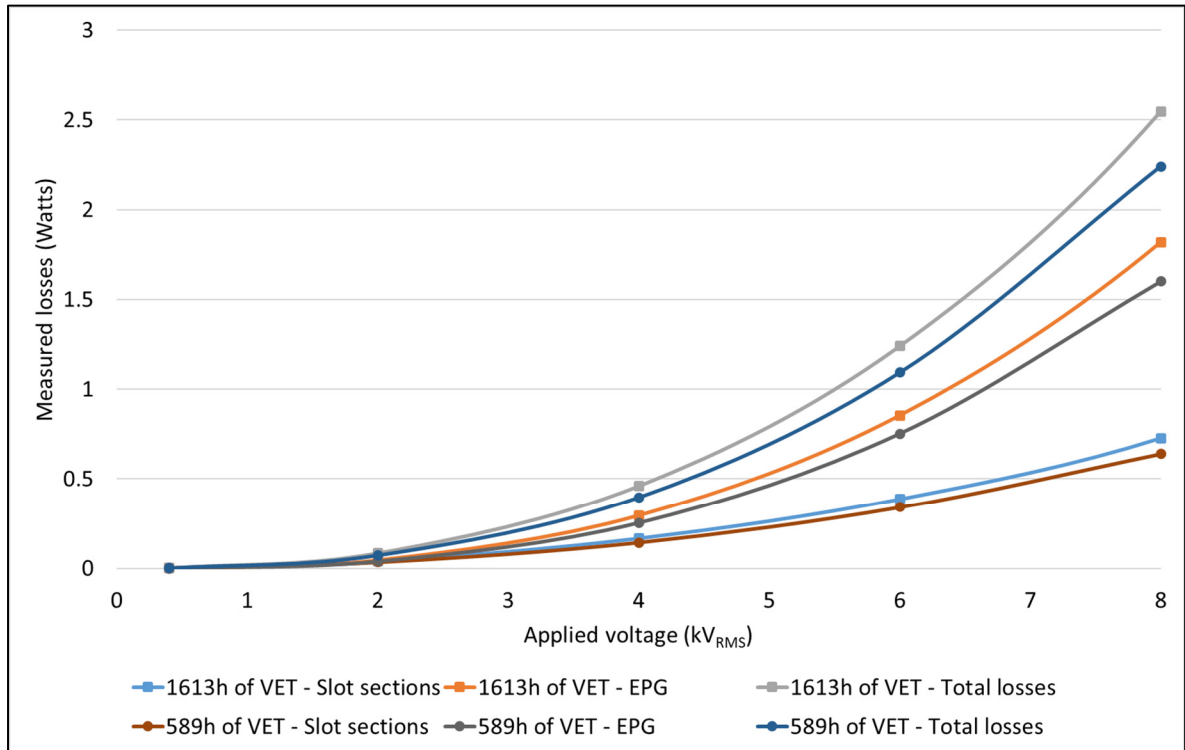


Figure 7.9 Results of guarded DF measurements after 589 hours and 1613 hours of ageing

It can be seen in figure 7.9 that the main increase in dielectric losses was measured from the guard electrodes, indicating that the losses from the EPG area were predominant in the measurements. It was previously explained in chapter 6 that the dielectric loss measurements are voltage sensitive and that, the main contribution of the dielectric losses at 8 kV_{RMS} and 60 Hz is from the interfacial polarization between the EPG and the insulation underneath it. The more significant increase at 8 kV_{RMS} can indicate changes in the EPG area or in the insulation underneath it. In section 7.1.1, it was mentioned that the surface resistivity of the EPG sections decreased as the coil aged through exposure to VET. The decrease in resistivity will increase the current and therefore, the losses as per $W=I^2R$. The DF measurements at higher voltage seem to be more sensitive to the change of the EPG coating rather than the degradation of the insulation in the slot sections.

7.1.4 Analysis of the fault

A visual inspection of coil 07 was performed following the fault after 1768 hours of total VET time. No visible indications of a fault were found.

Using a multimeter, it was possible to identify on which leg of the coil the fault happened. It was decided to cut the coil in smaller sections and to check for continuity between each strand and the OCP section of the individual coil sections. Unfortunately, after several cuts, it was not possible to measure any continuity between the strands and the OCP on any of the cut sections. It is possible that the heat generated by the cutting process changed the properties of the defect in a way that, it became isolated electrically.

The DFR measurements, PD measurements and DF measurements all indicated some level of deterioration of the coils. The conventional DF measurements showed a significant increase in measured values during the tip-up test. However, it was concluded that this increase in DF values was caused by the changes in the EPG coating surface resistivity and not by significant deterioration in the coil. The DFR measurements showed an increase in the measured values, prominently at 1 mHz. However, the increase was not enough to anticipate an imminent failure. The PD measurements did show a sudden increase in measured values.

It is possible that, even though the insulation was showing signs of deterioration, that a dielectric failure was not imminent in this case, prior the increase of test voltage. Indeed, it is possible that the increase of electric stress during stage 4 of the ageing process greatly accelerated the deterioration process that were already present during stage 3 or, that a whole different failure mechanism was triggered.

7.2 Coil 19

Coil 19 failed after 823 hours of total VET time. The last dielectric measurements prior failure were performed after 779 hours of total VET time.

7.2.1 Results of DFR measurements

Figure 7.10 and figure 7.11 show all the measured DFR curves respectively represented using a linear and logarithmic scaling for the y-axis. Those measurements were taken at the intervals described in table 5.1.

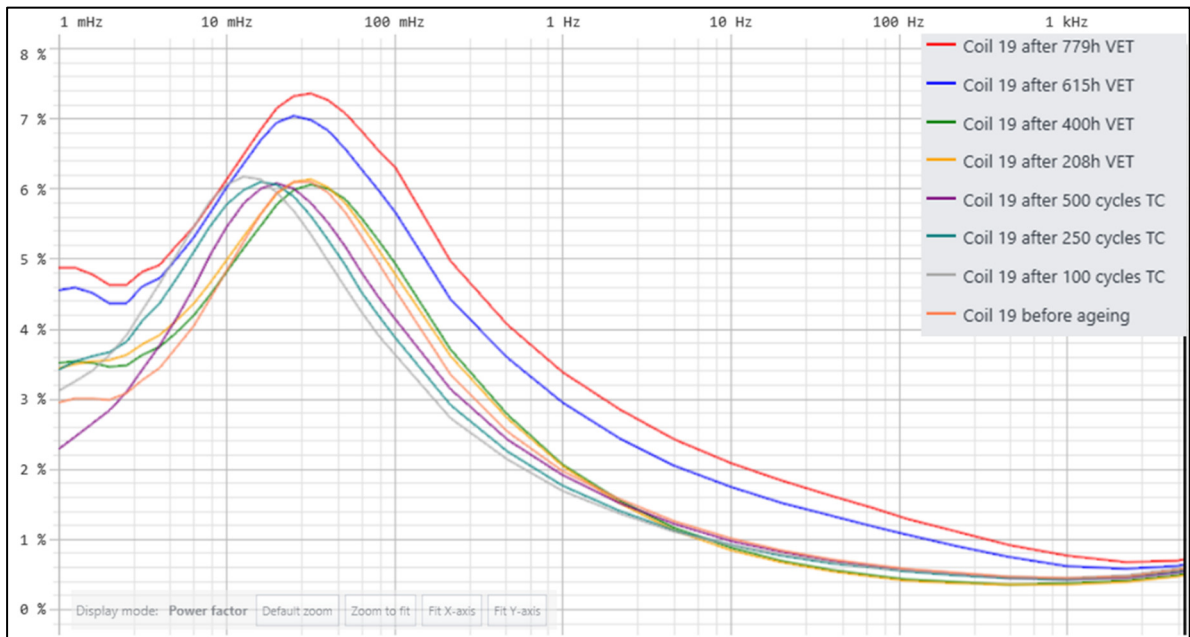


Figure 7.10 Power factor curves measured on coil 19 using a linear scaling for the y-axis

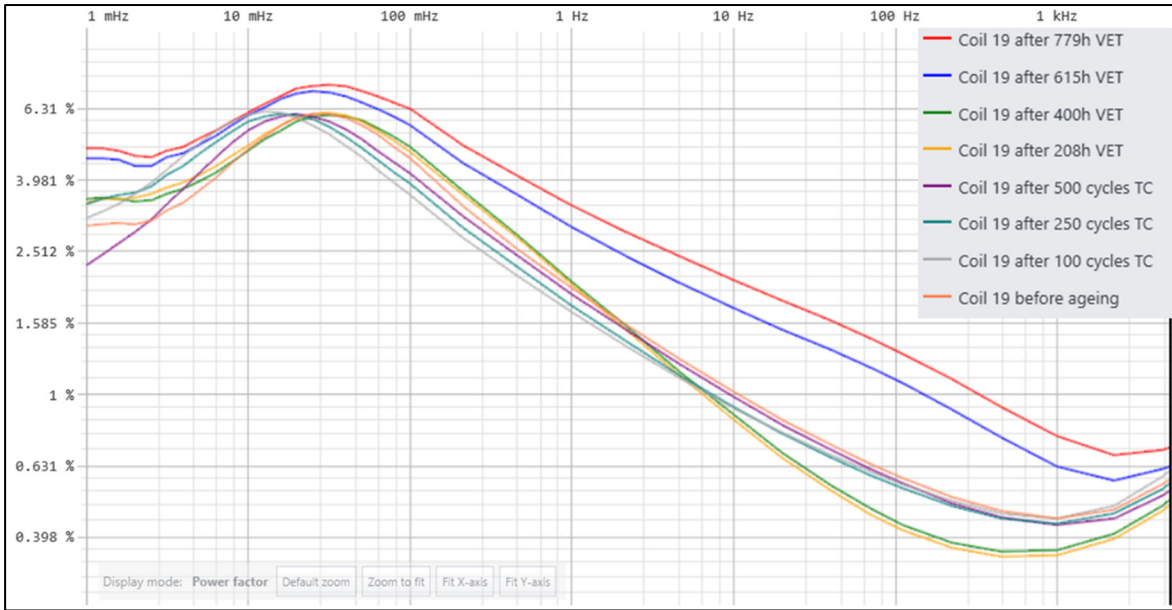


Figure 7.11 Power factor curves measured on coil 19 using a logarithmic scaling for the y-axis

Similar to the results of coil 07 (section 7.1), every measured DFR curves include a loss peak, in the range between 10 mHz to 100 mHz. The presence of the loss peak was previously explained in section 6.1

To improve the visualization of the curves presented in figure 7.10 and figure 7.11, the data is summarized in table 7.4 where the measured DF values at some of the measured frequencies are indicated as a function of the measurement interval.

Table 7.4 Summary of the measured DF values for coil 19 from figure 7.10 and figure 7.11

	1 mHz	10 mHz	100 mHz	1 Hz	10 Hz	60 Hz	100 Hz	1 kHz	5 kHz
Reference	2.96%	4.85%	6.31%	1.98%	1.02%	0.66%	0.60%	0.45%	0.58%
100 cycles	3.12%	6.06%	5.67%	1.70%	0.92%	0.63%	0.57%	0.45%	0.61%
250 cycles	3.42%	5.78%	4.93%	1.78%	0.92%	0.61%	0.55%	0.43%	0.57%
500 cycles	2.30%	5.46%	4.78%	1.91%	0.98%	0.64%	0.58%	0.43%	0.54%
208h VET	3.44%	4.99%	4.14%	2.04%	0.85%	0.48%	0.43%	0.35%	0.49%
400h VET	3.51%	4.82%	3.88%	2.08%	0.88%	0.50%	0.44%	0.37%	0.51%
589h VET	4.57%	6.02%	3.63%	2.95%	1.75%	1.22%	1.10%	0.63%	0.63%
779h VET	4.87%	6.14%	4.56%	3.39%	2.09%	1.49%	1.33%	0.76%	0.71%

The behavior of the DFR curves for coil 19 are very similar from the ones obtained for coil 07 for stage 1 of the accelerated ageing process. During that interval, there is an initial decrease in DF values. The loss peak created by the interfacial polarization between the EPG coating and the main insulation underneath moves to lower frequencies. Those behaviors were explained in section 7.1.1.

Figure 7.12 and figure 7.13 show the measured imaginary capacitance using respectively a linear and logarithmic scaling for the y-axis throughout the whole accelerated ageing process. Figure 7.14 shows the measured real capacitance.

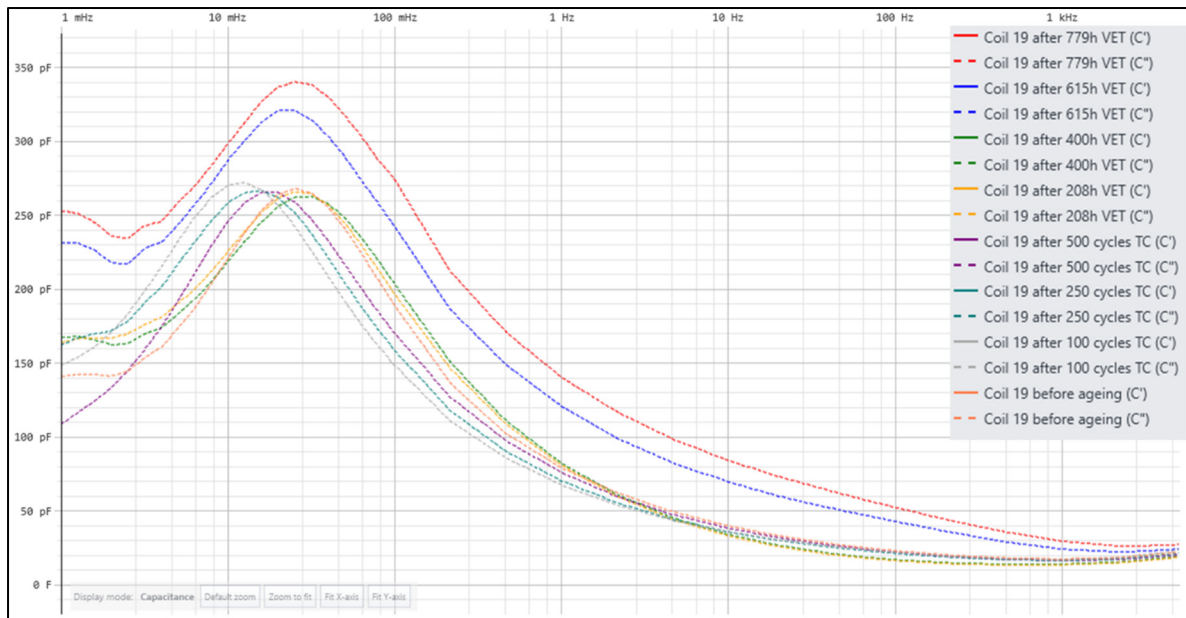


Figure 7.12 Measured imaginary capacitance curves on coil 19 displayed using a linear scaling for the y-axis

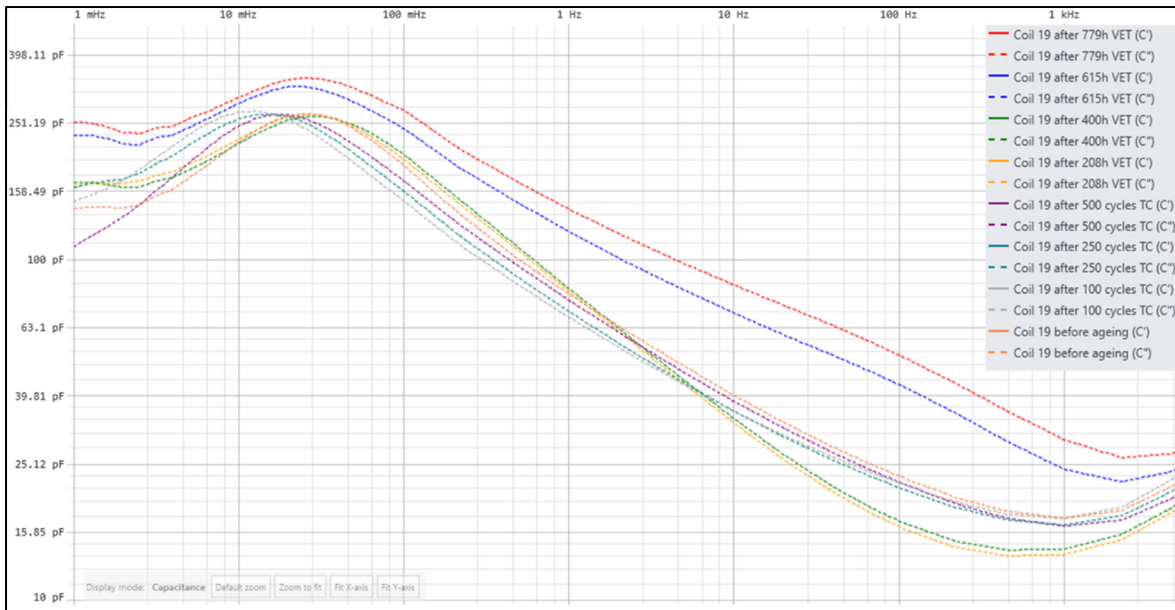


Figure 7.13 Measured imaginary capacitance curves on coil 19 displayed using a logarithmic scaling for the y-axis

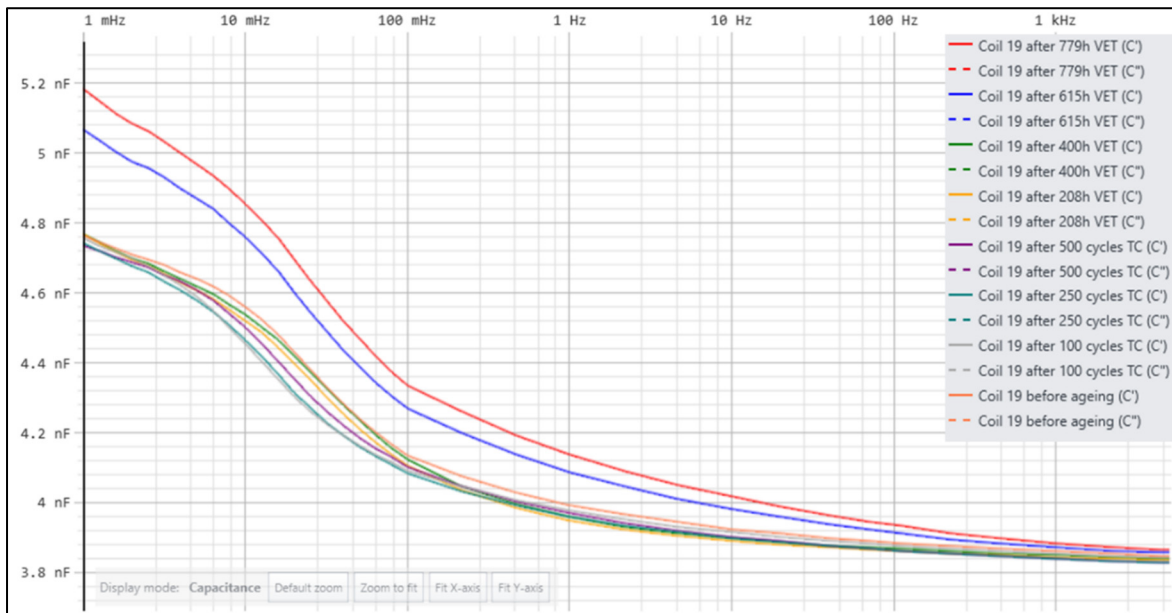


Figure 7.14 Measured real capacitance curves measured on coil 19

During stage 2 of the accelerated ageing process, the DFR curves were seen increasing with time exposure to the VET. After the first 208 hours of stage 2, the loss peak is seen moving to

higher frequencies. This situation was also seen in the results for coil 07 and is explained in section 7.1.1.

During stage 3 of the accelerated ageing process, a significant increase in the DFR curves and in the complex capacitance curves for the whole frequency range can be seen. This behavior was not noticeable for the two other coils investigated. Since the increase affects the whole frequency range and that the loss peak didn't change position in the frequency spectrum, it is likely that it is due to an anomaly in the slot sections, and not by the EPG coating or the insulation underneath it. As it was previously explained, a change in the EPG coating resistivity and/or the insulation underneath it will affect the position of the loss peak in the frequency spectrum and will affect the measured dielectric values.

The curves on figure 7.13 also show another loss peak, which seem to be occurring around 100 Hz. This behavior was not seen on the other two curves. This peak was visible for the measurements performed after 615 hours and 779 hours of VET and were preceding the failure of the coil. It is possible that this loss peak was created by the interaction of a resistive defect with the insulation. Such example of resistive defect can potentially be an electrical tree.

The increase in DF values was more significant when measured at 1 mHz, in comparison to when measured at 60 Hz. For example, the measured DF values at 1 mHz increased from 2.96%, measured before ageing, to 4.87%, measured after 779 hours of VET. For the same interval, the measured DF values increased from 0.66% to 1.49%. Nevertheless, unlike for coil 07 and for coil 20, the increased in losses was significant over the whole frequency range.

7.2.2 Results of PD measurements

Figure 7.15 shows the trend of the measured apparent charge as Q_{IEC} over the whole ageing process. The values displayed in the graph is the average of the Q_{IEC} values obtained over a period of 20 seconds, at a voltage level of 8 kV_{RMS}. Table 7.5 shows the evolution of the PRPD diagrams built over a period of 20 seconds, at a voltage level of 8 kV_{RMS}.

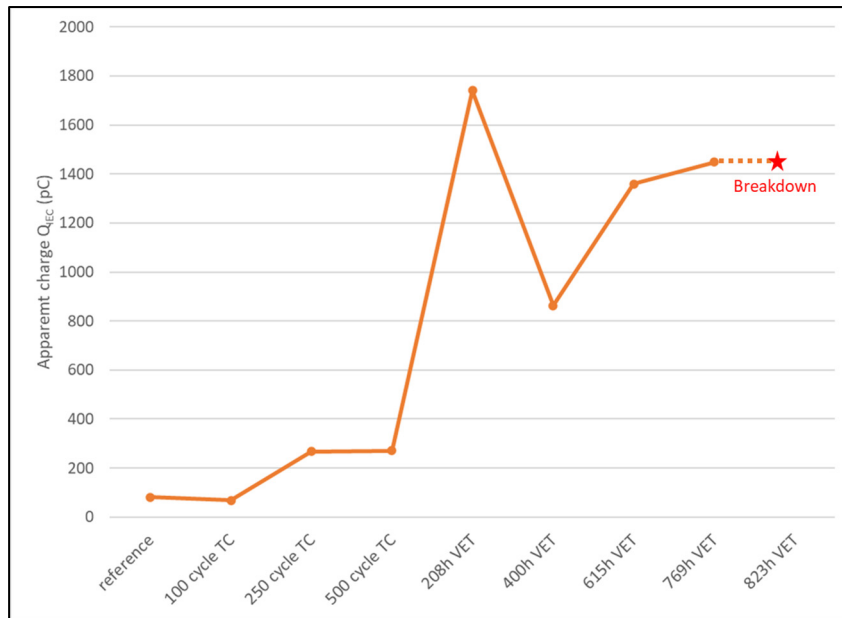
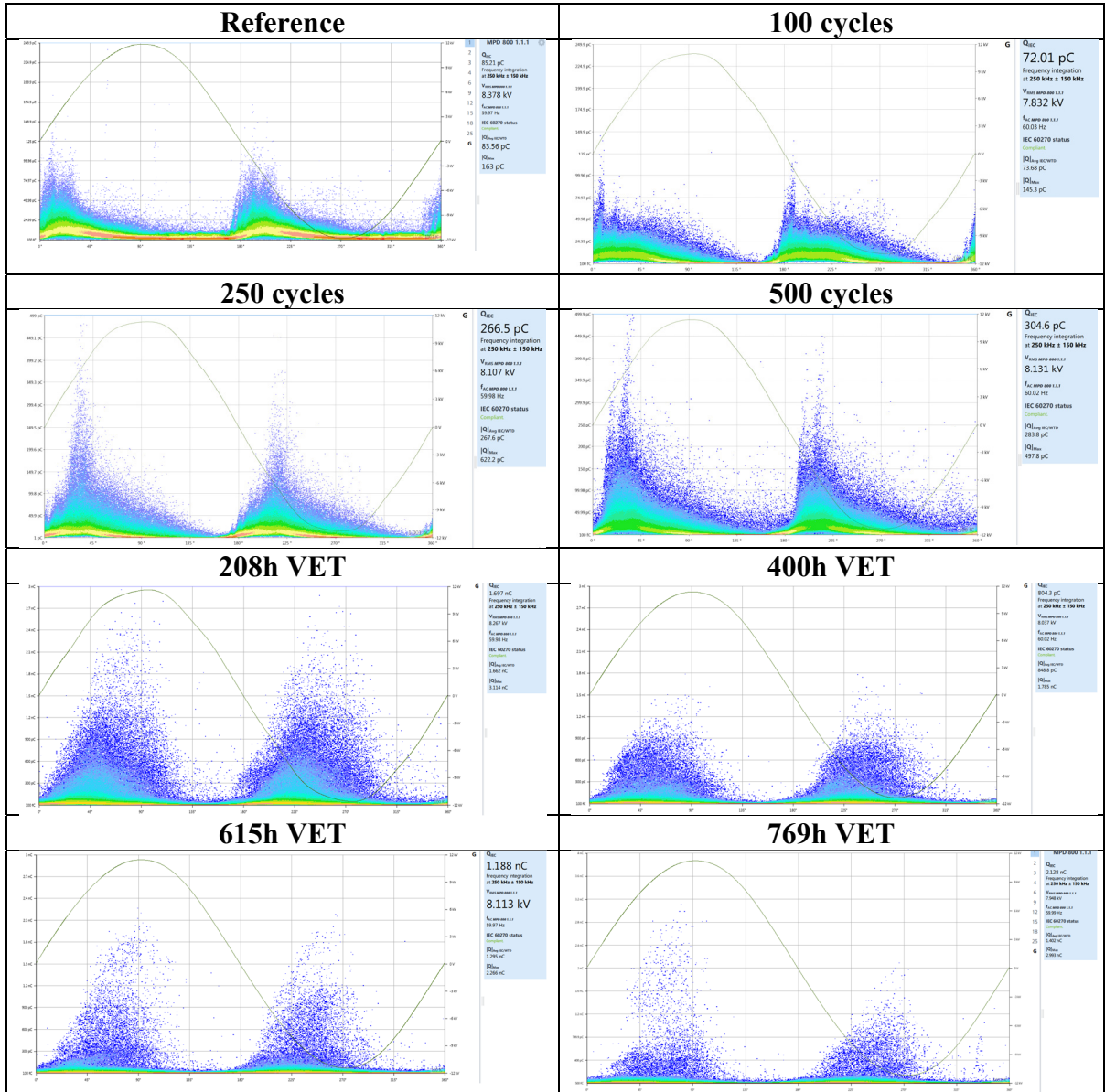


Figure 7.15 Trend of the measured apparent charge for coil 19

Table 7.5 Measured PRPD patterns at different stages of the ageing process of coil 19



The PD magnitude Q_{IEC} increased significantly throughout the aging process. The reference PD Q_{IEC} magnitude was approximately 85 pC before the ageing process began while it reached more than 1,400 pC during the measurement prior failure. It can be assumed that significant deterioration took place during the whole ageing process. When comparing the measured PRPD diagrams with the ones in figure 5.7, it seems that discharges due to cavities and delamination between tape layers were the main contributors of the measured PRPD patterns on coil 19. During the last measurement, discharges of higher magnitude and lower repetition

rates were captured predominantly during the first half cycle of the AC sine wave. While symmetrical PRPD patterns indicate PD activities within the insulation, a higher PD magnitude measured during the positive half cycle of the sine wave indicates PD activities occurring at the main conductor bundle, such as delamination of the insulation with the winding conductor. This type of defect is usually considered important as, the electric field is usually stronger closer to the main conductor bundle and therefore, discharges of higher magnitude are likely to occur.

7.2.3 Analysis of the fault

A visual inspection of coil 19 was performed following the fault after 823 hours of total VET time. It was possible to visually see a burnt mark on one of the two slot sections, at approximately 2 inches from one of the EPG. It was decided to do some cross-sectional cuts of the suspected faulty area in order to have a better observation of the defect. The cuts were afterward inspected using a stereoscope to find evidence of degradation. Figure 7.16 shows a picture of the suspected fault location while figure 7.17 shows a picture taken from the stereoscope.



Figure 7.16 Picture of the suspect fault area of coil 19

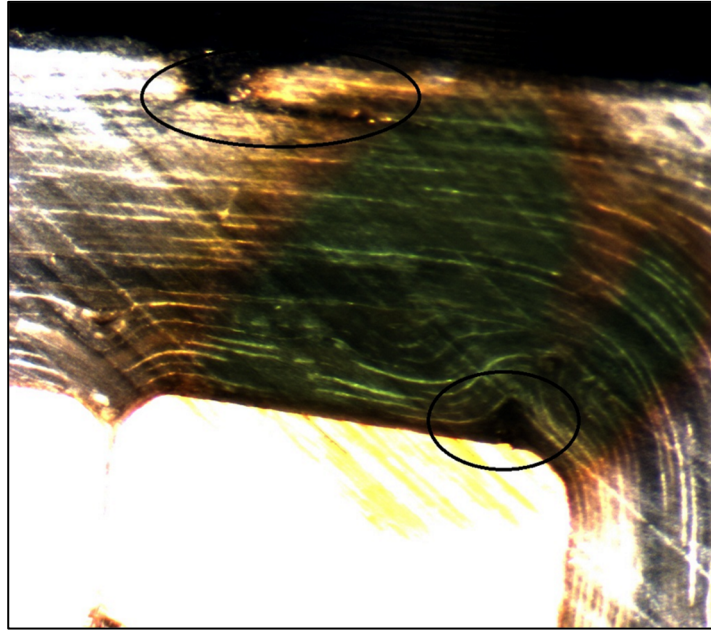


Figure 7.17 Picture of the cross-sectional cut in the suspected fault area using a stereoscope

On figure 7.17, two protrusions (circled in black) are visible on the failed disassembled coil. In section 7.2.2, it was mentioned that PD activities with higher magnitude were occurring adjacent to the conductor bundle, which was visible on the PRPD patterns measured after 779 hours of total VET time. This corroborates the large void that is visible in the black circle, at the bottom of figure 7.17. Discharges of higher magnitude and lower repetition rates were already visible on the PRPD measured after 615 hours of VET, However, the asymmetry was only visible on the PRPD patterns obtained after 779 hours of VET exposure. It is possible that the void was first partially filled with epoxy but that the impregnation was incomplete at this location. As the electric field is near the maximum in the corner of the conductor, voids can be ionized, and discharges can be initiated. It is possible that the discharges created an electrical tree, which progressed and reached the conductor between 615 hours and 779 hours of VET. This would explain why there was no visible asymmetry in the measured PRPD patterns obtained prior 779 hours of VET.

It is important to mention that it was not possible to visualize the complete electrical tree and therefore, the aforementioned explanation is only at best, a plausible scenario. Even though it

is not possible to know without a doubt if the measured losses were from a localized defect, or from distributed small defects, it does seem that the losses dissipated prior failure influenced greatly the measured DFR curves. Therefore, it seems that the DFR measurements were effective at detecting the forthcoming dielectric failure.

It can also be seen that several voids or gaps between tape layers are visible, especially in the corner of the coil. These less severe but more distributed voids may have potentially contributed as well to the gradual increase of measured DF values and DFR curves throughout the ageing process. As comparison, figure 7.18 shows a cross-sectional cut of a non-aged coil of the same manufacturing batch.

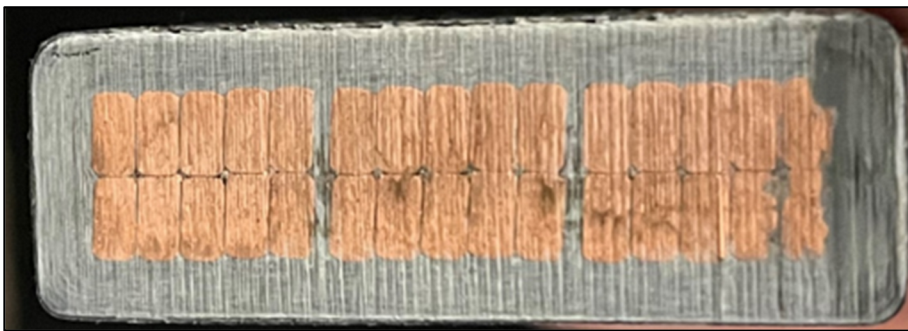


Figure 7.18 Cross-sectional cut of an unaged coil

7.3 Coil 20

Coil 20 failed after 719 hours of total VET time. The last dielectric measurements prior failure were performed after 628 hours of total VET time after which, the voltage was increased from 30 kV_{RMS} to 35 kV_{RMS}.

7.3.1 Results of DFR measurements

Figure 7.19 and figure 7.20 show all the measured DFR curves respectively represented using a logarithmic and linear scaling for the y-axis. Those measurements were taken at the intervals described in table 5.1.

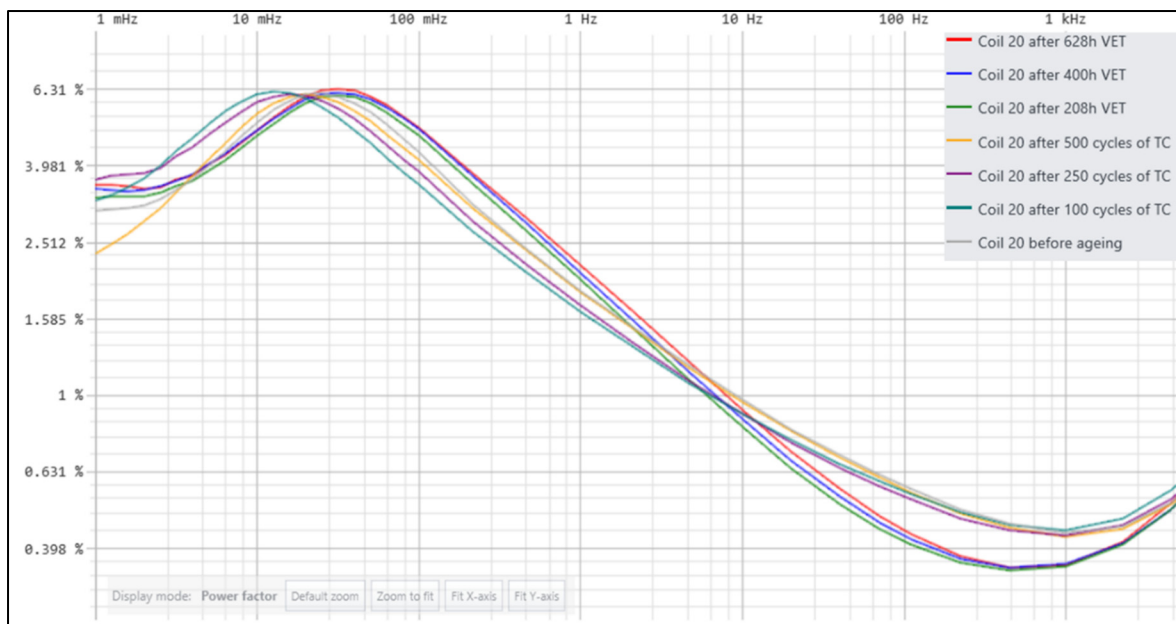


Figure 7.19 Power factor curves measured on coil 20 using a logarithmic scaling for the y-axis

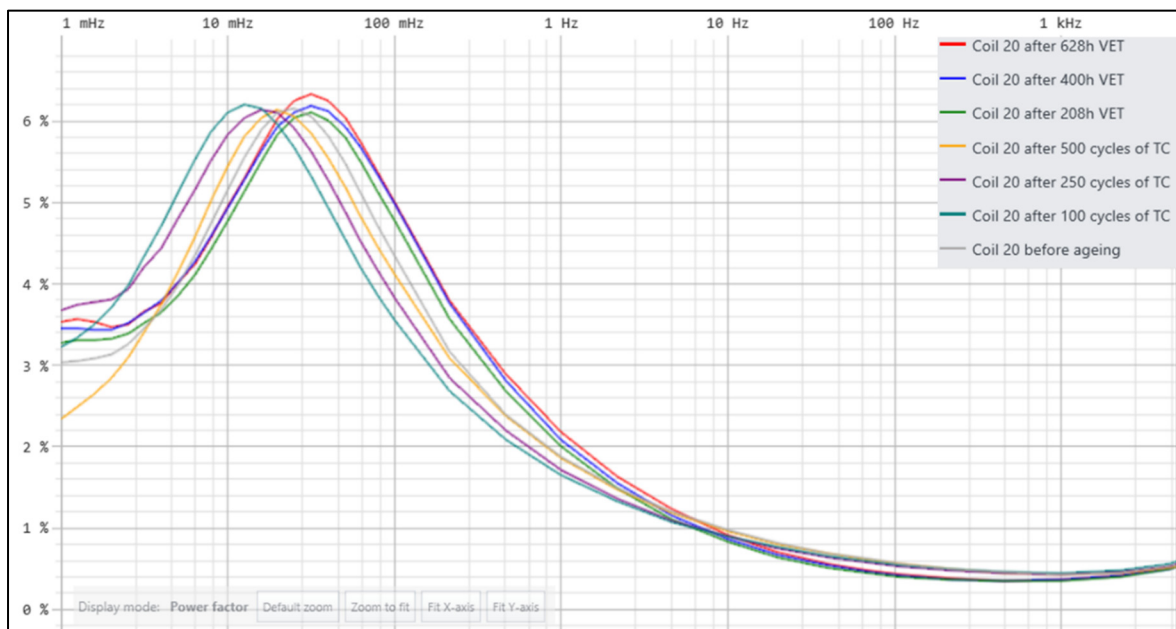


Figure 7.20 Power factor curves measured on coil 20 using a linear scaling for the y-axis

Every measured DFR curves include a loss peak, in the range between 10 mHz to 100 mHz. The presence of the loss peak was previously explained in chapter 6.

To improve the visualization of the curves presented in figure 7.19 and figure 7.20, the data is summarized in table 7.6 where the measured DF values at some of the measured frequencies are indicated as a function of the measurement interval.

Table 7.6 Summary of the measured DF values for coil 20 from figure 7.19 and figure 7.20

	1 mHz	10 mHz	100 mHz	1 Hz	10 Hz	60 Hz	100 Hz	1 kHz	5 kHz
Reference	3.04%	5.16%	4.33%	1.88%	0.98%	0.64%	0.58%	0.44%	0.54%
100 cycles	3.23%	6.11%	3.56%	1.66%	0.90%	0.61%	0.56%	0.44%	0.59%
250 cycles	3.67%	5.83%	3.83%	0.72%	0.89%	0.60%	0.54%	0.43%	0.56%
500 cycles	2.35%	5.45%	4.12%	1.87%	0.96%	0.63%	0.57%	0.43%	0.54%
208h VET	3.28%	4.77%	4.77%	2.01%	0.83%	0.47%	0.42%	0.36%	0.53%
400h VET	3.46%	4.93%	4.98%	2.09%	0.87%	0.49%	0.43%	0.36%	0.53%
628h VET	3.54%	4.95%	4.99%	2.19%	0.92%	0.51%	0.44%	0.36%	0.55%

The behavior of the DFR curves for coil 20 are very similar from the ones obtained for coil 07 and for coil 19 for stage 1 of the accelerated ageing process. During that interval, there is an initial decrease in DF values. The loss peak created by the interfacial polarization between the EPG coating and the main insulation underneath moves to lower frequencies. Those behaviors were explained in section 7.1.1.

Figure 7.21 and figure 7.22 respectively show the measured real capacitance and the imaginary capacitance throughout the whole accelerated ageing process.

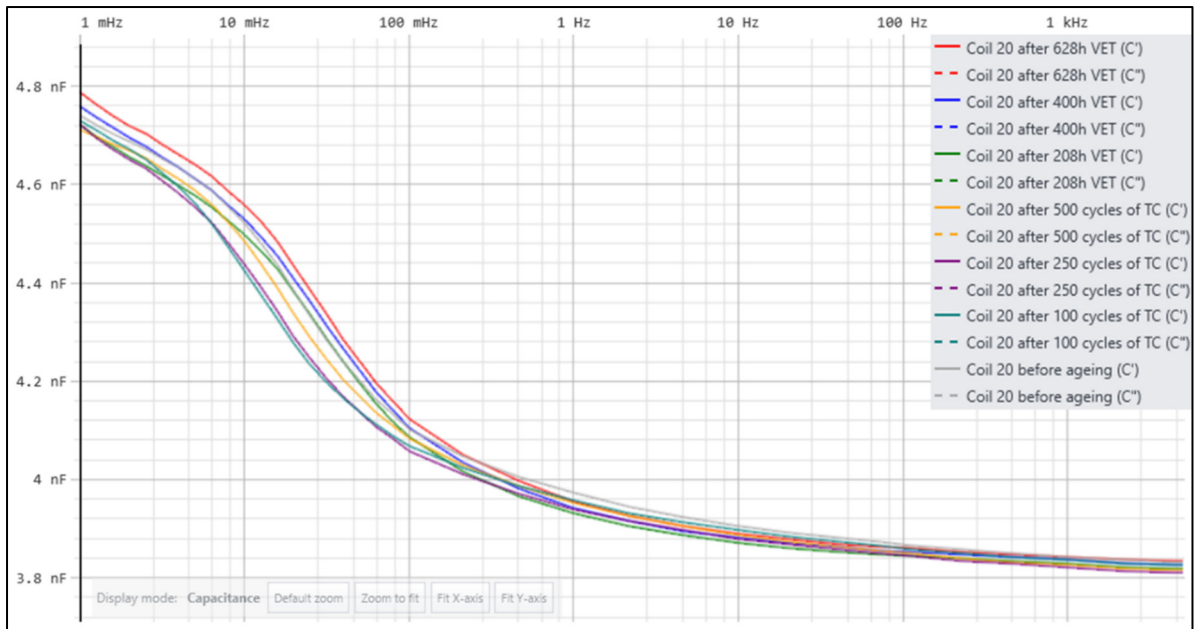


Figure 7.21 Measured real capacitance curves on coil 20

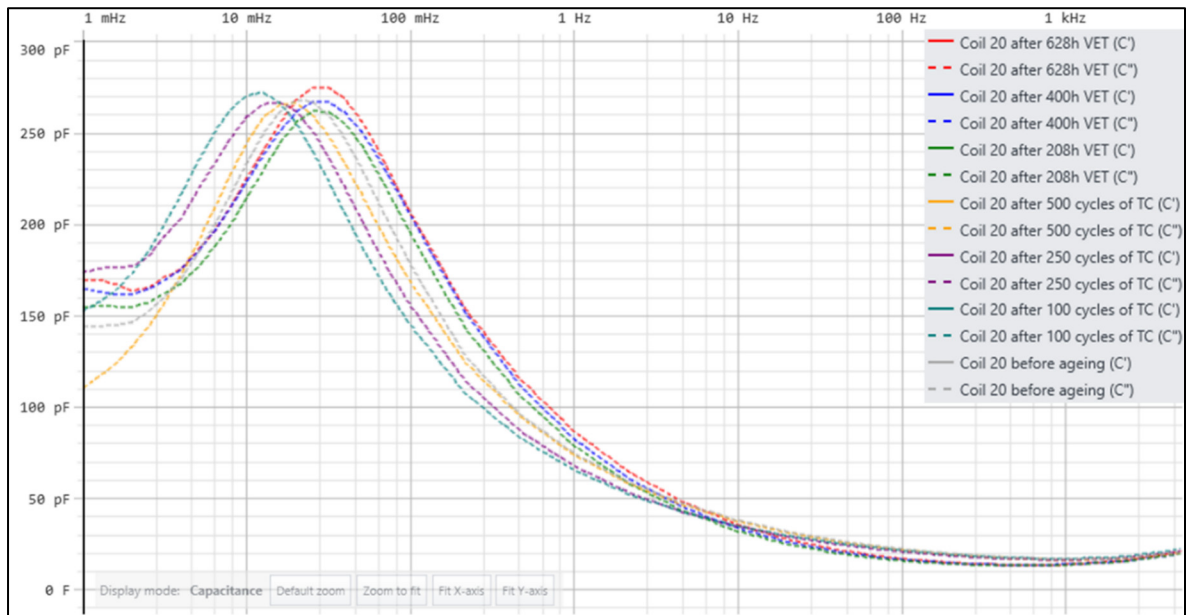


Figure 7.22 Measured imaginary capacitance curves on coil 20

During stage 2 of the accelerated ageing process, the DFR curves were seen increasing with time exposure to the VET. After the first 208 hours of stage 2, the loss peak is seen moving to

higher frequencies. This situation was also seen in the results for coil 07 and for coil 19. More information was provided in section 7.1.1.

The DF values were seen increasing throughout the stages 2 and 3 of the ageing process. The increase in DF values was more significant when measured at 1 mHz, in comparison to when measured at 60 Hz. This phenomenon is similar to the results from coil 07. For example, the measured DF values measured at 1 mHz were initially 3.04% and increased to 3.54% during the last measurement prior failure. Interestingly, the measured DF values were lower prior failure when measured at 60 Hz, in comparison to the initial measurement. This initial decrease in measured DF values at 60 Hz was explained in section 7.1.1 and is believed to be due to additional curing of the epoxy resin.

7.3.2 Results of PD measurements

Figure 7.23 shows the trend of the measured apparent charge as Q_{IEC} over the whole ageing process. The values displayed in the graph is the average of the Q_{IEC} values obtained over a period of 20 seconds, at a voltage level of 8 kV_{RMS}. Table 7.7 shows the evolution of the PRPD diagrams built over a period of 20 seconds, at a voltage level of 8 kV_{RMS}.

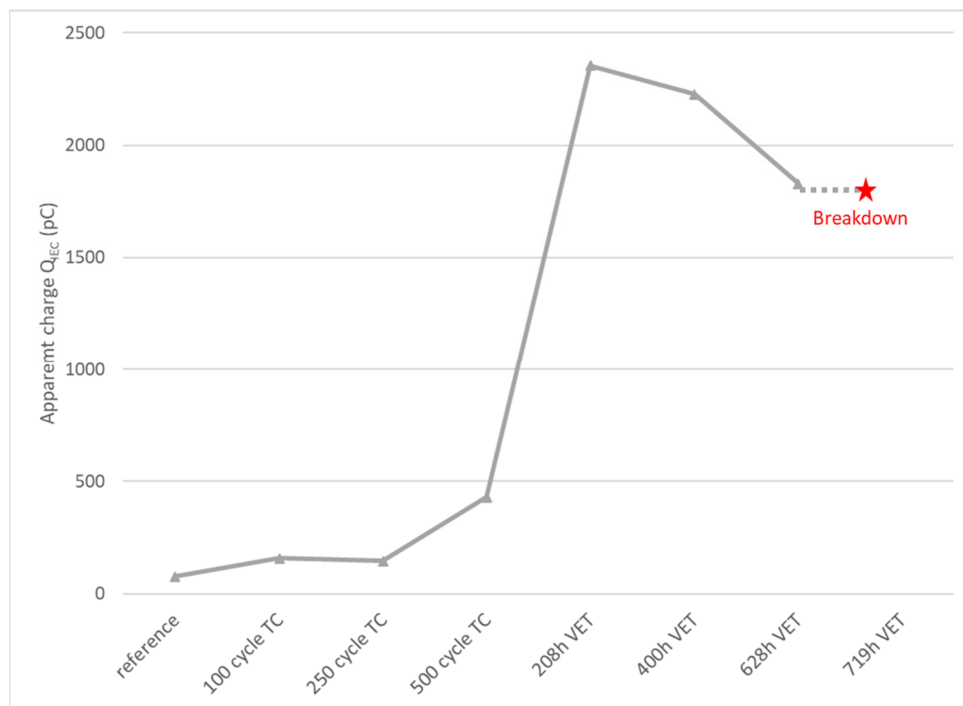
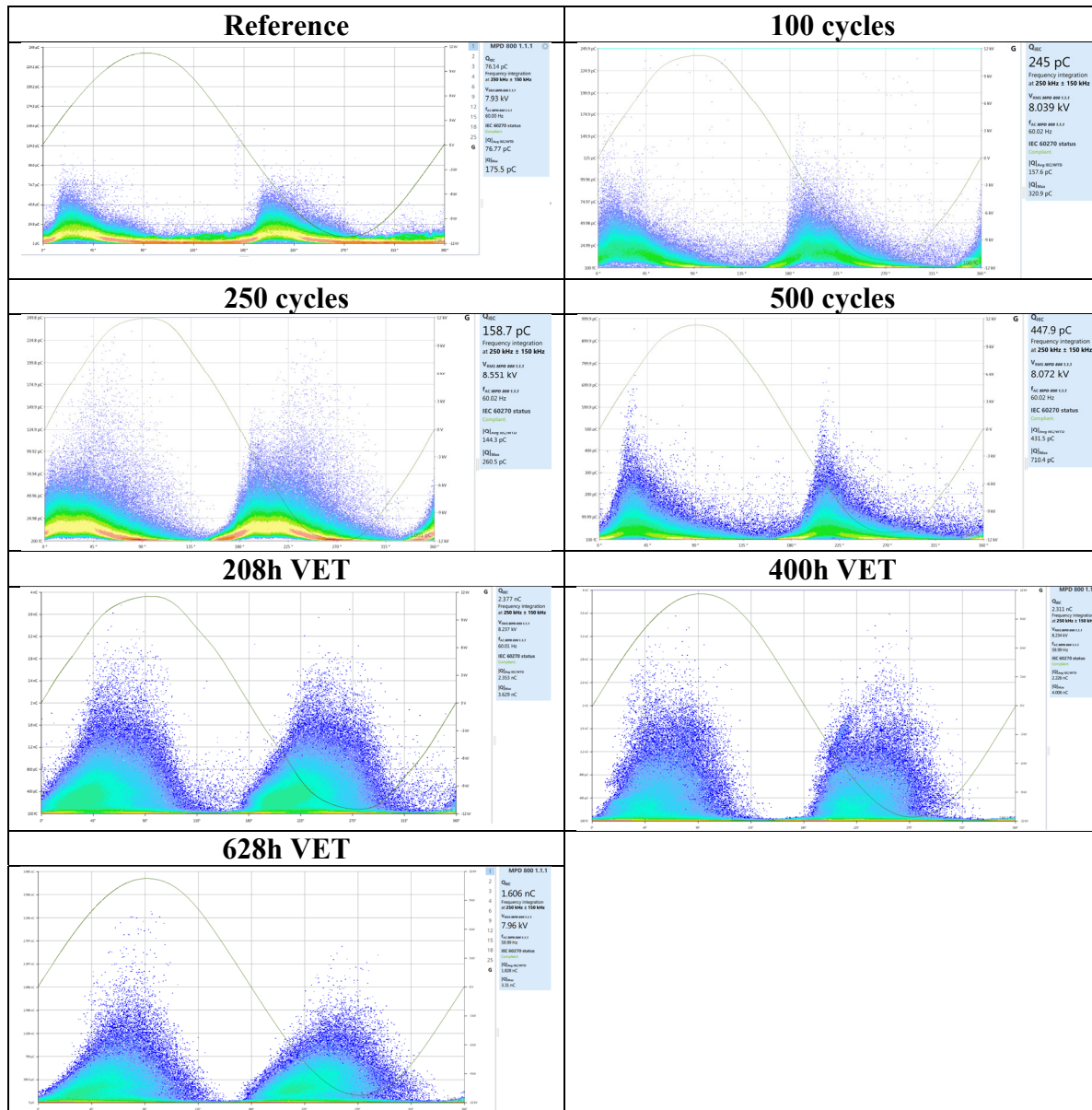


Figure 7.23 Trend of the measured apparent charge for coil 20

Table 7.5 Measured PRPD patterns at different stages of the ageing process of coil 20



The PD magnitude Q_{IEC} increased significantly throughout the aging process. The reference PD Q_{IEC} magnitude was approximately 77 pC before the ageing process began while it reached more than 1,800 pC during the measurement prior failure. It can be assumed that significant deterioration took place during the whole ageing process. When comparing the measured PRPD diagrams with the ones in figure 5.7, it seems that discharges due to cavities and delamination between tape layers were the main contributors of the measured PRPD patterns

on coil. During the last measurement, a slight asymmetry was visible in the PRPD patterns. This situation was also encountered with coil 07 and coil 19. On those cases, the asymmetry was more obvious in comparison to coil 20.

7.3.3 Analysis of the fault

A visual inspection of coil 20 was performed following the fault after 719 hours of total VET time. No visible indications of a fault were found.

Using a multimeter, it was possible to identify on which leg of the coil the fault happened. The location of the fault was narrowed down to a small section of the coil, approximately 0.5 inches from one of the connections between the OCP and one of the EPG sections. This was done using an iterative process. One small section of the OCP was removed and the continuity between the main conductor bundle and the remaining OCP section was checked. If there was still continuity between the main conductor bundle and the OCP section connected the EPG, the process was repeated until the resistance meter showed overload. Figure 7.24 illustrates the process used to locate the fault internally while figure 7.25 shows a picture of the fault location.

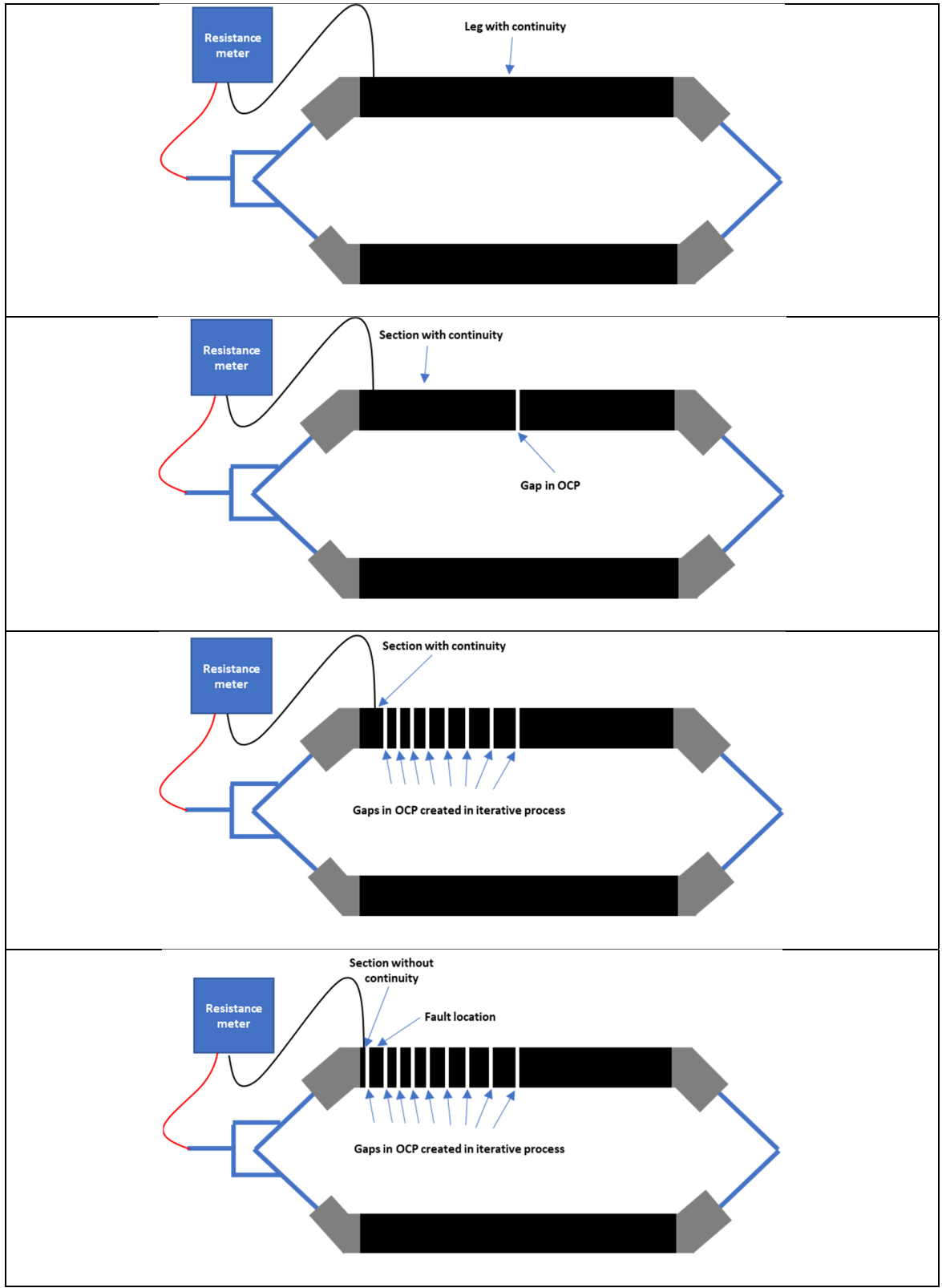


Figure 7.24 Sketches summarizing the process for localization of the fault

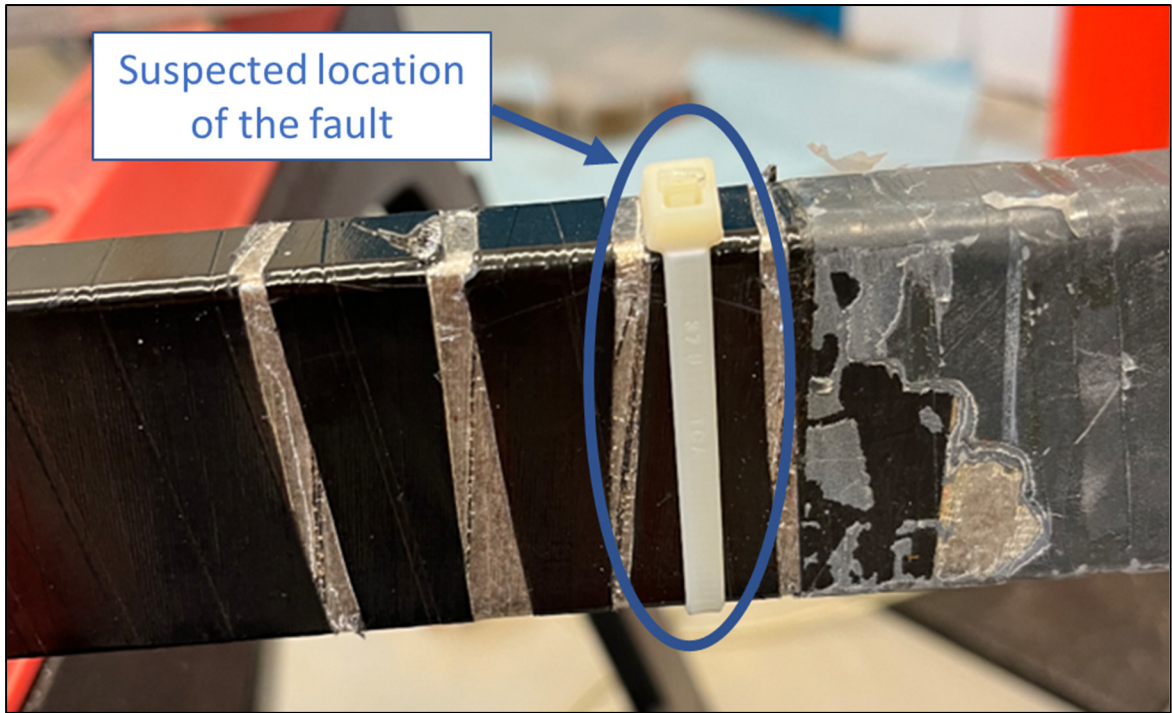


Figure 7.25 Picture of the suspected fault area

It was decided to do some cross-sectional cuts of the suspected faulty area to have a better observation of the defect. The cuts were afterward inspected using a microscope to find evidence of degradation. Figure 7.26 and figure 7.27 show two pictures taken from the same cross-sectional cut.

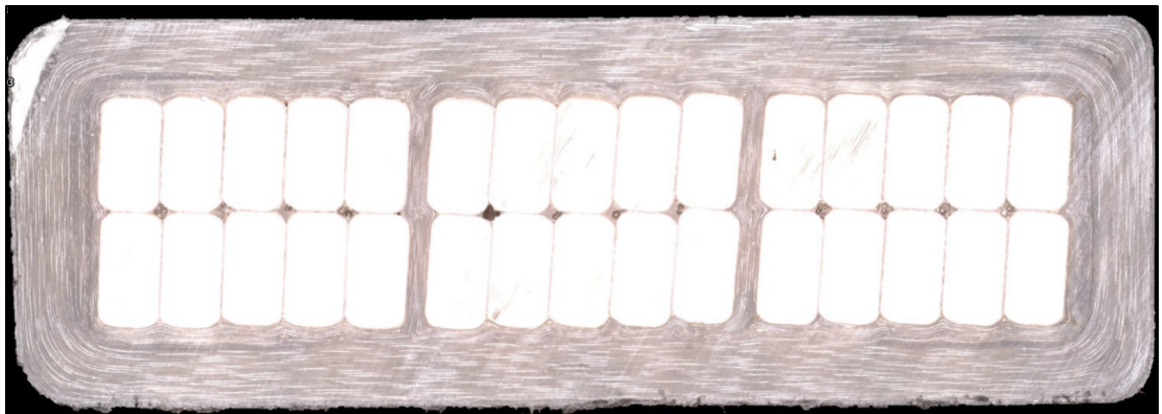


Figure 7.26 Picture of the cross-sectional cut in the suspected fault area using a microscope

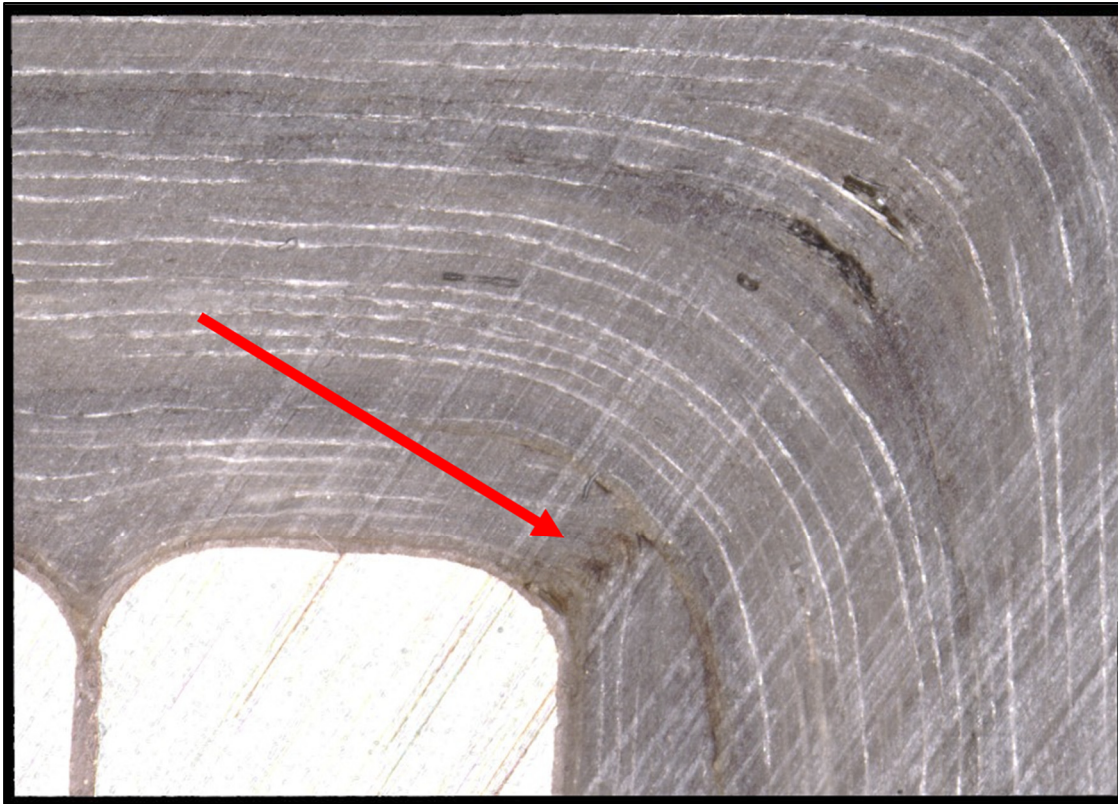


Figure 7.27 Picture of the upper right corner of figure 7.26

On figure 7.27, a brown line can be seen initiating at the corner of the conductor bundle (indicated by a red arrow). It is believed that this brown line is the propagation path of the dielectric puncture, which completely bridge the insulation between the conductor bundle and the OCP layer. For comparison, figure 7.26 shows the complete cross-sectional cut. It can be seen that the brown layer is only visible in the upper right corner of the coil and not in the other corners.

Besides the significant increase in PD activities, there was no significant increase in the measured DFR curves. There was no indication of an imminent failure or major deterioration on the measured DFR curves. Similar to coil 07, the voltage was increased from 30 kV_{RMS} to 35 kV_{RMS} shortly before failure and before any additional dielectric measurements were taken. It is therefore possible that, even though the insulation was showing some signs of deterioration from the PD measurements that a dielectric failure was not imminent in this case, prior the increase of test voltage. Indeed, it is possible that the increase of electric stress during stage 4

of the ageing process greatly accelerated the deterioration process that were already present during stage 3 or that a whole different failure mechanism was triggered.

CHAPTER 8

APPLICATION FOR COMPLETE STATOR WINDINGS

The investigations described in this document was performed on individual coils and bars. Those components are ultimately assembled to form a complete stator winding. Investigations on smaller components are commonly done in order to understand deterioration phenomena of complete equipment, as it is much simpler, requires fewer logistics and is less expensive to do. Some of the investigations done in this work would have been practically impossible to perform on a complete assembled winding, are at least, would have been quite challenging on a cost and logistic perspective. However, the end goal of such investigation is to apply the understanding gained from smaller experiments on complete machines as a diagnostic tool. Therefore, in this chapter, some of the results showed in chapter 7 are used for the assessment of the insulation of complete stator windings.

8.1 The value of the initial measurement

For complete stator windings, the industry has usually considered that the initial dielectric loss measurements are usually of little significance (Stone and al., 2014); (IEEE, 2001). There are two main reasons for this. At the time of writing this document, there are no globally accepted criteria for diagnostic dielectric loss measurements for complete stator windings (IEEE, 2001); (IEC, 2015). The main reason is that the EPG sections of complete stator windings cannot be mitigated using guard electrodes and its influence will be significant.

In chapter 6, it has been demonstrated that the effect of the EPG can be minimized when the test voltage is maintained low in comparison to the rated voltage of the machine. Figure 6.8 showed that when an applied voltage of $141 V_{RMS}$ is applied across the insulation, approximately 77% of the total measured loss comes from the slot sections. This percentage increases to approximately 85% when the applied voltage was decreased to $7 V_{RMS}$. Those percentages are significantly higher than the results from a conventional DF measurement performed at $2 kV_{RMS}$, in which only 32% of the total measured losses are coming from the slot sections. If the influence of the EPG coating can be mitigated during dielectric loss

measurements, then it makes comparative measurements much easier to interpret. Therefore, if a database containing enough data were built from dielectric loss measurements performed at low voltage, the meaning of the initial measurements could be increased significantly. In addition, if the influence of the EPG is kept low, it offers the possibility to potentially compare the results from guarded measurements on individual components, to measurements on complete stator windings. For example, table 8.1 shows a comparison between guarded measurements performed at the factory at 2 kV_{RMS} with unguarded measurements performed at 141 V_{RMS} and 7 V_{RMS}. The unguarded values measured at lower voltage are closed from the guarded measurements taken at 2 kV_{RMS}. However, these later values show great discrepancies with the unguarded measurements performed at 2 kV_{RMS}.

Table 8.1 Results of typical DF measurements performed with guards at the factory with measurements performed at lower voltage, without guards

Coil ID	Dissipation Factor measured at 60 Hz				
	With guards		Without guards		
	2 kV	8 kV	2 kV	141 V	7 V
2	0.694	0.774	N/A	0.690	N/A
7	0.712	0.807	1.312	0.650	0.530
19	0.733	0.804	1.367	0.660	0.540
20	0.730	0.811	1.349	0.640	0.520

8.2 Influence of stator winding capacitance

The capacitance value of the test object has tremendous influence on the sensitivity to detect ageing using dielectric loss measurements. As described in section 3.4, the measured DF values are the ratio between the measured losses in watts, and the total measured capacitive reactive power, in vars. Therefore, for a given localized anomaly, dissipating a specific number of watts or milliwatts, it is easy to see that the measured DF will greatly differ if the test object has a small capacitance, in comparison to a test object with a large capacitance.

The capacitance of the coils used for the investigation described in this document was approximately 3.6 nF, when measured at 60 Hz. They were manufactured as part of a new 28 MVA, 13.2 kV hydro generator. Each phase had two parallel windings, with each of them

having 54 coils connected in series. For a complete stator winding, it is not possible to test coils individually. Instead, each phase of the stator winding is tested individually. In more rare cases, the windings of each phase are separated and then, tested separately. Considering that each coil of a winding has a similar construction, it means that each parallel winding has a total capacitance of approximately 195 nF, or that each phase has a capacitance of 389 nF. In chapter 7, it has been demonstrated that the measured DFR curves change as the coils were ageing. In all cases, the DFR curves were seen increasing with exposure to VET. The increase was more significant for coil 19. Let's consider a scenario, where it is assumed that the increase in dissipated watts in coil 19 was due to one specific localized defect. This would mean that for a complete stator winding, the dissipated watts would remain constant as, they were produced by one single localized defect. However, since the capacitance would increase, the DF values would decrease as the capacitance is increased. Figure 8.1 shows the theoretical calculated DF values with different values of winding capacitance.

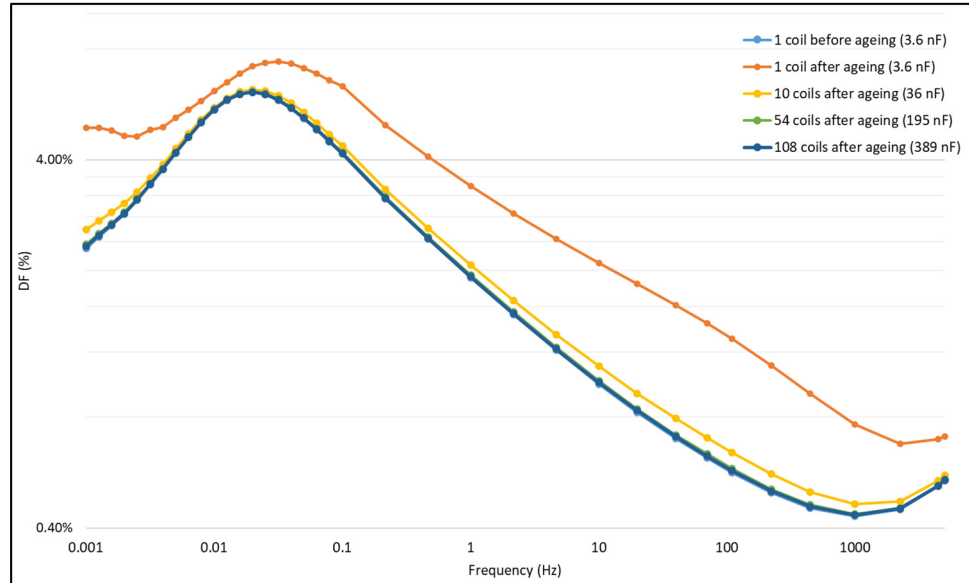


Figure 8.1 Projected DFR curves of coil 19 with different capacitance values

The anomaly detected on coil 19, would not have been detected if that stator coil was tested as part as a complete winding (194 nF), or even worst, as a complete phase (389 nF). However,

if the dissipated watts measured on coil 19 were produced by several smaller defects, which are distributed along the whole winding length, the measured DF values would not be significantly affected by the capacitance of the test object. Examples of such distributed issues or degradation process are thermal ageing and contamination of the winding. Therefore, dielectric loss measurements on complete stator windings are more sensitive to deterioration mechanisms which will affect several locations along the winding length and less to localized defects (Stone and al., 2014); (IEEE, 2001).

To illustrate this, the results of DFR measurements which were performed before and after the rewind of a 172 MVA hydro generator, are shown in figure 8.2. Prior rewind, the machine had been in operation for 48 years. Even though no significant investigations were performed on the removed winding, it is fair to assume that the winding had globally aged during those 48 years. It can be seen that the measured dielectric losses are significantly higher for the old winding, in comparison to the new winding and thus, for the whole frequency range.

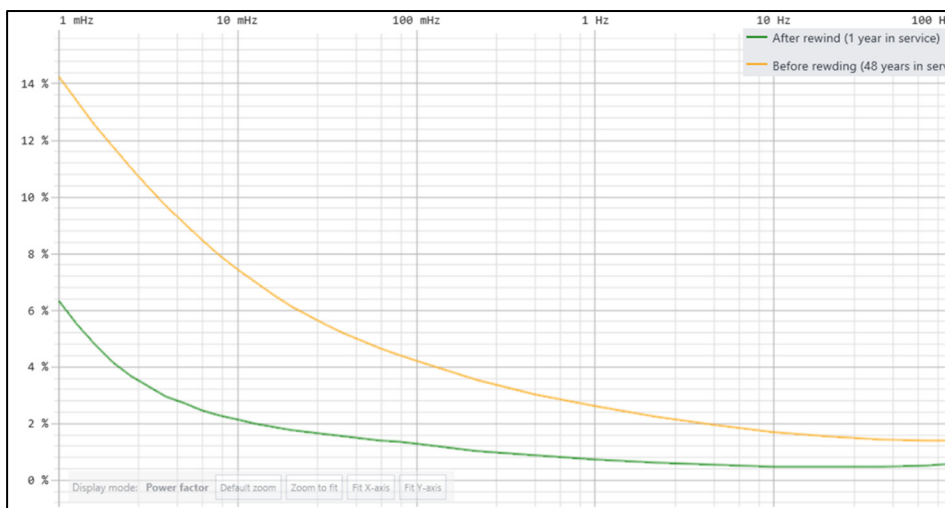


Figure 8.2 DFR curves from measurements performed on a 172 MVA hydro generator

Another example is the results of DFR measurements that were performed on a 16 kV turbo generator which had been exposed to ambient environment, in summer, for several days prior the measurements. The measurements in the lower frequency range were higher than the

previous reference measurements but, were very similar around power frequency. It was mentioned in chapter 6 that the EPG coating is highly resistive at low voltage and therefore, limited contribution from the endwinding is expected at 1 mHz. An exception is when a conductive layer of contamination is deposited on the surface of the EPG coating. Example of conductive contaminants can include by-products from a nearby manufacturing process or moisture. In these scenarios, the contribution from the contaminant deposited on the surface of the EPG coating will be important. The DFR measurements were repeated after the winding had been dried for three days. The measured curves were then much closer to the reference measurement over the whole frequency range. Figure 8.3 shows the three DFR curves measured on the turbo generator.

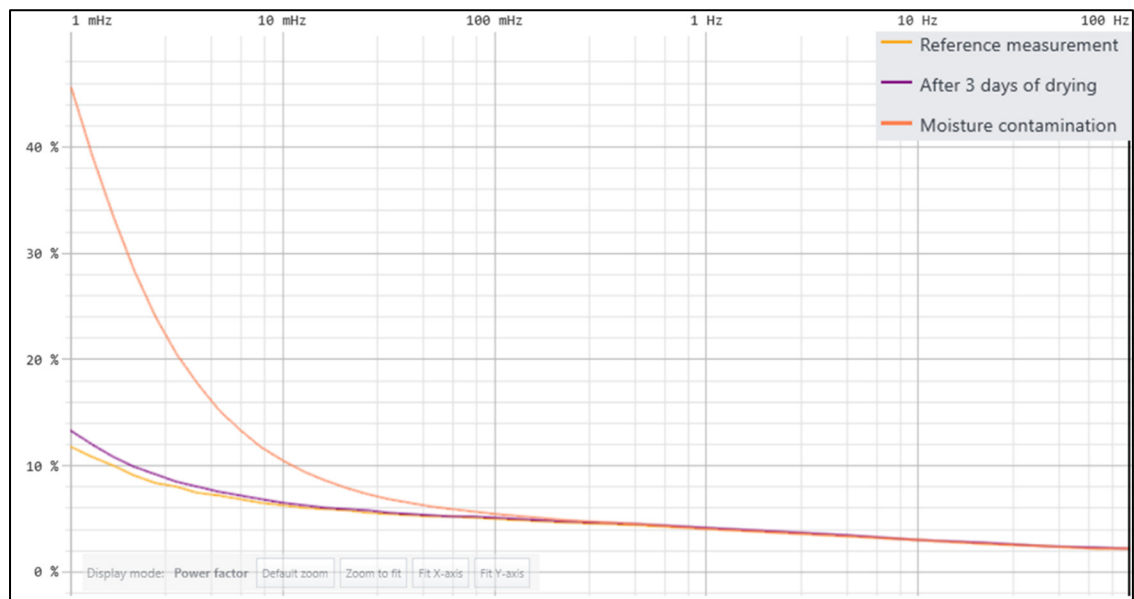


Figure 8.3 DFR curves from measurements performed on a 16 kV turbo generator

8.3 Assessment of the loss peak

In chapter 6 and chapter 7, it was shown that the position of the loss peak in the frequency spectrum can reveal changes in the resistivity of the EPG coatings. Therefore, for machines which are equipped with SiC base EPG coating, the assessment of the changes in the loss peak could reveal anomalies or changes in the resistivity of the EPG coating. As mentioned in the

previous section, for complete stator windings, several EPG sections will be measured simultaneously and therefore, the measurements will be sensitive to changes which affect most areas, rather than changes in a few EPG sections.

CONCLUSION

The purpose of this research project was to verify if the use of DFR measurements can be successfully applied to assess the insulation system of stator windings. To this end, an accelerated ageing protocol was prepared and applied to three different stator coils. Different dielectric measurements were performed throughout the ageing process to detect the deterioration of the insulation using DFR measurements, and to compare it with other conventional diagnostic methods, such as PD measurements and in one case, conventional DF measurements at 60 Hz.

Among all three coils, the DFR curves were seen increasing as the ageing process progressed. This was also the case with the PD measurements, which the results were used as a comparison. On two of the three coils, even if the dielectric losses did increase, the dielectric failure occurred before any indication of an imminent failure was visible on the measured DFR curves. However, it is possible that the sudden failure of those two coils were caused by a increase in test voltage, which triggered additional deterioration phenomena which were not present during previous measurements. For the other coil, the applied voltage was held constant for the whole duration of the voltage endurance test. On this coil, it was possible to see an important progressive deterioration from the DFR curves and to anticipate an imminent failure. As a comparison, the PD measurements did not indicate an imminent failure on this case.

It has been shown that the SiC based EPG coating of modern stator windings has a significant influence on dielectric loss measurements. The effects can be as strong as to mask the losses from the slot sections of the coils. During conventional DF measurements, it has been shown that the measurements are much more sensitive to the changes of resistivity of the EPG coating over time rather than to the deterioration of the main insulation. With DFR measurements, it is possible to visualize the influence of the EPG and to assess the resistivity of the coating independently from the main insulation.

It has also been demonstrated that different regions of the measured DFR curves can be used to assess different parts of the stator winding insulation systems. The measurements showed that DF values measured at very low frequency, such as 1 mHz, are more sensitive to deterioration than the values measured at 60 Hz.

BIBLIOGRAPHY

- Stone, C. G., and al. 2014. *Electrical Insulation for Rotating Machines: Design, Evaluation, Aging, Testing, and Repair*. 2nd Edition. 9781118892299.
- E. A. Boulter and G. C. Stone, “Historical development of rotor and stator winding insulation materials and systems,” *IEEE Electr. Insul. Mag.*, vol. 20, no. 3, pp. 25–39, May/Jun. 2004.
- Mottershead, G., and al. 2021. *Handbook of Large Hydro Generators: Operation and Maintenance*. 9781119524205.
- Klemper, G., and Kerszenbaum, I. 2018. *Handbook of Large Turbo-Generator Operation and Maintenance*. 9781119390718.
- OMICRON Academy Training Material. PD diagnostics on motors and generators with the MPD series. 2023.
- Can-Ortiz A, Laudebat L, Valdez-Nava Z, Diahm S. Nonlinear Electrical Conduction in Polymer Composites for Field Grading in High-Voltage Applications: A Review. *Polymers*. 2021; 13(9):1370. <https://doi.org/10.3390/polym13091370>
- OMICRON Academy Training Material. Reliable stator core fault detection in RotM with CPC100. 2021.
- M. Lachance and F. Oettl, "A Study of the Pulse Propagation Behavior in a Large Turbo Generator," 2020 IEEE Electrical Insulation Conference (EIC), Knoxville, TN, USA, 2020, pp. 434-439, doi: 10.1109/EIC47619.2020.9158584.
- J. R. Weidner: „Design und Zustandsüberwachung von Grenzflächen bei Ständerwicklungen großer Turbogeneratoren“, 3. ETGFachtagung: Grenzflächen in elektrischen Isoliersystemen, Würzburg, Germany, 2008.
- D.L. Evans, “ IEEE Working Group report of problems with hydrogenerator thermoset stator windings Part I-Analysis of survey,” *IEEE Trans. on Power Apparatus and Systems*, vol. PAS-100, no. 7, pp. 3284–3293, 1981.
- R. Bomba, U. Gross, and J. Kaiser, “VGB data base generator damage cases”, *VGB PowerTech*, vol. 11/2005, pp. 87–92, 2005.
- CIGRE Study Committee SC11, EG11.02, “Hydrogenerator Failures – Results of the Survey,” 2003.

High-voltage test techniques – Partial discharge measurements. International Electrotechnical Commission, 3rd ed., 2000. IEC Standard 60270.

Ravindra, A., & Wolfgang, M. (2022). High Voltage and Electrical Insulation Engineering, 2nd Edition. 978-1-119-56894-0.

IEEE Guide for Insulation Maintenance of Electric Machines, in IEEE Std 56-2016 , vol., no., pp.1-86, 11 Nov. 2016, doi: 10.1109/IEEEESTD.2016.7740867.

B. K. Gupta, I. M. Culbert, "Assessment of Insulation Condition in Rotating Machine Stators", Ontario Hydro, IEEE Transaction on Energy Conversion, pp. 500-508, Vol. 7, No. 3 Sept 1992.

IEEE Recommended Practice for Testing Insulation Resistance of Electric Machinery, in IEEE Std 43-2013 (Revision of IEEE Std 43-2000) , vol., no., pp.1-37, 6 March 2014, doi: 10.1109/IEEEESTD.2014.6754111.

C. Hudon, N. Amyot, S. Bernier, E. David and M. Essalihi, "Comparison of DC Ramp and Polarization and Depolarisation Tests on Hydrogenerators," 2018 IEEE Electrical Insulation Conference (EIC), San Antonio, TX, USA, 2018, pp. 114-119, doi: 10.1109/EIC.2018.8481087.

G. R. Soltani and E. David, "Condition assessment of rotating machine winding insulation by analysis of charging and discharging currents," Conference Record of the 2006 IEEE International Symposium on Electrical Insulation, Toronto, ON, Canada, 2006, pp. 336-339, doi: 10.1109/ELINSL.2006.1665326.

IEEE Recommended Practice for Measurement of Power Factor Tip-Up of Electric Machinery Stator Coil Insulation, in IEEE Std 286-2000 , vol., no., pp.1-29, 22 March 2001, doi: 10.1109/IEEEESTD.2001.92415.

IEC/TS 60034-27-3, Rotating Electrical Machines – Part 27: Dielectric Dissipation Factor Measurements on Stator Winding Insulation of Rotating Electrical Machines, 2015.

R. Vogelsang, R. Brütsch, K. Fröhlich. How imperfections in mica tape barriers influence tree growth and breakdown time. Conference on Electrical Insulation and Dielectric Phenomena (CEIDP). 2003 pp. 657–660.

R. Vogelsang, T. Weiers, K. Fröhlich, R. Bruetsch. Electrical breakdown in high-voltage winding insulations of different manufacturing qualities. IEEE Electrical Insulation Magazine, 2006. 22(3):5–12.

R. Bruetsch, M. Tari, K. Fröhlich, T. Weiers, R. Vogelsang. Insulation failure mechanisms of power generators [feature article]. IEEE Electrical Insulation Magazine, 2008. 24(4):17–25.

- IEEE Guide for the Measurement of Partial Discharges in AC Electric Machinery, in IEEE Std 1434-2014 (Revision of IEEE Std 1434-2000) , vol., no., pp.1-89, 4 Dec. 2014, doi: 10.1109/IEEESTD.2014.6973042.
- IEC/TS 60034-27 (2006-12), Rotating electrical machines – Part 27: Off-line partial discharge measurements on the stator winding insulation of rotating electrical machines.
- IEC/TS 60034-27-2 (2012-03), Rotating electrical machines – Part 27-2: On-line partial discharge measurements on the stator winding insulation of rotating electrical machines.
- Fournié, R., et R. Coelho. 2000. « Diélectriques: Bases théoriques ». *Techniques de l'ingénieur*, vol. 3, no D2300, p. 1-18.
- David, É. 2010a. *Matériaux diélectriques : Chapitre 3 - Propriétés diélectriques statiques*. Coll. « Notes du cours SYS-862 Matériaux diélectriques ». Montréal: École de Technologie Supérieure.
- Serway, R.A., et J.W. Jewett. 2009. *Physics for scientists and engineers : with modern physics*, 8th éd. vol. 2. Belmont, (CA) USA: Brooks/Cole.
- Küchler, Andreas. (2018). *High Voltage Engineering*. 10.1007/978-3-642-11993-4.
- Jonscher, A.K. 1983. *Dielectric relaxation in solids*. London (UK): Chelsea Dielectric Press, 380 p.
- David, É. 2010b. *Matériaux diélectriques : Chapitre 4 - Diélectrique soumis à un champ variable*. Coll. « Notes du cours SYS-862 Matériaux diélectriques ». Montréal: École de Technologie Supérieure.
- OMICRON Academy Training Material. TANDO 700. Chapter 3. Dissipation/power factor measurement on high-voltage devices. Theory – Basics of DF/PF measurements. 2019.
- Gafvert, Uno. (2004). *Dielectric response analysis of real insulation systems*. 1 - 10 Vol.1. 10.1109/ICSD.2004.1350276.
- C. Hao and B. Gao, "Study on the frequency domain dielectric spectroscopy of rotating machines insulation," 2016 IEEE International Conference on High Voltage Engineering and Application (ICHVE), Chengdu, China, 2016, pp. 1-4, doi: 10.1109/ICHVE.2016.7800599.
- R. Goffeaux, M. Krecke, B. Comte, M. Cottet, and B. Fruth. *Dielectric test methods for rotating machine stator insulation*. In *Annual Report, Conference on Electrical Insulation and Dielectric Phenomena*, 1998, pages 528–533 vol. 2, 1998.

C. Sumeder, "Statistical lifetime of hydro generators and failure analysis," in IEEE Transactions on Dielectrics and Electrical Insulation, vol. 15, no. 3, pp. 678-685, June 2008, doi: 10.1109/TDEI.2008.4543104.

"IEEE Recommended Practice for Thermal Cycle Testing of Form-Wound Stator Bars and Coils for Large Rotating Machines," in IEEE Std 1310-2012 (Revision of IEEE Std 1310-1996), vol., no., pp.1-30, 21 May 2012, doi: 10.1109/IEEESTD.2012.6204190.

"IEEE Recommended Practice for Voltage-Endurance Testing of Form-Wound Bars and Coils," in IEEE Std 1043-1996, vol., no., pp.1-20, 30 Nov. 1997, doi: 10.1109/IEEESTD.1997.82412.

"IEEE Standard for Voltage Endurance Testing of Form-Wound Coils and Bars for Hydrogenerators," in IEEE Std 1553-2002, vol., no., pp.1-12, 7 March 2003, doi: 10.1109/IEEESTD.2003.94234.

OMICRON PTM DIRANA User Manual. 2022.

MEGGER IDAX300/350 – Insulation Diagnostic Analyzer User Guide. 2020.

OMICRON MPD800 User Manual. 2021.

OMICRON CAL 542 User Manual. 2022.

OMICRON PD Webinar Series. Introduction to partial discharge measurements. August 2020.

OMICRON TANDO 700 User Manual. 2017.

E. David. 2021 IEEE Dissection Workshop, Modeling – Dissection related. June 2021.

N. Taylor. Diagnostics of stator insulation by dielectric response and variable frequency partial discharge measurements, October 2006. <http://kth.diva-portal.org/smash/get/diva2:11239/FULLTEXT01>. Licentiate Thesis, Kungl Tekniska Högskolan (KTH), Stockholm.

D. J. Conley and N. Frost, "Fundamentals of semiconductive systems for high-voltage stress grading," Proceedings Electrical Insulation Conference and Electrical Manufacturing Expo, 2005., Indianapolis, IN, USA, 2005, pp. 89-92, doi: 10.1109/EEIC.2005.1566265.

N. Taylor and H. Edin, "Stator end-winding currents in frequency-domain dielectric response measurements," in IEEE Transactions on Dielectrics and Electrical Insulation, vol. 17, no. 5, pp. 1489-1498, October 2010, doi: 10.1109/TDEI.2010.5595550.

- J. Cheng, N. Taylor, P. Werelius, A. K. Abideen and J. Hao, "Influence of Nonlinear Stress Grading Material on Dielectric Frequency Response of Stator Insulation," 2020 IEEE International Conference on High Voltage Engineering and Application (ICHVE), Beijing, China, 2020, pp. 1-5, doi: 10.1109/ICHVE49031.2020.9279961.
- E. David and L. Lamarre, "Low-frequency dielectric response of epoxy-mica insulated generator bars during multi-stress aging," in IEEE Transactions on Dielectrics and Electrical Insulation, vol. 14, no. 1, pp. 212-226, Feb. 2007, doi: 10.1109/TDEI.2007.302890.
- Taylor, N. (2010). Dielectric response and partial discharge measurements on stator insulation at varied low frequency.
- G.M. Pinto, E. Helal, H. Ribeiro, E. David, G.J.M. Fechine and N. R. Demarquette, " Use of Kramers-Kronig Transform and Vogel-Fulcher-Tammann Equation to Probe the Molecular Dynamics of Polyamide 10.10 Nanocomposites," *2023 IEEE Conference on Electrical Insulation and Dielectric Phenomena (CEIDP)*, East Rutherford, NJ, USA, 2023,
- M. Farahani, H. Borsi and E. Gockenbach, "Dielectric response studies on insulating system of high voltage rotating machines," in IEEE Transactions on Dielectrics and Electrical Insulation, vol. 13, no. 2, pp. 383-393, April 2006, doi: 10.1109/TDEI.2006.1624283.
- E. Calo, R. Álvarez, L. Catalano and P. M. del Valle, "Dielectric frequency response of a MV stator coil: effect of humidity and thermal ageing," *2020 IEEE Electrical Insulation Conference (EIC)*, Knoxville, TN, USA, 2020, pp. 242-245, doi: 10.1109/EIC47619.2020.9158695.
- R. Soltani, E. David and L. Lamarre, "Impact of humidity on dielectric response of rotating machines insulation system," in IEEE Transactions on Dielectrics and Electrical Insulation, vol. 17, no. 5, pp. 1479-1488, October 2010, doi: 10.1109/TDEI.2010.5595549.
- David, Éric. "Low-frequency dielectric response of epoxy-mica insulated generator bars during multi-stress aging." IEEE Transactions on Dielectrics and Electrical Insulation 14 (2007).
- U. Gäfvert et al, "Dielectric Spectroscopy in Time and Frequency Domain Applied to Diagnostics of Power Transformers", 6th International Conference on Properties and Applications of Dielectric Materials, June 21-26, 2000, Xi'an, China.

A. Gorji, S. Banerjee and S. Jayaram, "Dielectric Characterization Study on Medium-Voltage Ethylene Propylene Rubber (EPR) and Tree-Retardant Cross-Linked Polyethylene (TR-XLPE) Cables under Varying Thermal Conditions," *2020 IEEE Electrical Insulation Conference (EIC)*, Knoxville, TN, USA, 2020, pp. 10-13, doi: 10.1109/EIC47619.2020.9158709.

"IEEE Recommended Practice for Insulation Testing of AC Electric Machinery (2300 V and Above) With High Direct Voltage," in *IEEE Std 95-2002 (Revision of IEEE Std 95-1977)*, vol., no., pp.1-56, 12 April 2002, doi: 10.1109/IEEESTD.2002.93574.

Helgeson, A. (2000). Analysis of dielectric response measurement methods and dielectric properties of resin-rich insulation during processing (PhD dissertation, Institutionen för elkraftteknik). Retrieved from <https://urn.kb.se/resolve?urn=urn:nbn:se:kth:diva-2972>